FINDING AN OPTIMUM SURFACE CHEMISTRY FOR $BaO/TiO_2/Al_2O_3$ SYSTEMS AS NO_x STORAGE MATERIALS

A THESIS
SUBMITTED TO THE DEPARTMENT OF CHEMISTRY AND
THE INSTITUTE OF ENGINEERING AND SCIENCES OF
BILKENT UNIVERSITY
IN PARTIAL FULFILLMENT OF THE REQUIREMENTS
FOR THE DEGREE
OF
MASTER OF SCIENCE

By

GÖKSU SEDA ŞENTÜRK

JULY 2010

To My Beloved Parents Emin & Hawva…

I certify that I have read this thesis and in my opinion it is fully adequate, in scope and quality, as a thesis of the degree of Master of Science

_____

Assistant Prof. Dr. Emrah ÖZENSOY (Supervisor)

I certify that I have read this thesis and in my opinion it is fully adequate, in scope and quality, as a thesis of the degree of Master of Science

_____

Prof. Dr. Ömer DAĞ

I certify that I have read this thesis and in my opinion it is fully adequate, in scope and quality, as a thesis of the degree of Master of Science

_____

Prof. Dr. Saim ÖZKAR

I certify that I have read this thesis and in my opinion it is fully adequate, in scope and quality, as a thesis of the degree of Master of Science

_____

Assoc. Prof. Dr. Margarita KANTCHEVA

I certify that I have read this thesis and in my opinion it is fully adequate, in scope and quality, as a thesis of the degree of Master of Science

_____

Prof. Dr. Oğuz GÜLSEREN

Approved for the Institute of Engineering and Sciences

_____

Prof. Dr. Levenet ONURAL

Director of Institute of Engineering and Sciences

ABSTRACT

FINDING AN OPTIMUM SURFACE CHEMISTRY FOR $BaO/TiO_2/Al_2O_3$ SYSTEMS AS NO_x STORAGE MATERIALS

GÖKSU SEDA ŞENTÜRK

M.S. in Chemistry

Supervisor: Assistant Prof. Dr. Emrah ÖZENSOY

July 2010

Titania promoted NO_x storage materials in the form of $BaO/TiO_2/Al_2O_3$ were synthesized via two different sol-gel preparation techniques, with varying surface compositions and morphologies [1, 2]. The influence of the TiO_2 units on the NO_x storage component (8 - 20 wt. % BaO), the nature of the crystallographic phases, thermal stabilities and the dispersion of the surface oxide/nitrate domains were investigated.

The structural characterization of the synthesized NO_x storage materials were analyzed by means of BET surface area analysis, X-ray diffraction (XRD), ex-situ Raman spectroscopy, scanning electron microscopy (SEM), energy dispersive X- ray (EDX) and transmission electron microscopy (TEM). Comparative analysis of the results showed that the TiO_2/Al_2O_3 support material derived by the co-precipitation of the corresponding hydroxides via the sol-gel technique, exhibited distinctively more homogenous distribution of TiO_2 domains.

The functionality/performance of these materials upon NO_x and SO_x adsorptions were monitored by temperature programmed desorption (TPD) and in-situ Fourier transform infrared (FTIR) spectroscopy. An improved Ba surface dispersion was observed for the $BaO/TiO_2/Al_2O_3$ materials synthesized via the co-precipitation of alkoxide precursors which was found to originate mostly from the

increased fraction of accessible TiO_2/TiO_x sites on the surface. These TiO_2/TiO_x sites functioned as strong anchoring sites for surface BaO domains and were tailored to enhance surface dispersion of BaO. The relative stability of the NO_x species adsorbed on the $BaO/TiO_2/Al_2O_3$ system was found to increase in the following order: NO^+/N_2O_3 on alumina << nitrates on alumina < surface nitrates on BaO < bridged/bidentate nitrates on large/isolated TiO_2 clusters < bulk nitrates on BaO on alumina surface and bridged/bidentate nitrates on TiO_2 crystallites homogenously distributed on the surface < bulk nitrates on the BaO sites located on the TiO_2 domains.

The detailed study of the interaction of SO_x with $BaO/TiO_2/Al_2O_3$ ternary oxide materials showed that titania (TiO_2) was a promising candidate for improving the sulfur tolerance on these type of surfaces. Adsorption of SO_x on both pure Al_2O_3 and TiO_2 showed that Al_2O_3 formed strongly bound SO_x species, that were thermally stable up to T > 1073 K. SO_x adsorption directly altered stability of the nitrate species on the Ti/Al (Protocol 1, Protocol 2) samples. SO_x uptake properties of the $BaO/TiO_2/Al_2O_3$ materials were found to be strongly influenced by the morphology of the TiO_2/TiO_x domains and the BaO loadings (8/20 wt% BaO). Consequently, the presence of titania domains was seen to decrease the SO_x desorption temperatures and enhance the sulfur-tolerance of these materials by destabilizing the accumulated sulfate species. SO_x exposure on the synthesized materials led to a significant decrease in the NO_x adsorption capacities. The results obtained from FT-IR spectra showed that the sulfur deposition on the NO_x storage materials promoted by TiO_2 were more readily removed with respect to the conventional 8(20)Ba/Al samples.

Keywords: NO_x storage materials, NSR, LEANOX, BaO, Al_2O_3, TiO_2, anatase, rutile, $BaTiO_3$, sulfur poisoning, $DeNO_x$, NO_2, SO_x, FTIR, TPD.

ÖZET

$BaO/TiO_2/Al_2O_3$ YAPISINDAKİ NO_x DEPOLAMA MALZEMELERİNİN OPTİMUM YÜZEY KİMYASININ BELİRLENMESİ

GÖKSU SEDA ŞENTÜRK

Kimya Bölümü Yüksek Lisans Tezi
Tez Yöneticisi: Yrd. Doç. Emrah ÖZENSOY
Temmuz 2010

Bu çalışmada, iki farklı sol-jel hazırlama tekniği kullanılarak NO_x depolama malzemesi olan $BaO/TiO_2/Al_2O_3$ numuneleri sentezlenmistir. TiO_2 birimlerinin NO_x depolama bileşeni olan BaO (kütlece ağırlıkları % 8 ve % 20) ile etkileşimi, oluşan farklı kristalografik fazlar, malzemelerin ısıl kararlılıklarındaki değişiklikler ve yüzeydeki oksit/nitrat dağılımlarındaki farklılaşmalar incelenmiştir. Mevcut çalışmanın merkezindeki sav, NO_x depolama malzemelerinin yüzeylerindeki BaO birimlerinin yüzey dağılımlarının ve yüzey difüzyon özelliklerinin, özel yapılardaki TiO_2/TiO_x bileşenleri kullanılarak kontrollü bir şekilde değiştirilebileceğinin gösterilmesidir.

Sentezlenen NO_x depolama malzemelerinin yapısal karakterizasyonu, BET (Brunauer, Emmett, ve Teller) yüzey alanı ölçümleri, x-ışını kırınımı (XRD), Raman spektroskopisi, taramalı elektron mikroskobu (SEM), enerji saçınım x-ışını spektroskopisi (EDX) ve geçirimli elektron mikroskopisi (TEM) teknikleri kullanılarak yapılmıştır. Elde edilen sonuçlar detaylı bir şekilde karşılaştırılıp analiz

edildiğinde, sol-jel tekniği kullanılarak eşzamanlı çöktürme yöntemiyle sentezlenen TiO_2/Al_2O_3 destek malzemelerindeki TiO_2 birimlerinin, daha türdeş bir dağılım sergilediği ortaya çıkmaktadır.

Bu malzemelerin NO_x ve SO_x adsorpsiyonları sırasındaki/sonrasındaki davranışları sıcaklık programlı yüzeyden buharlaştırma (TPD) ve Fourier Dönüşümlü Kızıl Ötesi Spektroskopisi (FTIR) teknikleri ile izlenmiştir. Alkoksit öncü malzemeleri kullanılarak sentezlenen $BaO/TiO_2/Al_2O_3$ numuneleri üzerindeki barium oksit adacıkları daha iyi bir yüzey dağılımı göstermektedir. Bu numunelerin yüzeyinde türdeş ve iyi bir şekilde dağılmış olan TiO_2/TiO_x birimleri yüzeydeki BaO bileşenleri için güçlü çapa görevi görerek, BaO birimlerini kendilerine bağlamış ve böylece BaO birimlerinin yüzey dağılımını arttırmıştır. Yüzeyde depolanan NO_x türlerinin ısıl kararlılıkları şu şekilde sıralanmaktadır: Al^{3+}- NO/N_2O_3 << Al^{3+}-nitratları < BaO yüzeyi üzerindeki nitratlar < büyük TiO_2 birimlerine bağlı köprülü nitratlar < BaO üzerindeki oylumsal (bulk) nitratlar ve yüzeye türdeş şekilde dağılmış küçük TiO_2 birimlerine bağlı köprülü nitratlar < TiO_2 üzerindeki BaO yüzeyine bağlı oylumsal (bulk) nitratlar.

SO_2'nin üçlü oksit yapıdaki $BaO/TiO_2/Al_2O_3$ malzemeleri ile olan etkileşiminin detaylı olarak incelenmesi sonucunda; bu tür malzemelere eklenen TiO_2 birimlerinin, bu malzemelerdeki kükürt zehirlenme direncinin arttırılması için güçlü bir aday olduğunu göstermiştir. Ti/Al (P1, P2) yüzeylerine SO_x'in tutunması, yüzeye bağlanan nitratların kararlılıklarını ve miktarlarını azaltmıştır. $BaO/TiO_2/Al_2O_3$ malzemelerindeki SO_x birikimi ve kükürt zehirlenme miktarları doğrudan, TiO_2/TiO_x birimlerinin yüzey morfolojisine ve malzemede kullanılan BaO'in kütlece ağırlık miktarına bağlı olduğu saptanmıştır. FTIR sonuçları TiO_2 ile zenginleştirilmiş NO_x depolama malzemelerinden kükürt salınımının, TiO_2 içermeyen, sıradan 8(20) Ba/Al NO_x depolama malzemelerine göre daha kolay olduğu ortaya koymuştur.

Anahtar Kelimeler: NO_x depoloma malzemeleri, NSR, LEANOX, BaO, Al_2O_3, TiO_2, anataz, rutil, $BaTiO_3$, kükürt zehirlenmesi, $DeNO_x$, NO_2, SO_x, FTIR, TPD.

ACKNOWLEDGEMENT

I would like to express my gratitude to…

My supervisor Assistant Prof. Dr. Emrah Özensoy for his guidance, patience and supervision throughout my studies.

Prof. Ö. Dağ and Assoc. Prof. M. Kantcheva for fruitful discussions and help with the preparation of the binary oxide TiO_2/Al_2O_3 support materials

Stanislava Andonova, Emine Kayhan and Evgeny Vovk for their partnership and help during this research.

Scientific and Technical Research Council of Turkey (TUBITAK) (Project Code: 108M379, 107Y115). This work was also partially supported by the European Union FP7 project called UNAM-REGPOT (Contract No: 203953).

Beril Baykal, Safacan Kölemen and my group members Emre Emmez, Zafer Say and Emrah Parmak for their valuable friendship.

Ahmet Yurttadur, my parents; Emin and Havva and my brother Anıl for their continuous support and love.

TABLE OF CONTENTS

LIST OF TABLES

LIST OF FIGURES

1 INTRODUCTION

Air pollution caused primarily by the exhaust gases from automotive and stationary sources (power plants, chemical industry) remains an important global environmental problem, especially with the increasingly stringent emission limits worldwide. These emissions are mainly formed through the combustion of fossil fuels (coal, petroleum and natural gas) which mainly produces water vapour (H_2O) and carbon dioxide (CO_2), known to cause the greenhouse effect. Moreover, toxic chemicals such as carbon monoxide (CO), unburned and/or partially burned hydrocarbons (HCs) or particulate matter (PM), nitrogen oxides (NO_x) and sulfur oxides (SO_x) are the other typical pollutants produced [3]. Many regulations and studies are taken into consideration worldwide, in order to reduce the harmful gases and convert them into harmless gases.

Global oil reserves are constantly decreasing and as a result, the fossil fuel costs show an increasing trend in long term projections. Therefore, the automobile sector is trying to find solutions to minimize the fuel consumption. In 1984, the lean-burn engine attracted attention for its remarkable fuel economy [4]. The typical lean-burn engines operate at an air-fuel (A/F) ratio of 25/1, whereas the conventional gasoline engines operate at A/F ratios of 14.5/1 [5, 6]. Table 1 compares the representative compositions of the exhaust gases for diesel (lean-burn) vs. gasoline engines [7].

Table 1. Typical concentrations of untreated exhaust gases for diesel and gasoline engines [7].

Exhaust Components	Diesel Engine (Vol %)	Gasoline Engine (Vol %)
H_2O	*2 – 10*	*10 – 12*
CO_2	*2 – 12*	*10 - 13.5*
CO	*0.01 - 0.1*	*0.1 - 6*
O_2	*5 – 15*	*0.2 – 2*
HC (% C)	*0.005 - 0.05*	*0.5 – 1*
NO_x	*0.003 - 0.06*	*0.1 – 6*
SO_x	*10 – 100 ppm*	*15 – 60 ppm*
PM	*20 – 200 mg/m³*	*1 – 10 mg/m³*

In Europe by the end of 2014, NO_x emissions from diesel engines are required to go through a three-fold decrease from 0.25 $g.km^{-1}$ to 0.08 $g.km^{-1}$ as mentioned in the EURO 6 AECC regulations named as the "Emission Control Technologies and the Euro 5/6 Emission Legislation" [8]. In order to achieve these high environmental standards restricting the NO_x emissions [8] from diesel-equipped vehicles, reduction of NO_x through efficient catalytic emission after-treatment systems and fuel efficient engine technologies are required.

Different types of catalysts were developed for these purposes. One important catalyst used is the three-way-catalysts (TWCs) for gasoline after treatment applications. The commercially available TWCs typically contain Pt-Rh and/or Pd/Rh noble metals dispersed on a washcoat made up of Al_2O_3, CeO_2, ZrO_2, CaO, MgO and La_2O_3 [9]. These catalysts enable the reduction of NO_x to N_2 and O_2, the oxidation of CO to CO_2 and the oxidation of the unburned HCs to CO_2 and H_2O simultaneously [4]. In Figure 1, it is visible that TWCs perform very well at an A/F ratio of 14.5/1. However, the problem arises in reducing NO_x in the presence of large amounts of oxygen (i.e. under oxidizing or "lean" conditions, A/F = 25/1). Thus in a lean environment TWCs become ineffective for NO_x removal.

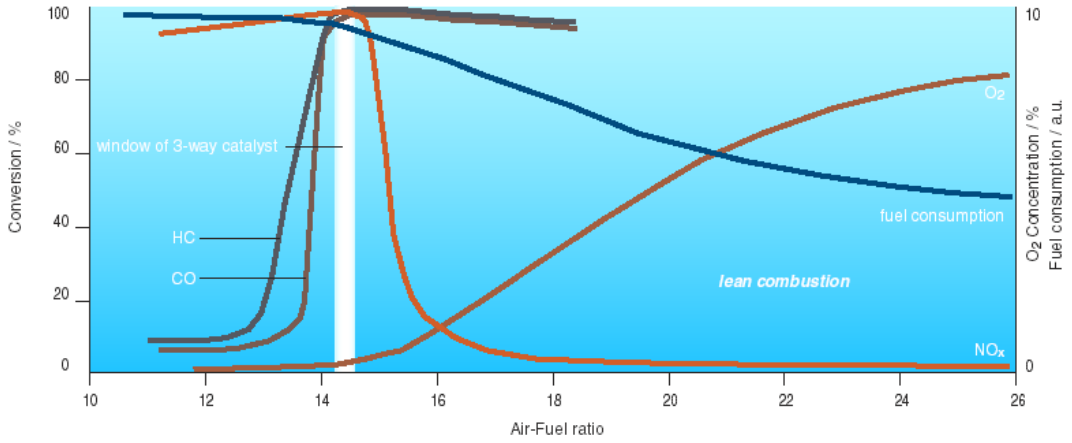

Figure 1. Fuel consumption and 3-way performance of a gasoline engine as a function of air–fuel (A/F) ratio [5].

The other major catalytic technology proposed and used for the removal of NO_x emissions from the lean-burn vehicles is the Selective Catalytic Reduction (SCR) technology. There are two main types of SCR catalysts; ammonia/urea selective catalytic reduction catalysts (NH_3-SCR) and hydrocarbon selective catalytic reduction catalysts (HC-SCR) [6]. The first catalyst (NH_3-SCR) used has some drawbacks regarding the use of toxic and corrosive NH_3 as the reductant (NH_3-SCR) and the reaction of NO_2 and NH_3 forming the exposive ammonium nitrate leading to the deactivation of the catalyst [10]. Secondly, the HC-SCR method which uses zeolite-based HC-SCR exhibits disadvantages due to very limited low-temperature activity (i.e. below 573 K) and the deactivation by of the catalyst by water and SO_2.

NO_x storage reduction (NSR) also known as the Lean NO_x Trap (LNT) technology is one of the promising alternatives for the catalytic NO_x removal from lean - burn gasoline engines [5, 11, 12]. The first NSR catalyst was developed and put into the market by Toyota in 1994 [13, 14]. The typical catalysts most commonly used for NSR applications involve combinations of precious noble metals (Pt, Pd, Rh) for oxidation and reduction purposes and K_2O and/or barium oxide (BaO) as the primary NO_x storage component, supported on a high surface area (~200 m^2/g) support material, such as γ-Al_2O_3. The NSR catalytic concept [15-18] is built on an alternating lean/rich engine operation. During the long "lean" period (~60 s) that is abundant in oxygen the NO_x is trapped on the NO_x storage component. This is

followed by a short "rich" period (~8 s) where NO_x is released and successively reduced to N_2 on the noble active sites, in a gas phase environment that is enriched in unburned hydrocarbons, H_2 and CO (reductant atmosphere) [19].

The possible mechanism of the NSR system as mentioned above begins with the lean atmosphere where NO_x (> 90% of which is found as NO in diesel engines) is first oxidized to NO_2 over the precious metal sites and then stored as nitrites or nitrates on the trapping agent. During the following reduction stage, the stored NO_x is further reduced to nitrogen (N_2), while $Ba(NO_3)_2$ storage units are converted into BaO domains. The trapping ability of the NSR catalyst is thus restored after a lean cycle followed by a rich cycle [15].

Although a number of improvements on the NSR catalysts have been suggested [20-25], problems still remain which are mainly associated with the deactivation of the catalysts. Thermal deterioration is one of these problems which is due to reaction of the NO_x storage material with the support material as well as due to the morphology changes of the precious metals and the NO_x storage material [26]. However, the probably most challenging problem to be solved for the NSR catalyst is the deactivation caused by sulfur. Sulfur compounds present in diesel fuel are predominantly found as substituted benzothiophenes. The quantity of sulfur compounds present in petroleum distillate usually increases with boiling range and therefore conventional diesel fuel invariably contains more sulfur than gasoline. The sulfur compounds originally in the engine lubricating oil also produce sulfur dioxide (SO_2) during the combustion process. This can be converted into sulfates on the catalyst through the mechanism as shown in the following equations [27]:

$$SO_2 + ½\ O_2 \rightarrow SO_3 \quad (1)$$

$$BaO + SO_3 \rightarrow BaSO_4 \quad (2)$$

Due to the higher thermodynamic stability of sulfate species compared to the corresponding nitrates, ''sulfates'' are not decomposed under the same regenerating conditions as nitrates. Thus, sulfur effectively blocks the catalytic sites for NO_x storage and gradually reduces the overall NO_x storage capacity of the NSR catalysts [27]. In addition, SO_2 also effectively poisons the support material. SO_2 and/or SO_3^{2-}

are initially oxidized to SO_4^{2-} over the precious metal sites and then SO_4^{2-} further reacts with the γ-Al_2O_3 support material forming aluminum sulfate ($Al_2(SO_4)_3$) which hinders the nitrate spill-over, limits the nitrate diffusion on the support surface and plugs the micro-pores of the γ-Al_2O_3 matrix [28].

Despite the constant reduction in the sulfur content of the refined fuel in the past decades, sulfur poisoning remains one of the major causes for catalytic deactivation of the NSR systems [28-32]. Sulfur poisoning typically leads to the formation of alkaline earth metal and precious metal sulfate or sulfide complexes that are thermodynamically more stable than nitrates as discussed above. For, a large number of oxide substrates the stability of the surface species increases in the following order: $NO_2^- \sim CO_3^{2-} < NO_3^- < SO_4^{2-}$ [29, 33-36].

Efforts towards improving the catalytic tolerance against sulfur poisoning and designing highly active and stable novel NSR catalysts are vital for the globalization of the NSR technology [28, 30, 32]. Misono [37], Fritz [38] and several others [1, 35, 36, 39-42] reported detailed studies on the improvement and the durability enhancement of NSR catalysts. NSR catalysts have been commercialized for lean-burn gasoline and diesel applications in Europe, Japan and North America. However, the formulated catalysts originally are successfully used in limited markets such as Japan where the sulfur content of the diesel fuel is relatively low (below 10 ppm) [43] when compared to countries in the U.S. (500 ppm) and Europe (50 pppm) [43].

An attempt to enhance the sulfur resistance of NSR catalysts was made by Yamazaki et al. [44] and Fanson et al. [45] by incorporating Fe into Ba-based LNT catalysts. According to Yamazaki et al. Fe was found to decrease sulfur uptake and promote the decomposition of $BaSO_4$. On the other hand, Fanson et al. observed that Fe supported the formation of a bulk nitrate species which was resistant to poisoning. Other researchers have suggested the addition of Mg into the NSR catalyst and studied the sulfur deactivation [46]. Furthermore, there are several examples of mixed binary oxides regarding the addition of TiO_2 [47], $BaSnO_3$ [48] or Li_2O on support oxides such as Al_2O_3 [49].The use of Cu containing catalysts has also been studied by promoting and/or replacing Pt in the NSR catalysts [50, 51]. The sulfur tolerance of this type of catalyst was suggested to arise from the inability of Cu to oxidize SO_2.

Another approach focuses on the use of novel and improved support materials with enhanced sulfur tolerance. Matsumoto and co-workers [28, 52] tried to find an optimum chemical composition of the NO_x storage compounds in order to minimize the growth of the sulfate domains, and adjust the surface acidity of the support to inhibit the SO_x storage. The macroscopic geometrical structure of the catalytic monolith was also found to be effective in limiting the size of the sulfate particles and controlling the sulfate decomposition/desorption temperature [5, 14]. It was shown that the smaller the sulfate particle size, the easier the decomposition of the sulfates from the surface. This approach became the basis for attacking the deactivation problem in NSR system [44].

Furthermore, the effect of doping of the alumina support with different alkaline metals or alkali-earth metals was also studied in which promising results were reported for lithium doped samples [53]. Theoritical calculations [54] showed that strontium sulfate decomposes at much lower temperatures than barium sulfate when both H_2 and CO are used in the regeneration of the sulfated storage sites (presuming the formation of H_2S, CO_2 and H_2O). Recently, Corbos and co-workers [36, 55] studied the effect and the desulfation of model Pt/BaO/support NSR catalysts. In these studies, BaO supported on Al–Si and Ce–Zr mixed oxides was found to exhibit higher NO_x storage capacity after exposure to sulfating conditions in comparison with BaO supported on alumina. Moreover, the use of ceria-zirconia as a support was found to result in the destabilization of the bulk $BaSO_4$ upon H_2(g) exposure.

TiO_2 is commonly utilized as a support material in numerous catalytic processes or as an active catalyst in photocatalytic systems. TiO_2 exists in three major crystallographic forms; rutile, anatase and brookite. The anatase type is usually used for photocatalytic applications [56]. The preparation of TiO_2 with the sol-gel method has advantages in terms of purity, homogeneity and stoichometric control [56]. The particle size of TiO_2 depends on grain size, impurities, composition and the calcination temperature. Moreover, acting as a support material for the NSR catalysts, TiO_2 was also found to have a noticeable ability to suppress the sulfur deposition [57]. This was related with the surface acidity of TiO_2, inhibiting the adsorption of acidic sulfur species and making the sulfates less stable on the TiO_2 compared to other oxide supports. It was also shown that the decomposition

temperature of the sulfates on a TiO_2 support was lower than that of γ-Al_2O_3. However, in order to circumvent some of the unfavourable properties of TiO_2 such as the limited thermal stability, low surface area, and poor mechanical properties, its combination with secondary oxides can be considered to design novel support materials with enhanced properties. Along these lines, γ-Al_2O_3 [58-60] and/or ZrO_2 [4, 61, 62] are among the promising choices for the secondary oxides that can be used in combination with TiO_2. It was reported that blending TiO_2 with γ-Al_2O_3 as a support material minimized the amount of SO_x deposit on a Pt/Ba/γ-Al_2O_3 catalyst and enhanced the NO_x storage of the sulfur-exposed catalysts. The blend of the non sulfur-poisoned Pt/TiO_2 catalyst with the sulfur-poisoned Ba/Pt/Al_2O_3 catalyst improved the sulfur desorption from the Ba/Pt/Al_2O_3 catalyst under rich conditions [28]. It was also suggested that the interface between Al_2O_3 and TiO_2 plays an important role in sulfate decomposition and the desorption processes [57]. Despite the established sulfur resisting effect of TiO_2 as an additive in the composition of the Pt/Ba/γ-Al_2O_3 NSR catalysts, most of the fundamental aspects regarding the influence of TiO_2 on the interaction between the NO_x storage component and the support material have not yet been elucidated in detail. In this study, the effect of TiO_2 on the surface distribution and the thermal stability of the catalytic species formed on the NO_x storage systems will be investigated via two different synthetic protocols.

In several former studies [28, 32, 57-60, 63-65] it was pointed out that titania addition to the conventional alumina support reduces the stability of the sulfates and the use of titania-containing mixed oxides as support materials provides a potential avenue for sulfur tolerance improvement. Furthermore, active sites on the TiO_2 surface can also be relatively readily regenerated under reaction conditions [58]. In the current study [1, 66], we have focused our attention on the structural and morphological changes occurring on the ternary oxide NO_x storage systems in the form of BaO/TiO_2/Al_2O_3 [1]. Our findings suggested that on the BaO/TiO_2/Al_2O_3 system, Ti-domains provide strong anchoring sites for the Ba-containing units and significantly alter the surface morphology, composition and the stoichiometry of the Ba-containing units as well as the surface mobility of the BaO clusters. As a continuation of these experiments [1], we have attempted to find an optimum chemistry for the ternary BaO/TiO_2/Al_2O_3 mixed oxide system. Along these lines,

the binary oxide TiO_2/Al_2O_3 support material was prepared by using various Ti and Al precursors via two different sol-gel precipitation techniques.

Thus, the composition-dependent and the temperature-dependent structural changes of different TiO_2/Al_2O_3 support materials and the corresponding ternary oxide NO_x storage systems ($BaO/TiO_2/A_2O_3$) are evaluated in detail by means of X-ray diffraction (XRD), Raman spectroscopy, Brunauer-Emmet-Teller (BET) surface area measurements, scanning electron microscopy (SEM), energy dispersive X-ray mapping (EDX-mapping) and transmission electron microscopy (TEM). Furthermore, the aim of the current work is to analyze the performance/functionality of these storage materials with NO_x interaction experiments and investigate the deactivation of these samples by SO_2 (g) + O_2 (g) through Fourier transform infrared (FTIR) spectroscopy and temperature programmed desorption (TPD) experiments.

2 EXPERIMENTAL

2.1 Sample Preparation

2.1.1 Synthesis of TiO_2/Al_2O_3 Support Materials

Binary oxide TiO_2/Al_2O_3 support materials were prepared via two different synthetic protocols (P1 and P2). The mole fraction of TiO_2 was kept constant at ~0.3 for both support materials.

In P1, the mixed oxide support was synthesized through a sol-gel method [1, 67]. $TiCl_4$ (Fluka, titanium (IV) chloride solution ~0.1 M in 20% hydrochloric acid) and γ-Al_2O_3 (PURALOX, 200 m^2/g, SASOL GmbH, Germany) were used as starting precursors. At first, 6.56 ml of titanium(IV) chloride solution was added drop wise with a syringe to 60 ml deionized water under continuous stirring, where the solution temperature was kept below 333 K inside an ice bath (avoiding the precipitation of hydroxides generated from the heat of the violently exothermic hydrolysis reaction). 13.62 g of γ-Al_2O_3 in powder form was slowly added to the diluted solution at room temperature. Finally, gelation started after adding 30 % v/v NH_3 (aq) to the mixture and adjusting the pH of the solution to 9. After aging the white gel under ambient conditions for 24 hours, the resultant blend was filtered and washed thoroughly with distilled water until the formed product was free of chloride ions, confirmed by the $AgNO_3$ test. The final product (Ti/Al (P1)) was dried in air at 423 K for 2 h.

The second series (P2) of the mixed TiO_2/Al_2O_3 oxide support material was synthesized through a sol-gel route that has been devised by our own research group [2]. The binary oxide support material was prepared by the co-hydrolysis of titanium and aluminium alkoxides. Initially, 24.63 g of aluminum *sec*-butoxide (97%, Sigma Aldrich) was mixed with 115 ml propan-2-ol (99.5 +%, Sigma Aldrich) and 3.1 ml acetylacetone (99.3 %, Fluka) for 30 min. Sequentially, 7.65 g titanium(IV) isopropoxide (97 %, Sigma Aldrich) was added dropwise to the mixture that proceeded for another half an hour. All of the synthesis steps were carried out at room temperature under vigorous stirring. The co-precipitation of the corresponding hydroxides was accomplished after the gradual addition of 5 ml of 0.5 M HNO_3 to the solution which consecutively led to the formation of gel. The resulting white

precipitate was aged under ambient conditions for 10 days. The final mixed support oxide (Ti/Al (P2)) was attained after drying the gel in air at 873 K for 2 h.

For further analysis of the obtained TiO_2/Al_2O_3 support materials (through P1 and P2), various thermal treatment processes ranging from 423 K to 1273 K (2 h in air for each temperature) were performed.

2.1.2. Synthesis of $BaO/TiO_2/Al_2O_3$: NO_x Storage Materials

A set of NO_x storage materials in the form of $BaO/TiO_2/Al_2O_3$ were synthesized by conventional incipient wetness impregnation of the TiO_2/Al_2O_3 binary oxide support materials (prepared via P1 and P2). In order to obtain 8 wt% and 20 wt% BaO loadings, TiAl (P1) (dried in air at 473K) and (P2) (dried in air at 673K) were impregnated with aqueous solutions of barium nitrate (ACS Reagent, ≥ 99 %, Riedel-de Häen, Germany). The synthesized materials ($Ba(NO_3)_2/TiO_2/Al_2O_3$) were then dried at 353 K. Finally, for the thermal analysis, the samples were calcined under Ar (g) atmosphere for 2 h at various temperatures, ranging from 423 K to 1273 K. Consequently, representative samples from the treated batches were collected for ex-situ characterization after each temperature treatment. Moreover, for FTIR and TPD studies, the synthesized NO_x storage materials were further annealed at 873 K for another 2 h under Ar (g) before being inserted into the catalytic reactor for additional adsorption/desorption experiments.

Other than the synthesized materials, pure γ-Al_2O_3, pure TiO_2 (Anatase Nano-Powder, 99.9 %, 40 nm, Inframat Advanced Materials) and (8/20 wt %) $BaO/\tilde{a}$-Al_2O_3 samples [1, 66] were used as reference materials.

In the current text, synthesized NO_x storage materials are denoted as XBa/Ti/Al (P1, P2). Compositions of these materials are also listed below in Table 2.

Table 2. Compositions of the synthesized ternary oxide NO_x storage materials.

Acronyms	*BaO (wt %)*	*TiO_2 (wt %)*	*Al_2O_3 (wt %)*
8Ba/Ti/Al (P1)	8	23	69
20Ba/Ti/Al (P1)	20	20	60
8Ba/Ti/Al (P2)	8	27	65
20Ba/Ti/Al (P2)	20	24	56

2.2 Experimental Techniques

2.2.1 BET

BET specific surface area measurements were conducted using a Micromeritics Tristar 3000 surface area and porosity analyzer. The samples were measured via low-temperature isothermal adsorption-desorption of N_2. Before the surface area measurements, the samples were outgassed at 623 K for 2 h in vacuum.

2.2.2 XRD

The powder XRD patterns were recorded using a Rigaku diffractometer, equipped with a Miniflex goniometer and an X-ray source with Cu$K\alpha$ radiation, at λ = 1.54 Å, 30 kV and 15 mA. The powder samples were pressed and affixed to standard-sized glass slides and scanned in the 10–80^o, 2θ range with a scan rate of 0.01^o s^{-1}. Diffraction patterns were assigned using Joint Committee on Powder Diffraction Standards (JCPDS) cards supplied by the International Centre for Diffraction Database (ICDD).

2.2.3 Raman Spectroscopy

The Raman spectra were recorded on a HORIBA Jobin Yvon LabRam HR 800 instrument, equipped with a confocal Raman BX41 microscope, spectrograph with an 800 mm focal length and a CCD detector. The Raman spectrometer was equipped with a Nd: YAG laser (λ = 532.1 nm). While the Raman experiments were conducted, the laser power was tuned to 20 mW, measured at the sample position, in order to minimize the sample heating effects. All the powder samples were mechanically dispersed onto a single-crystal Si holder. The incident light source was dispersed by holographic grating with a 600 grooves/mm and focused onto the sample by using a 50X objective. The confocal hole and slit entrance were set at 1100 and 200 μm, respectively. The spectrometer was regularly calibrated by adjusting the zero-order position of the grating and comparing the measured Si Raman band frequency with the typical reference value of 520.7 cm^{-1}. All Raman spectra were acquired within 100-4000 cm^{-1} with an acquisition time of 213 s and a spectral resolution of 4 cm^{-1}. Pure TiO_2 (Anatase - Nano powder, 99.9%, 40nm,

Inframat Advanced Materials), rutile (obtained after calcination of the anatase nanopowder at 1273 K for 2 h) $Ba(NO_3)_2$ (ACS Reagent, $\geq$ 99% purity, Riedel-de Häen, Germany) were used as reference powders.

2.2.4 SEM/EDX

SEM and EDX data were performed using a Zeiss EVO40 environmental SEM that is equipped with a LaB6 electron gun, a vacuum SE detector, an elevated pressure SE detector, a backscattering electron detector (BSD) and a Bruker AXS XFlash 4010 detector. Samples for SEM and EDX analysis were prepared by grinding the samples into fine powder and mechanically dispersing them on an electrically conductive carbon film which was placed on an aluminium sample holder. No additional coatings or dispersive liquids were used for the sample preparation. SEM images were obtained using a vacuum SE detector where electron acceleration voltage of the incident beam was varied within 10-20 kV and the samples were kept typically at $\leq 5 \times 10^{-5}$ Torr inside the SEM. All of the EDX data were collected using an electron acceleration voltage of 20 kV and a working distance of 15 mm. For the EDX elemental mapping studies, at least four independent areas of identical dimensions on the same catalyst sample were investigated in order to assure the reproducibility of the results.

2.2.5 TEM

Transmission electron microscopic (TEM) images were obtained with a resolution of 0.14 nm on a JEM-2010 (200 keV) microscope equipped with an Energy Dispersive X-ray (EDX) spectrometer with a Si (Li) detector. The analyzed area was about 10 nm. The energy resolution of EDX was 127 eV. The sample for the TEM study was prepared by ultrasonic dispersing in ethanol and subsequent deposition of the suspension upon a “holey” carbon film supported on a copper grid.

2.2.6 FTIR

FTIR spectroscopic measurements were carried out in transmission mode in a batch-type catalytic reactor coupled to an FTIR spectrometer (Bruker Tensor 27) and a quadruple mass spectrometer (QMS) (Stanford Research Systems, RGA 200) for

TPD and residual gas analysis (RGA). FTIR spectra were recorded using a Hg-Cd-Te (MCT) detector, where each spectrum was acquired by averaging 128 scans with a spectral resolution of 4 cm^{-1}. The samples were mounted into the IR cell [28] consisting of a five-way stainless steel chamber equipped with optically-polished BaF_2 windows. This IR cell was connected to a gas manifold (including a dual-stage rotary vane pump and two turbomolecular pumps) so that the pressure in the cell could be varied within 1000 Torr - 10^{-6} Torr. About 20 mg of finely ground powder sample was pressed onto a high-transmittance, lithographically-etched fine tungsten grid which was mounted on a copper sample holder assembly, attached to a ceramic vacuum feedthrough. A K-type thermocouple was spot-welded to the surface of a thin tantalum plate attached on the W-grid to monitor the sample temperature. The sample temperature was controlled within 298 K – 1100 K via a computer-controlled DC resistive heating system using the voltage feedback from the thermocouple. After having mounted the sample in the IR cell, sample was gradually heated to 373 K in vacuum and kept at that temperature for at least 12 h before the experiments in order to ensure the removal of water from the surface. In an attempt to minimize the effect of background water (i.e. re-adsorption of water on the sample from the reactor walls and the gas manifold), the system was frequently baked. Prior to each NO_x adsorption experiment, the walls of the vacuum system were passivated by flushing 2 Torr of NO_2 (g) for an extended period of time (20 min) followed by evacuation at the same temperature. Next, in order to obtain a surface that is free of adsorbed NO_x and other adsorbates, the sample was annealed in vacuum by increasing the temperature to 1023 K in a linear fashion at a constant rate of 12 K min^{-1}. After this annealing protocol, sample was cooled down to 323 K. Before acquisition of each spectral series, a background spectrum of the clean, adsorbate-free sample was obtained in vacuum at 323 K (with a residual reactor pressure ~1 x 10^{-5} Torr).
NO_2 (g) (prepared by reacting NO (g), Air Products, Purity > 99.9% and O_2 (g) Ersoy Gas, Purity > 99.9%) used in the adsorption experiments was further purified via several freeze-thaw-pump cycles before the experiments.

2.2.6.1 Surface Acidity via pyridine adsorption

The surface acidity of the studied oxide systems was investigated by in-situ FTIR spectroscopy measurements of chemisorbed pyridine. Pyridine (Merck KGaA,

purity > 99.0%) was used as a basic probe molecule in this procedure and further purified via several freeze-thaw-pump cycles before adsorption.

Prior to each pyridine adsorption experiment, the sample surface was activated (dehydrated) in the IR cell by ramping the sample temperature to 623 K and subsequently outgassing the sample at the same temperature for 1 h under vacuum (residual pressure < 10^{-4} Torr). After this pretreatment protocol, the sample was cooled down to 323 K and a background spectrum of the clean, adsorbate-free sample was obtained (with a residual reactor pressure < 1×10^{-5} Torr). Then, the sample was exposed to a precisely controlled dose of pyridine vapour ($P_{pyridine}$ = 3.0 Torr) for 15 min at 323 K. After the saturation of the sample surface (15 min), the system was evacuated at room temperature ($P_{reactor} < 1 \times 10^{-4}$ Torr). After the acquisition of the pyridine-saturated sample spectrum at 323 K, the sample was heated in vacuum to various temperatures within 323-723 K and then cooled back to 323 K for the sample spectra acquisition.

2.2.6.2 Stepwise NO_2 (g) adsorption experiments

In the first type of FTIR experiments, controlled doses of 0.6 Torr of NO_2 (g) (measured by a 0.1-1000 Torr MKS Baratron absolute pressure transducer) were introduced in a stepwise fashion onto the NO_x – free sample surface at 323 K. After having the acquired sample spectrum of each dose at 323 K, the system was evacuated to ~ 1 x 10^{-3} Torr before the next dosage. Typically, the low-temperature adsorption series was completed with saturating the surface sites with a final insertion of 8 Torr of NO_2 at 323 K for 20 min.

2.2.6.3 Temperature-dependent FTIR experiments

In a typical temperature-dependent adsorption experiment, the sample held at 323 K was exposed to 8 Torr of NO_2 for 20 min, which typically led to the saturation of the surface with NO_x species. Next, the system was evacuated (<1 x 10^{-4} Torr) and then the sample temperature was linearly ramped to a given temperature. Once the target temperature was achieved, annealing was stopped and the sample was cooled to 323 K where the sample spectrum was acquired. The same procedure was repeated

for different temperature intervals within 323 – 923 K in order to monitor the thermal behavior of the surface species via FTIR.

2.2.6.4 SO_2 (g) + O_2 (g) adsorption experiments

Prior to each SO_2 + O_2 adsorption experiment, the sample surface was activated (dehydrated) in the IR cell by ramping the sample temperature to 1023 K and subsequently outgassing the sample at 323 K for 20 min under vacuum (residual pressure < 10^{-4} Torr). After this pretreatment protocol, a background spectrum of the clean, adsorbate-free sample was obtained (with a residual reactor pressure < 1×10^{-5} Torr).

The sulfur exposure experiments were performed through four different spectral acquisition steps. In the first spectral acquisition step, the sample was exposed to ~0.6 Torr of SO_2 + O_2 (SO_2:O_2, 0.1:1) for 1 h at 323 K and the first FTIR spectrum was obtained under this condition. In the second step, the sample used in the first step was flashed to 473 K in SO_2 + O_2. After cooling the sample to 323 K, the second FTIR spectrum was acquired. In the third step, the sample used in the second step was further flashed to 673 K (in the presence of SO_2 + O_2) and the reactor was further evacuated at 323 K for 20 min ($P_{reactor}$ < 1×10^{-4} Torr) and the third FTIR spectral acquisition was carried out. In the fourth (i.e. the final) step, the sample used in the third step was flashed to 673 K in vacuum ($P_{reactor}$ < 1×10^{-4} Torr) and then the spectral acquisition was performed at 323 K in vacuum.

2.2.6.5 NO_2 (g) adsorption on prepoisoned materials

The samples were firstly activated as explained in section 2.2.6.4. Poisoning of the materials were achieved by introducing ~0.6 Torr SO_2 + O_2 (SO_2:O_2, 0.1:1) on the dehydrated sample at 323 K and further heating the sample in the gaseous mixture to 473 K for 30 min. Then, the system was evacuated at 323 K ($P_{reactor}$ < $1x10^{-3}$), prior to NO_2 adsorption. Next the poisoned sample was exposed to 8 Torr of NO_2 at 323 K for 20 min in order to saturate the surface with NO_x. Finally, the reactor was evacuated ($P_{reactor}$ < $1x10^{-3}$) at 323 K and FTIR spectrum of the sample was obtained.

In addition to these experiments, after performing the NO_x saturation on a poisoned sample as described above, the sample was flashed to 1023 K in vacuum, followed by cooling the sample to 323 K in vacuum and the FTIR data acquisition at 323 K in vacuum. This latter protocol allowed us to monitor the highly stable surface species that exist on a sample which is initially poisoned, then saturated with NO_x and then finally regenerated via a high temperature pumping/evacuation protocol.

2.2.7 TPD

2.2.7.1 Thermal stability of NO_x species on the Fresh Materials

TPD experiments were acquired by using a QMS, which was directly connected to the vacuum chamber through a pneumatic gate valve. The sample powder (mass = c.a. 20 mg) was pressed onto a tungsten grid which was mounted in the IR/TPD cell. Prior to each TPD data, oxidation-resistant thoria coated iridium filament of the mass spectrometer was outgassed for 30 min. After cooling to 323 K, the sample was exposed to 8 Torr of NO_2 for 20 min until the equilibrium was reached. Next, the system was outgassed to ~1 x 10^{-6} Torr in order to remove the weakly physisorbed molecules. Subsequently, TPD experiments were carried out. Evolved NO_x species during the desorption process were monitored by recording the QMS signals with mass to charge ratios (m/z) equal to 18 (H_2O), 28 (N_2/CO), 30 (NO), 32 (O_2), 44 (N_2O/CO_2) and 46 (NO_2) in pressure vs. time mode. A linear temperature ramp within 323 – 1023 K was used during the TPD experiments where the ramp rate was 12 K/min. In order to ensure the reproducibility of the results, TPD experiments were performed multiple times for each sample.

2.2.7.2 Thermal stability of SO_x/NO_x species on the Sulfated Materials

Sulfation of the materials were obtained by exposing ~0.6 Torr SO_2+O_2 (SO_2:O_2, 0.1:1) on the sample at 323 K, further heating in gaseous mixture to 473 K for half an hour and lastly evacuating at 323 K ($P_{reactor}$ < $1x10^{-3}$). The next step regarding the saturation of the surface with NO_2 was exactly the same as explained in section 2.2.7.1. In addition to the evolved NO_x species, SO_x species during the desorption process were also monitored by recording the QMS signals with mass to

charge ratios (m/z) equal to 18 (H_2O), 28 (N_2/CO), 30 (NO), *34 (H_2S)*, 32 (O_2), 44 (N_2O/CO_2), 46 (NO_2) and *64 (SO_2)* in pressure vs. time mode. A linear temperature ramp within 323 – 1023 K was used during the TPD experiments where the ramp rate was 12 K/min. In order to ensure the reproducibility of the results, TPD experiments were performed multiple times for each sample.

3 RESULTS AND DISCUSSION

3.1 TiO_2/Al_2O_3 Binary Oxide Support Materials

3.1.1 Structural Characterization of the Thermally Treated Ti/Al Support Materials

3.1.1.1 Specific Surface Area Measurements

Thermal changes and stability of the synthesized Ti/Al systems (P1 and P2) along with the ternary Ba/Ti/Al mixed oxides were analysed as a function temperature in the interval of 423 – 1273 K.

Table 3 illustrates the temperature dependence of the S_{BET} (m^2/g) of the samples within 623-1273 K. The same data is also graphically illustrated in Figure 2.

Figure 2 and Table 3 clearly indicate that the specific surface areas corresponding to all of the samples are strongly affected by the thermal treatments and as an outcome, the S_{BET} values tend to decrease in a monotonic fashion with increasing temperature. Typically such behaviour is rather common for thermal processes leading to sintering and/or phase transformations. From the results above, it is evident that the Ti/Al samples synthesized by P2, have considerably higher specific surface area values within 623 – 873 K when compared to the Ti/Al (P1) material. However at elevated temperatures (T > 1073 K), the porous structure of the Ti/Al (P2) system exhibits a relatively unstable character and therefore a profound loss in its structural integrity is observed. On the other hand, although Ti/Al (P1) samples have moderately lower surface area values within 623 - 1073 K, these materials tend to preserve their porous structure more efficiently even after the thermal treatment at 1273 K.

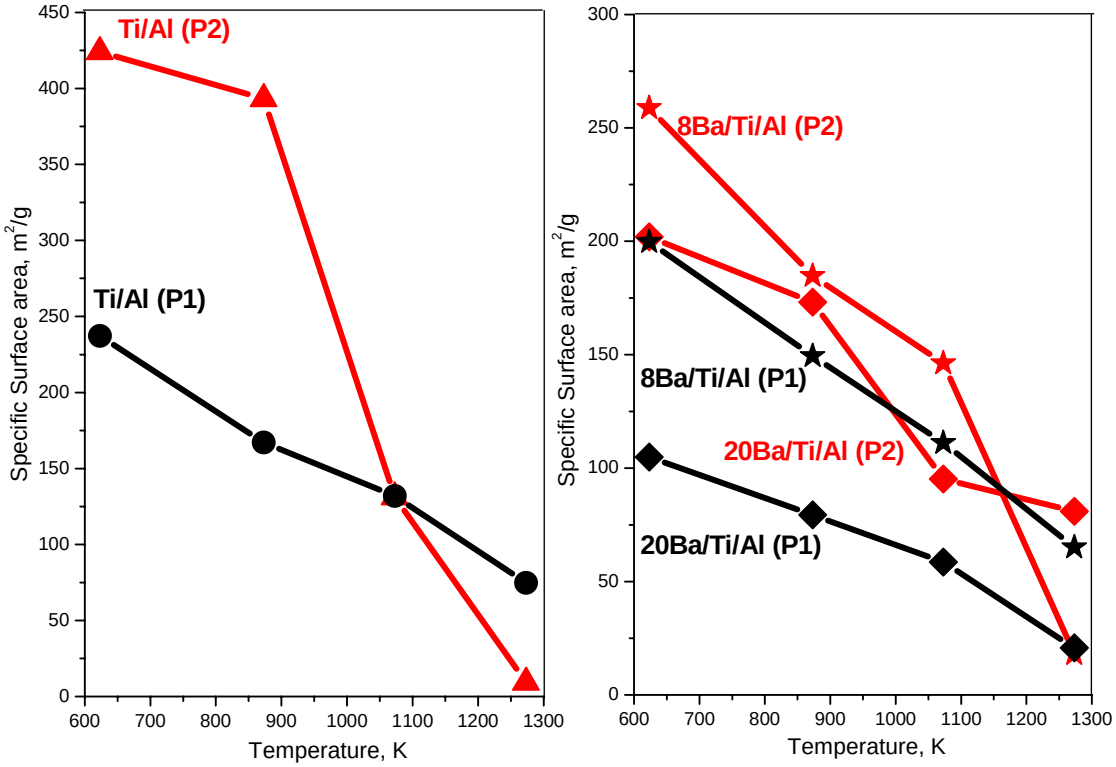

Figure 2. Specific surface area data for the samples after thermal treatments at various temperatures

Table 3. BET Specific surface area measurements of the samples calcined within 623-1273K

Sample [a] T/ K	Ti/Al (P1) [b]	Ti/Al (P2) [b]	8Ba/Ti/Al (P1) [c]	8Ba/Ti/Al (P2) [c]	20 Ba/Ti/Al (P1) [c]	20 Ba/Ti/Al (P2) [c]
623	237	424	200	259	105	202
873	167	393	150	185	79	173
1073	132	131	111	146	59	95
1273	75	9	65	18	21	81

[a] *Surface area values : m^2/g*

[b] *Samples were calcined under air at the given temperatures for 2 hr*

[c] *Samples were annealed under Ar (g) flow for 2 hr*

The BET data for the NO_x storage materials 8(20)Ba/Ti/Al (P1/P2) show relatively lower surface area when compared to the corresponding Ti/Al (P1, P2) support materials. Increasing the loading of the NO_x storage material (8 to 20 wt% BaO) for both protocols leads to smaller surface area values at elevated temperatures. However a reversal of the observed trend is clearly visible for the 8(20)Ba/Ti/Al (P2) samples at 1273 K, where higher Ba loadings lead to significantly higher surface area values as compared to the Ti/Al (P2) support material. A more elaborate discussion regarding these temperature-dependent structural changes will be provided in the later sections given below.

3.1.1.2 XRD Experiments

Figure 3 and Figure 4 represents the XRD data that reveal the thermal behavior of the binary Ti/Al (P1, P2) oxide systems within 300-1273 K. The results given in Figure 3 and 4 can be analyzed in detail in order to monitor the thermally induced structural changes of the support materials.

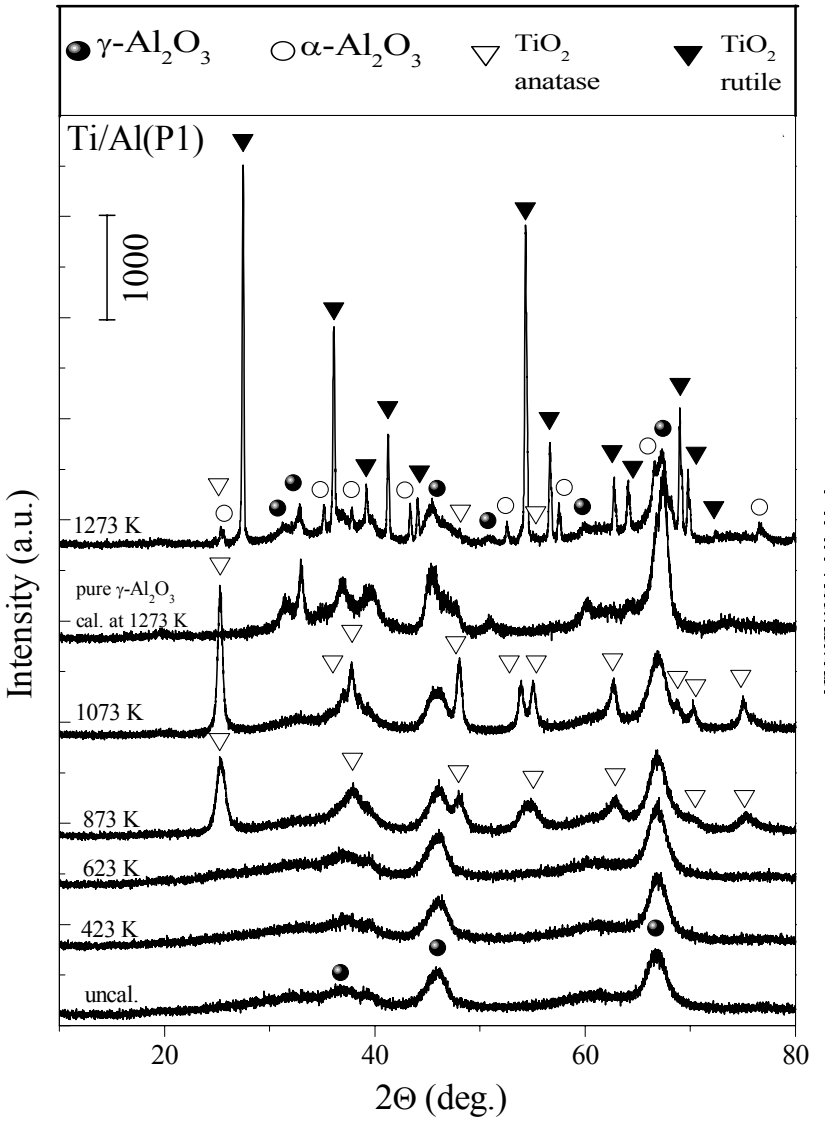

Figure 3. XRD patterns of the Ti/Al (P1) samples before and after calcination in the temperature range of 423-1273 K, pure γ-Al_2O_3 calcined at 1273 K is also shown in the figure

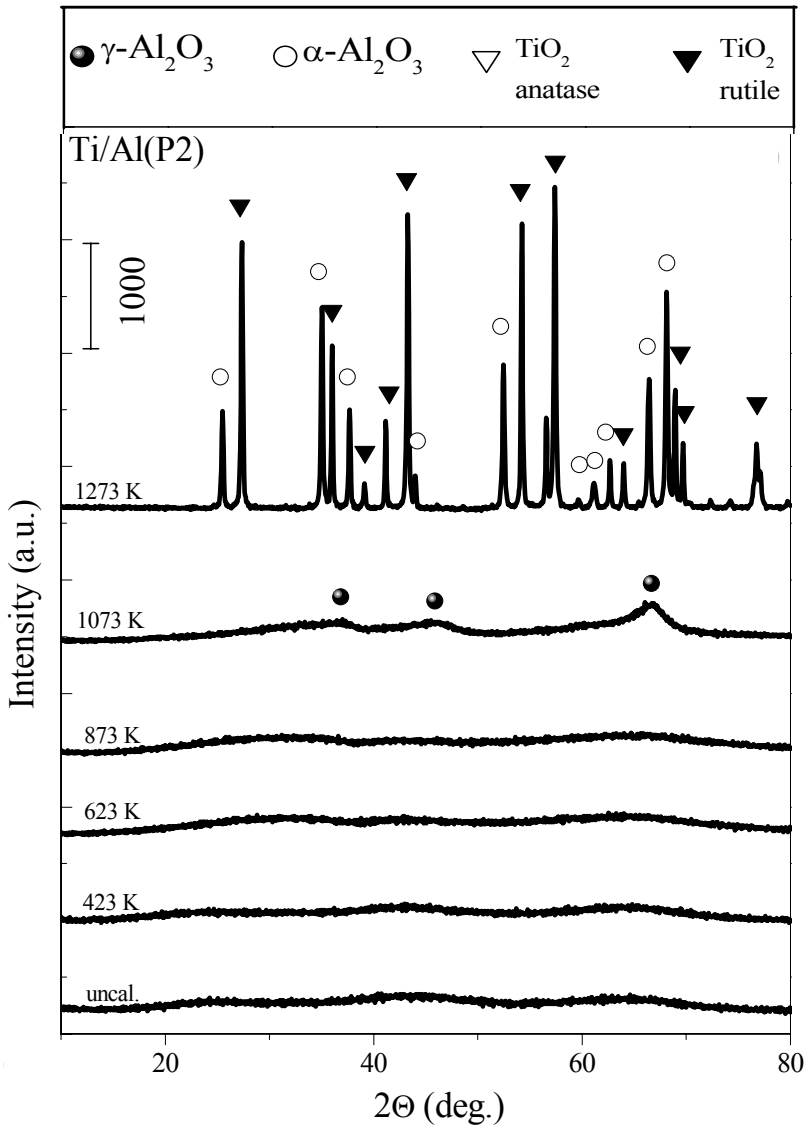

Figure 4. XRD patterns of the Ti/Al (P2) samples before and after calcination in the temperature range of 423-1273 K

Figure 3 illustrates diffraction lines associated with γ-Al_2O_3 (JCPDS 29-0063) at 423 and 623 K. For Ti/Al (P1) at $T \leq 623$ K no discernible diffraction peaks due to other crystalline phases can be observed which suggests that TiO_2 species present in Ti/Al (P1) have a very small average crystallite size or are still in an amorphous form. As for the Ti/Al (P2) (Fig. 4) support oxide, it can readily be seen that samples calcined within 423 to 1073 K contain very broad and poorly-defined diffraction lines that can probably be associated with γ-Al_2O_3 (JCPDS 29-0063). This suggests that within 423 – 1073 K, the Ti/Al (P2) support material exhibits a structure that predominantly consists of amorphous TiO_x/AlO_x mixed oxide domains.

When the Ti/Al (P1) sample is thermally treated at 873 K, the diffraction lines of anatase (JCPDS 21-1272) starts to be visible and become even more apparent after increasing the thermal treatment temperature to 1073K. This implies that some of the amorphous TiO_2 domains transform into anatase crystalline phase. However, after the heat treatment at 1273 K it is seen in Figure 3 that anatase starts to decrease its intensity in a significant manner, while a new set of intense lines associated with the rutile phase (polymorph of TiO_2, JCPDS 04-0551) appear. The XRD profile at this temperature also includes minor diffraction signals associated with the presence of α-Al_2O_3 (corundum, JCPDS 10-0173). Additionally, Figure 3 also demonstrates the XRD pattern of pure γ-Al_2O_3 calcined at 1273 K with the presence of diffraction lines related with γ-Al_2O_3 and no other features. This proves that the addition of titania to the system decreases the phase transformation temperature of γ-Al_2O_3 to α-Al_2O_3. Consequently, Figure 4 shows the support oxide prepared via P2 with a set of strong diffraction features corresponding to rutile (JCPDS 04-0551) and corundum (α-Al_2O_3, JCPDS 10-0173) phases. As described in detail elsewhere [1, 66-68], Al_2O_3 and TiO_2 components in the binary Ti/Al oxide system can form a solid solution, where alumina incorporates into the anatase lattice. Furthermore, in such a solid solution, anatase to rutile transformation is also accompanied by a phase transition in which γ-Al_2O_3 is transformed into α-Al_2O_3 (corundum). It should be noted that the γ-Al_2O_3 to α- Al_2O_3 phase transformation at 1273 K occurs to a greater extent for the Ti/Al (P2) system, in which corundum features are more visible than that of the Ti/Al (P1) sample. This is also in good agreement with the lower surface area of the Ti/Al (P2) sample at 1273 K.

3.1.1.3 Raman Spectroscopy Experiments

In order to have a better understanding of the vibrational structures of the binary oxide support materials, Raman spectroscopy measurements were applied to thermally treated (423 K – 1273 K) Ti/Al samples, as shown in Figures 5a and 5b.

From Figure 5 (c) and (d), the reference Raman spectra and XRD patterns corresponding to bulk anatase and rutile, polymorphs of TiO_2, can be readily identified. According to the factor group analysis [69, 70], anatase crystallizes in a tetragonal structure and belongs to the D_{4h}^{19} space group. The reference Raman spectrum of anatase (uppermost spectrum of Figure 5 (c)) consists of six Raman active modes ($1A_{1g}$, $2B_{1g}$, and $3E_g$) with positions at 144 (E_g), 197 (E_g), 399 (B_{1g}), 516 (A_{1g} + B_{1g}), 639 (E_g) and 796 cm^{-1} (E_g). The room temperature Raman band at 516 cm^{-1} is split into two peaks centered at 513 (A_{1g}) and 519 cm^{-1} (B_{1g}) [71]. Similarly, rutile also has a tetragonal structure [72], it belongs to the D_{4h}^{14} space group and is characterized by a Raman spectrum with four Raman active modes (A_{1g} + B_{1g} + B_{2g} + E_g) and a two-phonon scattering band at 236 cm^{-1}. These four modes are visible in the rutile spectrum presented in Figure 5 (c) at 143 (B_{1g}), 447 (E_g), 612 (A_{1g}) and 826 cm^{-1} (B_{2g}). Furthermore, it is worth emphasizing that the rutile band at 143 cm^{-1} has a very similar frequency to the E_g band of anatase at 144 cm^{-1}. However, it should be noted that the intensity of the E_g band of anatase is significantly more pronounced than that of the B_{1g} band of rutile.

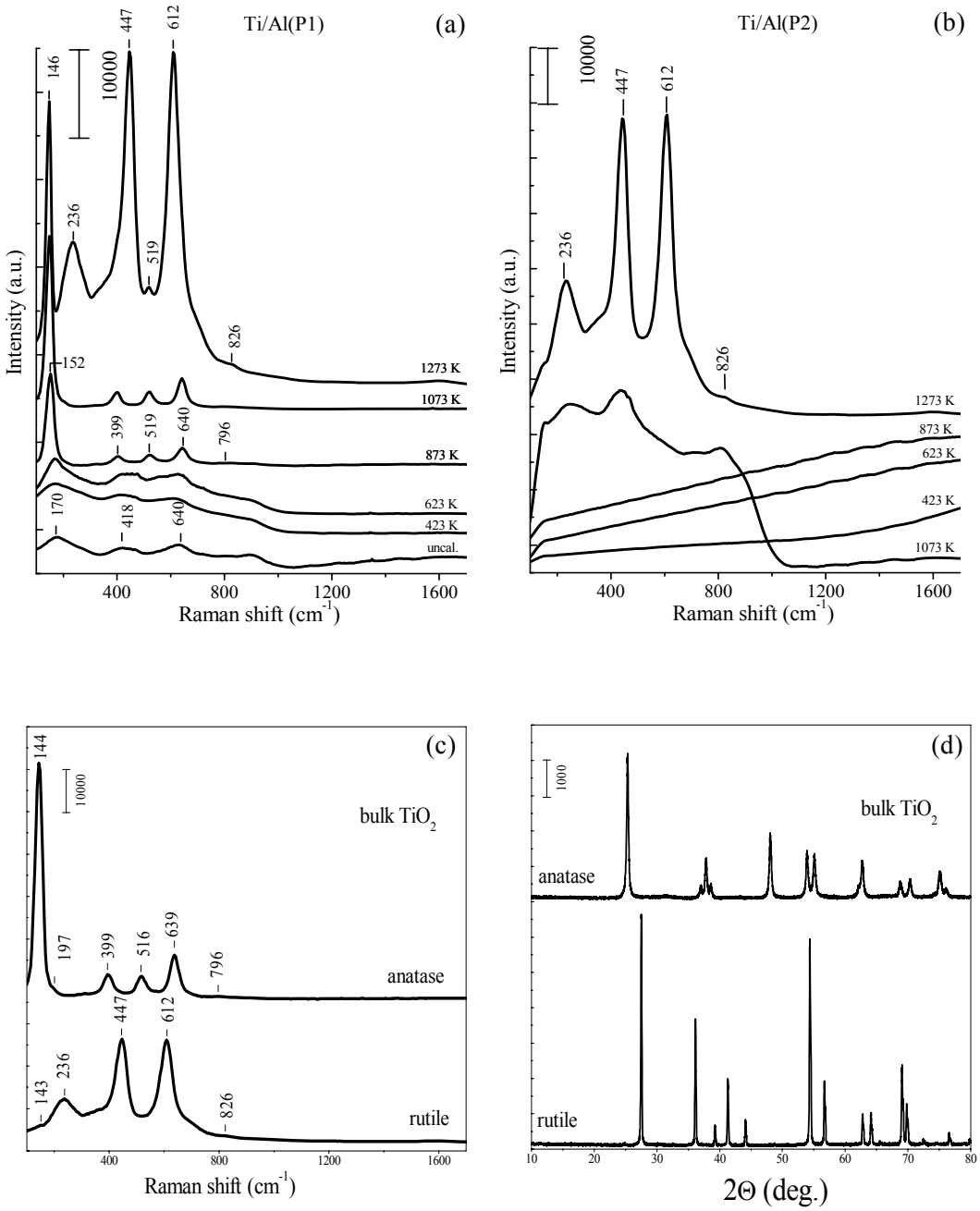

Figure 5. Temperature-dependent ex-situ Raman spectra corresponding to the calcined (423-1273 K) Ti/Al samples (a) Ti/Al P1 (b) Ti/Al (P2), (c) and (d) present the Raman and XRD data for the bulk anatase and rutile reference materials

In accordance with the XRD data presented above, it is seen from Fig. 5a and 5b that unlike the Ti/Al (P1) system, Ti/Al (P2) oxide support materials include features within 423 – 873 K with low Raman scattering cross sections related with poor crystallinity and/or small crystallite sizes [70, 72, 73]. The crystallinity of anatase is certainly more obvious at low temperatures for the support material prepared via P1 as seen in Figure 5a. These broad bands at around 170, 418, 630 cm^{-1} together with a complex set of features within 800-900 cm^{-1} resemble the reference (bulk) anatase spectrum (c). After thermal treatments above 873 K, anatase features become much more pronounced and shift to lower frequencies with a considerable decrease in their full-width at half-maximum (FWHM) values for Ti/Al (P1). Spectral broadening and the frequency shifts of the Raman bands corresponding to TiO_2 nanocrystals have been previously reported by several authors in the literature [72, 74]. These spectral changes were mainly attributed to phonon confinement, oxygen deficiencies (formation of nonstoichiometric phases) and pressure effects on the grains, induced by the surrounding grains or by the surface tension. It was suggested that if the influence of the surface defects is neglected, nanocrystallite anatase Raman features shift to lower frequencies with respect to their bulk values and their FWHM values decrease as the crystallite size increases. Therefore, it is conceivable that the observed decrease in the FWHM values of the Raman features of the Ti/Al (P1) system can be related to the growth and ordering of the anatase phase above 623 K (873K - 1073K). This result is also in good agreement with the XRD data presented in Figure 3. After the thermal treatment of the Ti/Al (P2) sample at 1073 K, a group of broad and convoluted Raman features become visible at 236, 447 and 826 cm^{-1}. These bands can be attributed to a poorly crystallized rutile phase [72]. It is worth mentioning that the reference Raman spectrum of rutile (c) was obtained after thermal treatment of pure anatase at 1273 K for 2 h. Thus, it is very likely that the bottom most spectrum in the (c) of Figure 5 corresponds mostly to the rutile phase. This is also evident in the XRD data for the same reference sample presenting sharp features associated with the rutile phase given in Figure 5 (d). This is not surprising since, in previous studies [75] a complete anatase to rutile phase transformation was reported on bulk TiO_2 samples at temperatures as low as 873 K. Moreover, Figure 5b shows the rutile growth in a significant manner when the annealing temperature is increased to 1273 K, no obvious indication of an anatase

phase is visible for the Ti/Al (P2) system. In addition, no Raman bands attributed to the presence of corundum are observed probably due to the very strong fluorescence background and the strong intensities of the rutile features with positions that overlap with those of the α-Al_2O_3. However, it is observed that in Figure 5a there are prominent Raman bands at 236, 447, 612 and 826 cm^{-1} which are readily assigned to the rutile structure, additionally an intensive Raman band at 146 cm^{-1} and the weakly expressed feature at 519 cm^{-1} signify the coexistence of the anatase. Thus, Raman data presented in Figure 5b indicate the presence of a homogenously-mixed oxide solution for the Ti/Al (P2) system within 473-873 K. This is in very good agreement with the current FTIR, TPD, SEM/EDX and TEM results.

Observation of the anatase to rutile phase transformation on the Ti/Al surface at a higher temperature with respect to the pure TiO_2 system suggests the stabilization of the anatase phase on the Ti/Al surface due to a strong interaction between the TiO_2 and *γ*-Al_2O_3 domains. The influence of Al_2O_3 on the phase transformation of TiO_2 nanoparticles and the structure of the composite was reported in a former study by differential scanning calorimetric (DSC) and XRD analysis [76]. It was found that the bonding interactions between the [TiO_6] octahedra on the anatase surface and the [AlO_6] octahedra result in a retardation of the anatase to rutile phase transition and impedes the growth of TiO_2 domains. In other words, strong interaction between the anatase and *γ*-Al_2O_3 domains (where packing of the oxide ions possesses cubic symmetry in both structures) leads to the formation of a solid solution which, in turn, hinders the anatase to rutile transition by increasing the corresponding phase transformation temperature. On the other hand, at relatively high temperatures where the anatase domains in the solution start to transform into the hexagonal rutile structure, rutile and *γ*-Al_2O_3 domains begin to phase segregate. This is due to the relatively low solubility of the hexagonal rutile structure in the cubic *γ*-Al_2O_3 lattice [68]. Thus, after this phase segregation, small *γ*-Al_2O_3 crystallites leaving the solution can readily undergo a phase transition and form the α-Al_2O_3 structure at temperatures that are significantly lower than that of the bulk *γ*-Al_2O_3 system.

3.1.1.4 SEM-EDX Measurements

Morphological changes in combination with elemental distribution were qualitatively investigated using a combination of SEM and EDX-elemental mapping techniques. Figure 6 presents selected representative SEM-EDX images of the Ti/Al (P1) and Ti/Al (P2) samples.

The color coding in Figure 6 clearly demonstrates the dissimilarity between the surface dispersion of the TiO_2/TiO_x domains on the Ti/Al (P1) and Ti/Al (P2) samples. EDX elemental maps in Figure 6 reveal scattered red and green islands (due to fake coloring) which represent Ti and Al containing domains, respectively. The first EDX map indicates that TiO_2/TiO_x are dispersed in a rather inhomogeneous fashion on the Ti/Al (P1) sample. In contrast, EDX elemental map corresponding to the Ti/Al (P2) sample is dominated by a yellow signal which originates from the combination (overlap) of red Ti and green Al signals implying a better dispersion of TiO_2/TiO_x domains on the Ti/Al (P2) sample (probably in the form of small crystallites or in the form of a solid TiO_x-AlO_x mixed oxide/solution).

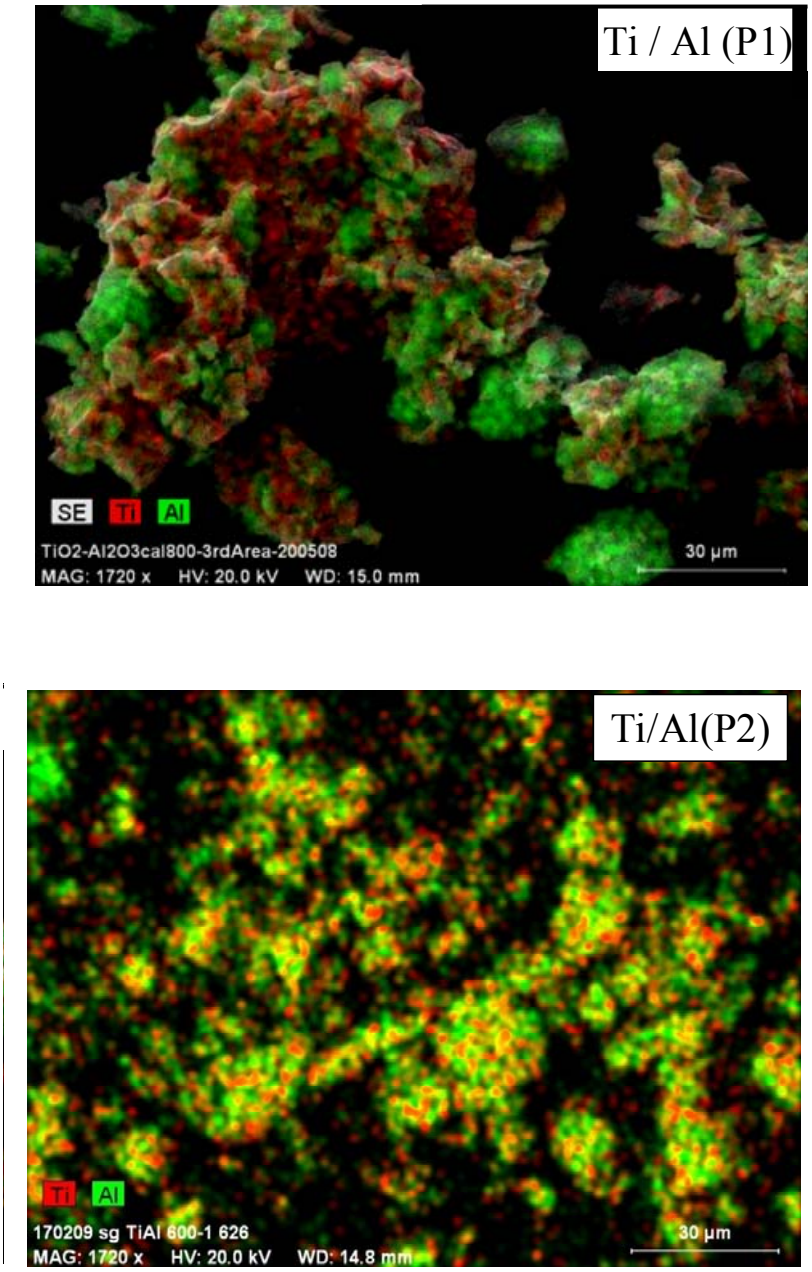

Figure 6. Ti and Al elemental EDX maping images for Ti/Al (P1) and Ti/Al P2.

3.1.1.5 TEM Measurements

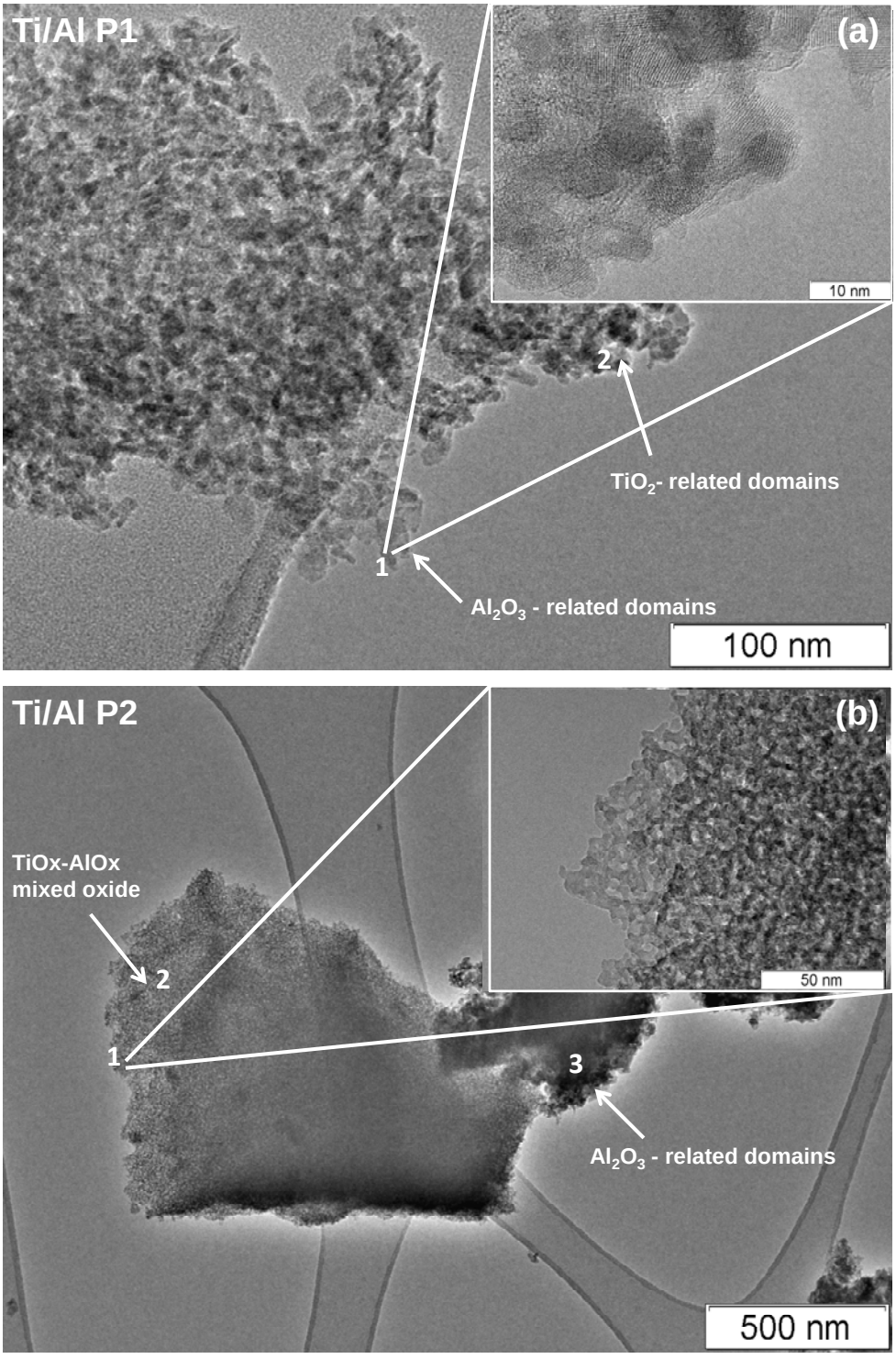

Figure 7. Representative TEM images of a) Ti/Al (P1) 1) γ-Al_2O_3-rich domains 2) TiO_2-rich domains on the sample b) Ti/Al (P2) 1-2) inset showing the sponge-like surface morphology of the TiO_x-AlO_x mixed oxide 3) darker area represents the Al_2O_3-rich domains on the sample

Figure 7 represents the TEM images showing the morphologies of the mixed Ti/Al (P1, P2) support materials. Area 1 in Figure 7a shows the typical rod like appearance of the γ-Al_2O_3 units on the sample. It is evident by the EDX measurements (data not shown) that this area predominantly corresponds to γ-Al_2O_3 (Ti : Al elemental ratio 0.2 : 99.8). However, area 2 corresponds to mostly TiO_2-rich domains. Ti/Al (P1) represents a more inhomogeneous surface distribution of Al_2O_3 and TiO_2 domains when compared with Ti/Al (P2). In Figure 7b the area marked with 1 is also shown with a higher magnification where it is readily visible that unlike Ti/Al (P1), Ti/Al (P2) exhibits a sponge-like fine structure which is most probably due to the complex structure of the mixed TiO_x/AlO_x oxide phase. The Ti:Al elemental ratio in area 1 in Figure 7b is close to 20:80 which is in very good agreement with the nominal composition expected from the relative concentrations used in the material synthesis (TiO_2 mole fraction = ~0.3). EDX elemental analysis of the darker area represented as area 3 in Figure 7b reveal almost exclusively Al_2O_3 domains. These observations indicate that the Ti/Al (P2) surface structure is mostly composed of a complex TiO_x/AlO_x mixed oxide with additional less prominent domains that are rich in Al_2O_3.

3.1.1.6 Surface Acidity: FTIR Spectra of Chemisorbed Pyridine

Surface acidity of the Ti/Al (P1) system was also investigated via pyridine adsorption in which the titration of the surface acid sites by the probe molecule (i.e. pyridine) was followed with FTIR spectroscopy.

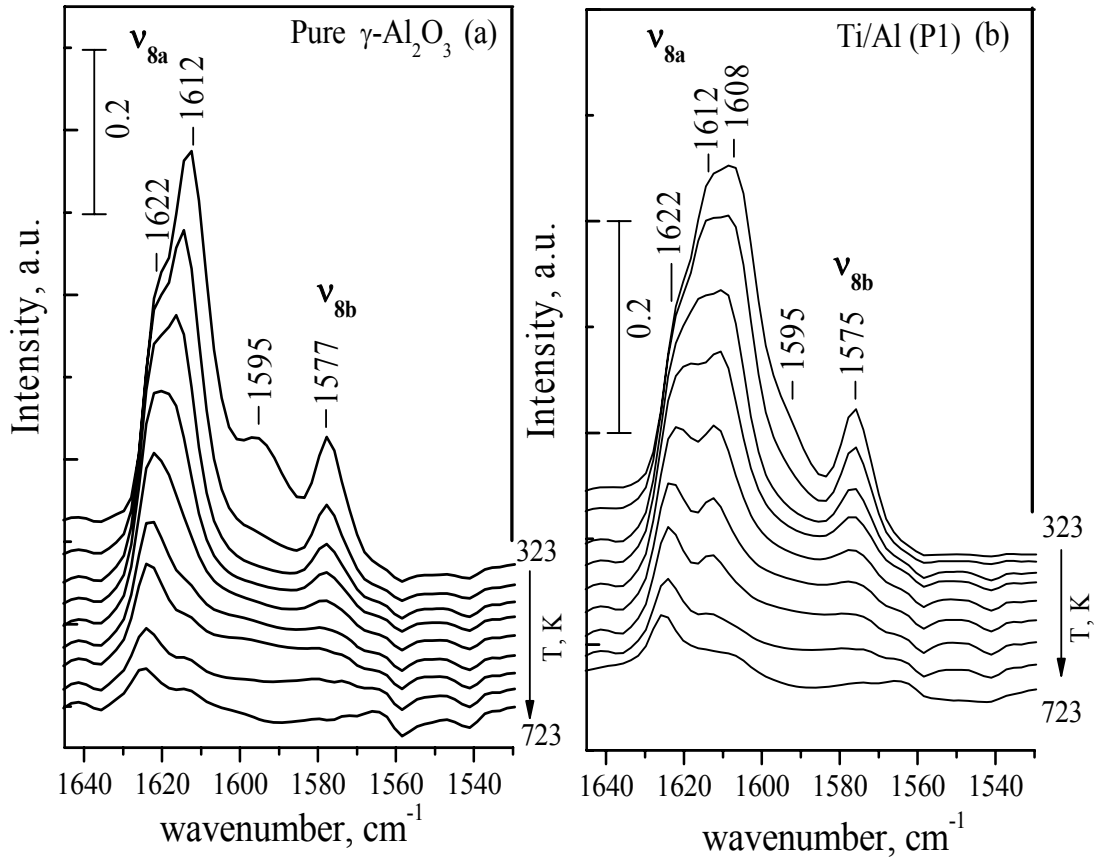

Figure 8. Temperature-dependent (323-723 K) FTIR spectra for chemisorbed pyridine species formed at room temperature on the surface of pure γ-Al_2O_3 (a) and on Ti/Al (P1) precalcined at 873 K (b).

Ti/Al (P1) binary oxide support material and γ-Al_2O_3 reference material were both calcined at 873 K in Ar (g) prior to the chemisorption experiments, followed by in-situ activation/evacuation at 623 K for 1 h. Figure 8 represents the evolution of the relevant pyridine vibrational bands as a function of annealing temperatures (323-723K). The vibrational modes within 1640-1100 cm^{-1} reveal various pyridine ring stretching modes υ(C-N) and υ(C-C). Room-temperature pyridine adsorption on both surfaces reveals bands at 1151, 1222, 1448, 1493, 1577 and 1612 cm^{-1} with additional visible shoulders at 1622, 1595, and 1237 cm^{-1}. The observed frequencies of pyridine resemble former results presented in the literature on similar oxide systems [77-80]. These bands can be assigned [77,81] to υ_{15}, υ_{9a}, υ_{19b}, υ_{19a}, υ_{8b}, two υ_{8a} and υ_3 modes of pyridine. The IR bands at ca. 1620-1600 (υ_{8a}), 1580 (υ_{8b}), 1490 (υ_{19a}) and 1450 (υ_{19b}) cm^{-1} can be attributed to the formation of pyridine species coordinated to the surface Lewis acid sites.

The characteristic differences of both samples were clearly observed within the 1640-1540 cm^{-1} vibrational region, therefore a detailed analysis of this specific spectral window was performed. The weakly expressed shoulder around 1595 cm^{-1} is attributed to the presence of a weakly interacting pyridine species (which disappear after annealing at 373K) that is coordinated to the surface via hydrogen bonding. The position and multiplicity of the υ_{8a} band in Figure 8, reveals two distinct features, the peak located around 1612 cm^{-1} and a shoulder at 1622 cm^{-1} that indicate the presence of two different types of Lewis acid sites. These temperature-dependent intensity changes provide valuable insight regarding the strength of the acid-base interactions between the basic pyridine probe molecule and the surface Lewis acid sites. In light of previous studies in the literature [79, 80], the band at 1577 cm^{-1} can be attributed to weak Lewis acid sites, which almost completely disappears at 573 K. The band at 1612 cm^{-1} can be assigned to medium-strength Lewis acid sites whose intensity is still visible at T > 573 K. It is appearent that the spectrum corresponding to the highest annealing temperature (723 K) is dominated by the 1622 cm^{-1} band, related with the strong Lewis acid sites remaining on the surface. These observations are in a good agreement with former studies [82,83] focusing on the surface acid-base properties of γ-alumina, which suggest the presence of three different types of Lewis acid sites exhibiting distinctively dissimilar acid strengths. It was reported [82, 83] that the band at 1580 cm^{-1} is due to the presence of weak octahedral (O_h) Al^{3+} Lewis

acid sites, whereas the feature at 1612 cm^{-1} is assigned to the presence of medium-strength Lewis acid sites consisting of a pair of coordinatively unsaturated Al^{3+} ions in octahedral and tetrahedral environments. Finally the band at 1622 cm^{-1} was attributed to the strongest Lewis acid sites related to the presence of coordinatively unsaturated tetrahedral (T_d) Al^{3+} cations.

Comparison of the data corresponding to the reference γ-Al_2O_3 material given in Figure 8b with that of the Ti/Al (P1) reveals similar temperature-dependent IR bands for the pyridine adsorption on these surfaces. In addition, an intense feature located at ca. 1608 cm^{-1} (partially overlapping with the feature at 1612 cm^{-1}) can also be observed. After the temperature increase, this new feature becomes more discernible and shifts to higher frequencies. Former studies [84-86] regarding pyridine adsorption on the anatase (TiO_2) surface reported a similar band which was attributed to the Ti^{4+} Lewis acid sites with an octahedral coordination. The thermal stability of this additional feature suggests that this IR feature is associated with the pyridine adsorption on medium-strength Lewis acid sites. The combination of the current spectral observations suggest that the addition of TiO_2 (anatase) crystallites to γ-Al_2O_3 provide additional medium-strength Lewis acid sites that noticeably alter the surface acidity.

3.1.2 NO_x Uptake Protocol: Functionality and Performance of the TiO_2/Al_2O_3 Support Materials

3.1.2.1 NO_x adsorption on Ti/Al support materials via FTIR spectroscopy

After having analyzed the structural properties of the synthesized support materials, NO_x storage ability was investigated by focusing on the nature of the NO_x species formed during the adsorption of NO_2(g) on the Ti/Al (P1/P2) surfaces.

The evolution and the growth of the stored NO_x species as a function of the surface NO_x coverage at 323 K was monitored through FTIR spectroscopy. The series of IR spectra corresponding to increasing coverages of NO_x on the Ti/Al (P1) and Ti/Al (P2) samples are shown in in Figures 9a and 9b, respectively. In order to have a detailed understanding of the NO_x adsorption data associated with the Ti/Al

(P1/P2) samples, similar adsorption experiments were also conducted on two reference surfaces, γ-Al_2O_3 and TiO_2 (anatase) (Figures 9c and 9d).

3.1.2.1.1 Stepwise NO_2 (g) Adsorption on Ti/Al (P1)

The NO_2 uptake analysis of the Ti/Al (P1) support material (Figure 9a) show resemblance to the reference γ-Al_2O_3 surface (Figure 9c) at 323 K. During the early NO_2(g) adsorption stages, the Ti/Al(P1) material (Figure 9a) presents a strong band at 1230 cm^{-1} which shifts to 1256 cm^{-1} at higher coverages. Concurrently with the increase in the intensity of this band, at higher NO_2 doses, several additional bands appear at 1294, 1582 and 1628 cm^{-1} with shoulders at c.a. 1320, 1464 and 1560 cm^{-1}. In addition, a minor feature located around 1985 cm^{-1} becomes visible. All of these features progressively grow and reach their maximum intensities after the complete saturation of the surface with excess NO_2 (g) (red spectrum, fully saturated sample surface denoted with "S" in Figure 9).

Considering the noteworthy similarities between the data given in Figures 9a and 9c, the FTIR data presented in Figure 9a can be interpreted with the help of the former studies in the literature [66, 87-90]. The major band occurring with the first few initial NO_2 doses around 1230 cm^{-1} and the shoulder at about 1320 cm^{-1} are attributed to the nitrites on the alumina surface. The formation of these nitrites may occur with the disproportionation reaction:

$$6\ NO_2 + Al_2O_3 \rightarrow Al(NO_3)_3 + Al(NO_2)_3 \qquad (3)$$

Further NO_2 doses lead to the oxidation of the surface nitrite species to nitrates. As described in various studies [12, 15, 16, 90], nitrites initially formed on the surface are oxidized to nitrates with the help of NO_2 (ads, g) acting as an oxidizing agent. This can be readily visualized by considering the following reaction:

$$NO_2^-\ (ads) + NO_2\ (g,ads) \rightarrow\ NO_3^-\ (ads) + NO\ (g,ads) \qquad (4)$$

Here, the nitrite ion NO_2^- (oxidation state of N: +3) is the electron donor and becomes oxidized to nitrate NO_3^- (oxidation state of N: +5).

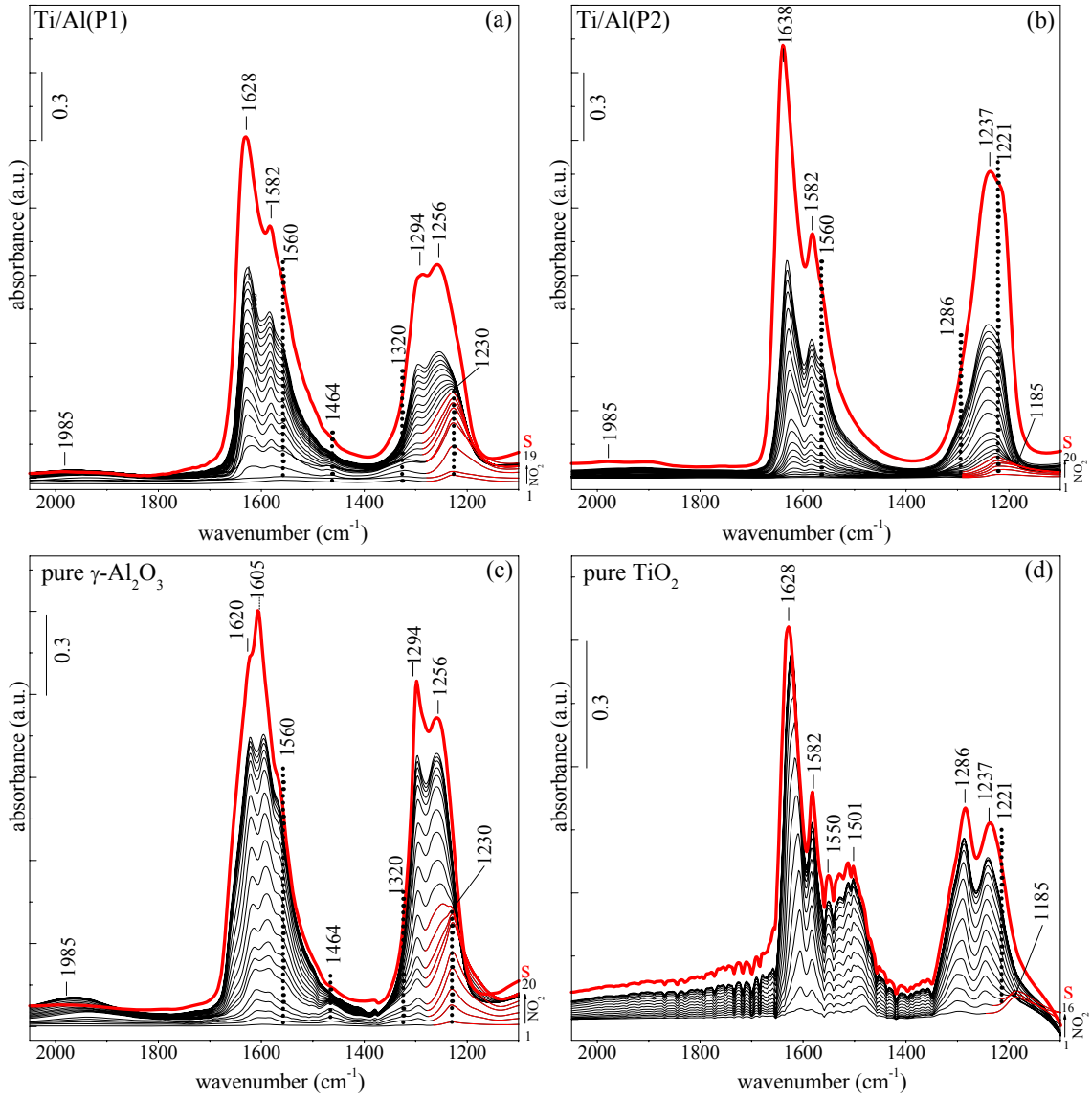

Figure 9. FTIR spectra corresponding to the stepwise NO_2 adsorption at 323 K on (a) Ti/Al (P1), (b) Ti/Al (P2), (c) γ-Al_2O_3 and (d) TiO_2 (anatase) surfaces. The spectrum corresponding to the NO_2-saturated surfaces are marked with ”S”.

The results are in line with the continuous growth and the frequency shift of the nitrite-related feature with the appearance of vibrational features attributed to different types of nitrate species adsorbed on the exposed γ-Al_2O_3 support surface. These different types of nitrate species adsorbed on γ-Al_2O_3 are in the form of bridged (1256 cm^{-1}), bidentate (1294 cm^{-1}) and monodentate nitrates (1464 and 1560 cm^{-1}). Finally, the weak band located at ~1985 cm^{-1} is associated with the weakly adsorbed N_2O_3 on the alumina surface formed by the reaction of NO_2 and NO or possibly associated with the adsorbed NO^+ [91].

Other than the observed similarities between Ti/Al (P1) and γ-Al_2O_3, FTIR data corresponding to the Ti/Al (P1) sample clearly indicate important differences. It is readily visible in Figure 9a that the Ti/Al (P1) sample presents two additional strong features located at 1582 and 1628 cm^{-1}. These additional features appear at the very first NO_2 pulses and further complete their evolution after the saturation of the Ti/Al (P1) surface with NO_2(g). Absence of these additional features in Figure 9c and the suppression of the 1605, 1620, 1256 and 1294 cm^{-1} bands (assigned to bidentate and bridged nitrates on the γ-Al_2O_3 sites) in Figure 9a clearly indicate a relative inhibition of the NO_x uptake of the γ-Al_2O_3 sites on the Ti/Al (P1) surface and the presence of new adsorption sites associated with the TiO_2 domains.

Furthermore, it is apparent that these additional features at 1582 and 1628 cm^{-1} are very similar to those detected in the IR spectra of adsorbed NO_2 on pure anatase (Figure 9d). These bands can also be readily assigned to various types of nitrates on the TiO_2 domains existing on the surface of the Ti/Al (P1) sample. In a former study [93] it was reported that the surface hydroxyl groups take part in the formation of these nitrate structures. The isolated hydroxyl groups of anatase, which possess a basic character are replaced by nitrate anions, while their recombination leads to water formation:

$$2\ \text{Ti-OH} + 3NO_2 \rightarrow 2\ \text{Ti-}NO_3 + H_2O + NO \qquad (5)$$

Based on literature, [92-95] the bands can be attributed to bidentate (1582 cm^{-1}) and bridged (1628 cm^{-1}) nitrates located on the Ti^{4+} sites on the surface. The presence of different nitrate species adsorbed on the Ti/Al (P1) sample with different adsorption sites and adsorption geometries is in agreement with the structure and the

surface acidity of the Ti/Al (P1) system discussed earlier (i.e. existence of additional medium-strength Ti^{4+} Lewis acid sites on Ti/Al (P1)) [1].

The FTIR data discussed above indicate that the presence of TiO_2 (anatase) crystallites on the surface of the alumina particles in the Ti/Al (P1) system significantly influences the nature of the adsorbed NO_x species by providing additional Ti^{4+} NO_x storage sites. However, the suppression of the IR features associated with the nitrates adsorbed on the exposed γ-Al_2O_3 sites of the Ti/Al (P1) surface (together with the BET, XRD and Raman results discussed above) suggests the existence of large TiO_2 crystallites which partially block some of the accessible Al^{3+} surface sites. In other words, the surface morphology of the TiO_2 (anatase) domains relatively hinders the NO_x adsorption ability of the Ti/Al (P1) system with respect to that of the pure γ-Al_2O_3. These arguments are also consistent with the TPD data which will be discussed in detail below in section 3.1.2.1.2.

3.1.2.1.2 Stepwise NO_2 (g) Adsorption on Ti/Al (P2)

The resemblance of the IR spectral characteristics of the Ti/Al (P2) sample (Figure 9b) to that of the reference anatase (TiO_2) material (Figure 9d) suggests that Ti^{4+} storage sites distributed on the Ti/Al(P2) support material surface have a major contribution to the resultant FTIR spectra after the NO_2 adsorption (Figure 9b).

It can be seen in Figure 9b that the initial doses of NO_2 (g) lead to the appearance of a weak band at 1221 cm^{-1} with a shoulder at ~1185 cm^{-1} (these features are highlighted with red in Figure 9b). After successive NO_2 doses, the shoulder at ~1185 cm^{-1} starts to attenuate and this is accompanied by an increase in the intensity of the feature at 1221 cm^{-1}. Moreover, a set of new bands at 1237, 1582, 1638 cm^{-1} and shoulders at ~1286 and 1560 cm^{-1} become apparent. These IR features monotonically increase with increasing NO_2 doses and reach their saturation values after an 8 Torr NO_2 exposure for 20 min at 323 K.

Based on various studies, the bands related with the NO_x adsorption on pure TiO_2 (anatase) [92-95] and Ti/Al (P2) sample (Figure 9b) can be readily assigned. The most prominent band observed during the initial doses at 1221 cm^{-1} (which is also visible as a shoulder in the “S” spectrum) and the band at 1582 cm^{-1} are

attributed to the bidentate nitrates that are bound to TiO_2 particles. The weakly expressed shoulder at about 1185 cm^{-1} is assigned to nitrites coordinated on the Ti^{4+} adsorption centers. In addition, the features located at 1638 and 1237 cm^{-1} are assigned to a different form of nitrates that are bridged on the titania surface. Figure 9b clearly designates the presence of nitrite/nitrates species on the Ti^{4+} adsorption sites. Other than the NO_x species on the titania sites the strong band at 1560 cm^{-1} reveals the presence of monodentate nitrates on the alumina surface.

The IR differences observed for Ti/Al (P2) and pure TiO_2 clearly points out that after the saturation of the surface with NO_x, the band which was originally observed on pure TiO_2 at 1286 cm^{-1} and the group of features at 1500–1550 cm^{-1} is not clearly detected in the IR spectra of the Ti/Al (P2) sample. The missing features according to IR spectroscopy studies on anatase [92-95] were attributed to the presence of monodentate nitrates on the TiO_2 surface. In addition, it was found that the Lewis acid sites on the anatase surface reveal four and five-coordinated Ti^{4+} ions (denoted as α and β sites, respectively) where α-Lewis acid sites (with two oxygen vacancies) favor bidentate/bridge nitrate formation while the β-sites (Ti^{4+} with one oxygen vacancy) favor the formation of monodentate nitrates [92-95].

The above results given in Figure 9b suggest the lack of a significant amount of monodentate nitrate species on the surface of the Ti/Al (P2) support material, in comparison to that observed for the reference anatase material (Figure 9d). Therefore, due to different TiO_2 morphologies on the Ti/Al (P2) sample, most of the Ti^{4+} sites dispersed on the γ-alumina surface can adsorb NO_x mostly in the form of bidentate/bridged nitrates.

Comparison of Figures 9a and 9b, clearly indicates that the NO_x vibrational features related with the titania sites are much more pronounced for the Ti/Al (P2) sample. Moreover, the intense nitrate vibrational features in Figure 9b, may be associated with the higher surface area of the Ti/Al (P2) sample (note that all analyzed samples have identical masses, i.e. ~20 mg). However, it should also be emphasized that these observed differences in the IR intensities may also be arising from the differences in the infrared absorption cross sections of nitrates with different adsorption geometries. It is also worth mentioning that more intense nitrate vibrational signals associated with the Ti^{4+} sites for the Ti/Al (P2) sample also imply the fraction of accessible Ti^{4+} sites on the Ti/Al (P2) surface being greater than that

of the Ti/Al (P1) surface. Simultaneously, these suggestions indicate a better surface dispersion of the Ti^{4+} sites on the Ti/Al (P2) system (possibly due to smaller TiO_2/TiO_x domains on the surface) where a large fraction of these adsorption sites are accessible for NO_2. Thus, it is apparent that the NO_x storage properties of these systems are dictated by the surface morphology and the distribution of the TiO_2 domains present on the alumina support. Furthermore, the difference in the NO_x adsorption properties of the mixed oxide support materials can also be ascribed to the different number of oxygen defect sites and the nature of the surface hydroxyl groups exposed on the surface [96].

The spectral region within 1300 - 1100 cm^{-1} in Figures 9a and 9b reveals that the NO_x uptake process starts with the formation of nitrites at 1230 and 1185 cm^{-1} on the Al^{3+} and Ti^{4+} adsorption sites, respectively. Figures 9a-9d proves that the presence of TiO_2 domains tend to hinder the nitrite formation during the initial NO_x uptake. In other words, the initial nitrite formation is observed to a greater extent on pure γ-Al_2O_3 and decreases as the number of exposed Al_2O_3 surface sites decreases (i.e. γ-Al_2O_3 > Ti/Al (P1) > Ti/Al (P2) > TiO_2-anatese). This relative decrease in the initial nitrite formation could be ascribed to the presence of reactive oxygen species on the TiO_2 domains in the form of oxygen defects [96], or transient oxygen species like O^-, O^{2-} providing an efficient and rapid oxidation of nitrites into nitrates [96].

3.1.2.2 Thermal behavior of the adsorbed NO_x species on Ti/Al support materials via TPD.

Figures 10a and 10b demonstrate the TPD profiles corresponding to the NO_x desorption signals at (m/z) 30, 32 and 46 amu of both support and reference materials.

For the γ-Al_2O_3 surface (the bottommost TPD profiles given in Figure 10) two major desorption features are observed during the thermal evolution [66]. The first major NO_x desorption feature of γ-Al_2O_3 is visible at 389 K while the second major feature has its maximum desorption at 625 K. The lower temperature feature at 389 K is related to the desorption of weakly bound N_2O_3/NO^+ or monodentate nitrate species [87, 88, 93], that desorb in the form of NO_2 and NO + O_2. The second desorption feature at 625 K is associated with the desorption/decomposition of bridging and bidentate nitrates [87, 88] which yield a greater NO_2 desorption signal.

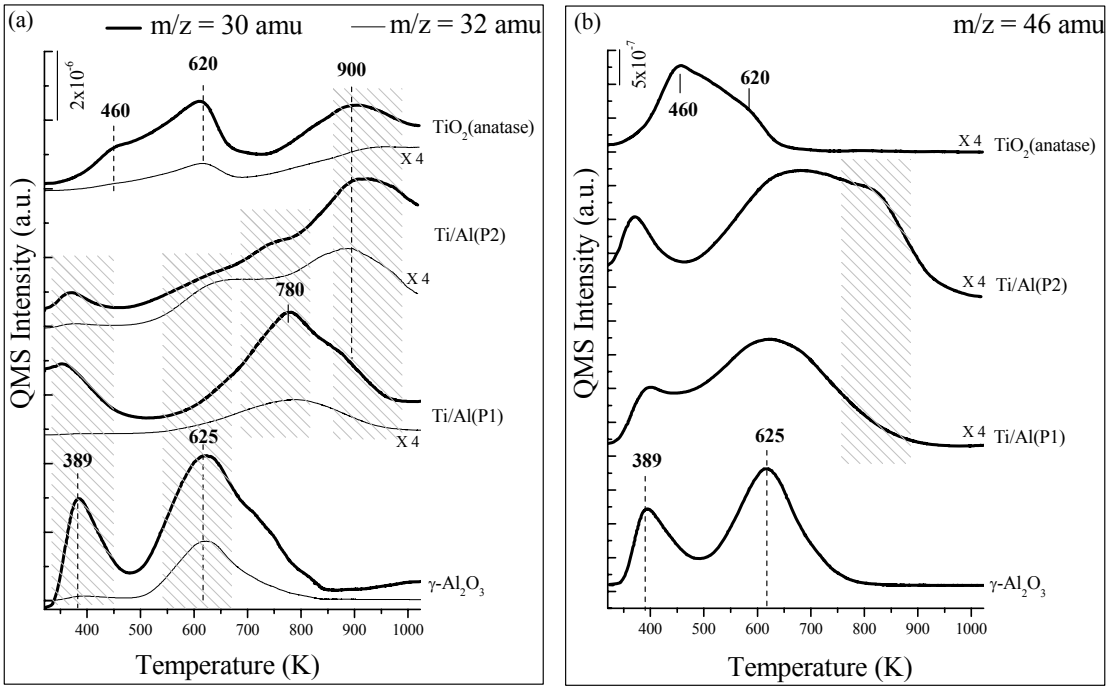

Figure 10. TPD profiles obtained after saturating Ti/Al (P1), Ti/Al (P2), γ-Al_2O_3 and TiO_2 surfaces with NO_2 at 323 K a) 30, 32 amu signals, b) 46 amu signal.

In the NO_x desorption profiles corresponding to the Ti/Al (P1) system, other than the desorption features associated with the alumina surface, an additional strong feature at 780 K is observed which displays an asymmetric structure with a shoulder at ~ 900 K. The intensities of the desorption signals at 389 K and 625 K are considerably suppressed and the TPD profiles are dominated by a new and distinct feature at 780 K.

These new desorption features in the TPD profiles of the Ti/Al (P1) sample at 780 K and at ~ 900 K can be attributed mostly to the decomposition of the bidentate/bridged nitrates on the TiO_2 domains of the Ti/Al (P1) surface. Furthermore, in agreement with the FTIR data for the Ti/Al (P1) system presented above, the presence of Ti^{4+} adsorption sites associated with the TiO_2 domains on the Ti/Al (P1) system (mostly in the form of large crystallites on the alumina surface) results in a decrease in the fraction of accessible Al^{3+} surface sites for NO_x adsorption.

Considering the surface morphology of the Ti/Al (P1) sample which is composed of mostly large TiO_2 domains, the feature at 780 K can be associated with the nitrate decomposition from the isolated and large (bulk-like) TiO_2 clusters. Moreover, the shoulder at ~ 900 K can be attributed to the NO_x desorption from the less-abundant TiO_2 domains more homogenously distributed on the surface. These assignments are also consistent with the desorption characteristics of the pure TiO_2 (anatase nano-powder with an average particle size of 40 nm and a surface area of 45 m^2/g) and the Ti/Al (P2) samples presented in Figure 10.

The TPD profile of the TiO_2 reference sample (the topmost profiles given in Figure 10a and 10b) presents a weak shoulder at 460 K and two broad features located at 620 K and 900 K. In the light of the FTIR results presented above and those reported in numerous former studies in the literature [92-95], the temperature range corresponding to the first and second feature at 460 K and 620 K are attributed to the desorption of the monodentate nitrates with a relatively minor contribution from the weakly physisorbed molecular species whereas the feature 900 K is assigned to the decomposition of the bridged/bidentate nitrates, respectively. However, the feature at ~ 780 K is not clearly visible for the reference TiO_2 sample, as it is for the Ti/Al (P1) system. Thus, it can be concluded that the existence of at least two different types of nitrate species with distinctively different thermal

stabilities on the titania domains of the Ti/Al (P1) sample seems to be closely connected with the morphology of the TiO_2 crystallites. The lower temperature decomposition at 780K is mostly from the surface of the isolated (bulk-like) TiO_2 clusters on the Ti/Al (P1) sample. On the other hand, the nitrates coordinated on the TiO_2 domains that are homogenously distributed on the surface by forming well-dispersed TiO_x units decompose at higher temperatures (c.a. 900 K). Both of these nitrate species decompose by mostly releasing NO (g). This interpretation is also consistent with the TPD profiles of the Ti/Al (P2) sample, presented in Figures 10a and 10b. TPD profiles of the Ti/Al (P2) sample show that the nitrate desorption features associated with the Al^{3+} adsorption sites located at 625 K are more visible for the Ti/Al (P2) sample. Furthermore, TPD profile for the Ti/Al (P2) material suggests that the intensity of the desorption feature at ~900 K (that is ascribed to the presence of thermally stable nitrates on well-dispersed TiO_2/TiO_x domains), is significantly greater than the desorption signal of the nitrates associated with the isolated (bulk-like) TiO_2 clusters. Based on the overall observations, it is apparent that the Ti/Al (P2) sample exhibits a surface structure with a greater number of Ti^{4+} and Al^{3+} sites that are available for NO_x adsorption. Considering the thermal evolution of the adsorbed NO_x species, the relative stabilities of the stored NO_x species can be ranked in the following increasing order: N_2O_3 on Al^{3+} or Al_2O_3 sites << nitrates on Al^{3+} or Al_2O_3 sites < nitrates on isolated (bulk-like) TiO_2 clusters < nitrates on well-dispersed TiO_2/TiO_x domains.

3.1.3 SO_x Uptake of TiO_2 promoted Al_2O_3 catalytic support materials

3.1.3.1 FTIR Study of SO_x interaction with Ti/Al support under lean conditions

Numerous former studies in literature [97, 98] focus on the interaction of dioxide (SO_2 (g)) with the alumina (Al_2O_3) surface. Typically, SO_2 (g) binds to the basic sites on alumina (Al_2O_3) to form adsorbed sulfite (SO_3^{2-}) species which is further converted to sulfate (SO_4^{2-}) up on oxidation. A former study in the literature [99] investigated the interaction of SO_2 with γ-Al_2O_3 using FTIR technique. This study indicates that after exposing the surface to SO_2 (g), IR bands related with both weakly and strongly adsorbed SO_2 species become apparent. Thus, the adsorption of SO_2 (g) on the basic adsorption sites is followed by a cleavage of an Al-O bond on the surface (primarily at OH sites/exposed oxygen atoms, O^{2-}) that leads to the formation of chemisorbed SO_3^{2-}, while adsorption at acidic sites (i.e. coordinately unsaturated aluminium cations, Al^{3+}) form physisorbed SO_2. The oxidation of adsorbed SO_3^{2-}/SO_2 in oxygen at relatively high temperatures (673-773 K) gives rise to two strong intense adsorption bands related with surface sulfate species [98]. In order to elucidate different types of SO_x species formed on the Ti/Al (P1/P2) surfaces, SO_2 (g) + O_2 (g) adsorption experiments at different experimental conditions were performed via FTIR. Analogous experiments were also conducted on γ-Al_2O_3 and TiO_2 (anatase) as a benchmark samples for comparison.

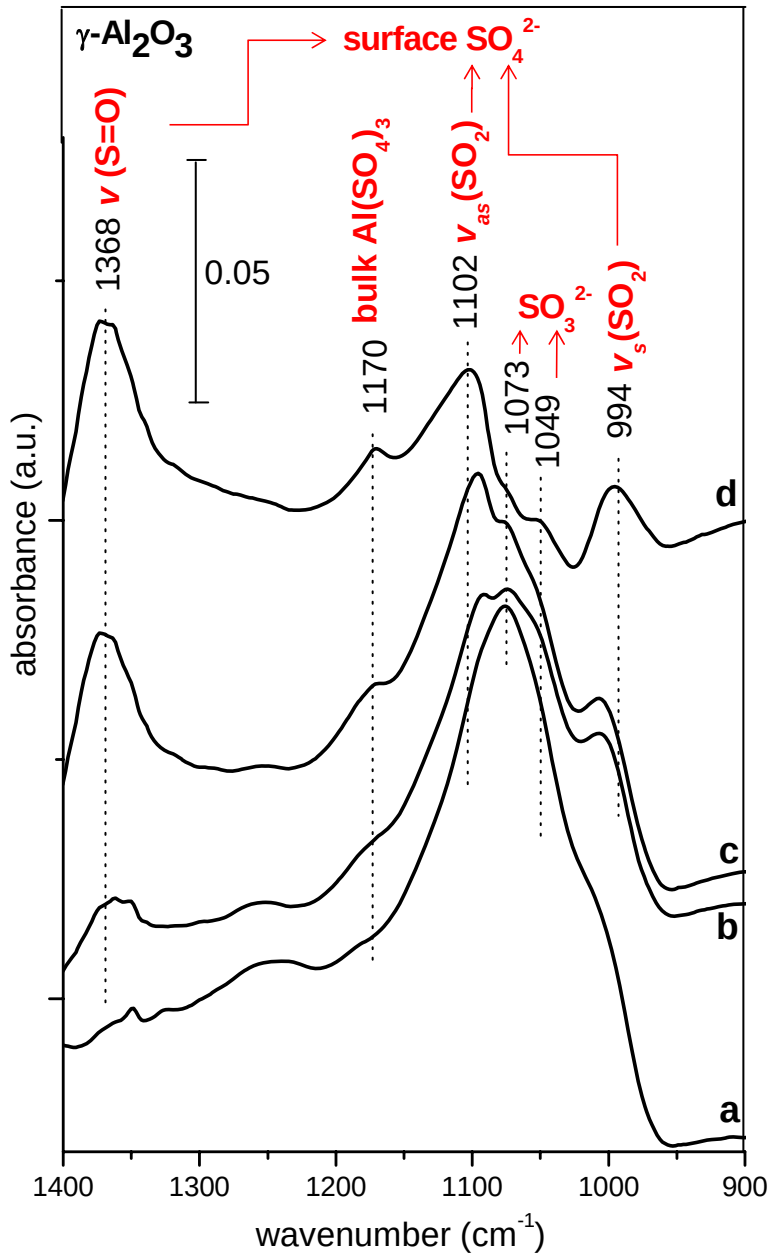

Figure 11. FTIR spectra for SO_2 (g) + O_2 (g) (SO_2:O_2, 0.1:1) co-adsorption on γ-Al_2O_3. **a)** After 1 h exposure to SO_2 (g) + O_2 (g) at 323 K (spectrum was obtained in the presence of the gas mixture), **b)** after flashing the sample in (a) to 473 K in SO_2 + O_2 and cooling to 323 K (spectrum was obtained in the presence of the gas mixture), **c)** after flashing the sample in (b) to 673 K in SO_2 (g) + O_2 (g) and further evacuation at 323 K for 20 min ($P_{reactor} < 1\times10^{-4}$ Torr) , **d)** after flashing the sample in (c) to 673K in vacuum ($P_{reactor} < 1\times10^{-4}$ Torr) and cooling to 323 K.

Davydov [100] reported that in the presence of O_2 (g), the interaction of SO_2 (g) with various oxide surfaces lead to the formation of sulfates having various adsorption configurations. Our current IR results (data not shown) regarding the adsorption of pure SO_2 (g) on γ-Al_2O_3 are in very good agreement with the former investigations in the literature, revealing the formation of sulfites (SO_3^{2-}), without any additional oxidation to sulfates. On the other hand, in accordance with the former reports in the literature, our studies (data not shown) also indicate that SO_2 (g) is readily oxidized to the stable sulfate (SO_4^{2-}) species on γ-Al_2O_3 in the presence of excess O_2 (g) (i.e. under lean conditions) and at high temperatures ($T \geq 473$ K).

The adsorption of SO_2 (g) + O_2 (g) on the γ-Al_2O_3 surface (Figure 11 spectrum *a*) reveals a major broad band at 1073 cm^{-1} as well as weaker and poorly-defined additional features around 1350, 1250 and 1000 cm^{-1}. In Figure 11 (spectra *a* and *b*), the presence of SO_3^{2-} species are evident due to characteristic sulfite features at c.a. 1073 cm^{-1} and the shoulder at 1049 cm^{-1}. As the adsorption temperature increases to 473 K (Figure 11, spectrum *b*) the 1368, 1170, 1102 and 1000 cm^{-1} bands become more intense. Two of the minor bands in Figure 11 (spectra *a* and *b*) around 1350 (ν_{as}, S-O) and the broad band at 1150 cm^{-1} (ν_s, S-O) are assigned to weakly adsorbed molecular SO_2 in agreement with the former reports in the literature [97, 98, 100, 101]. It is also evident that the ν (S=O) surface sulfate at 1368cm^{-1} starts growing after heating to 473 K. The band at 1250 cm^{-1}, might probably be associated with bidentate sulfate species, which transform into bulk $Al_2(SO_4)_3$ (1170 cm^{-1}) with increasing temperature (Figure 11, spectrum *d*). After flashing the sample to 673 K and evacuating at 323 K for 20 min (Figure 11, spectra *c* and *d*) the weakly adsorbed molecular SO_2 species (1350, 1150 cm^{-1}) on the γ-Al_2O_3 surface are replaced by SO_x species (1368, 1170, 1102 and 994 cm^{-1}). The FTIR spectra reveal minor changes after heating the sample to 673 K in vacuum (Figure 11, spectrum *d*). In Figure 11 (spectrum *d*), the dominating features are 1368 cm^{-1} (ν (S=O)), 1102 cm^{-1} (ν_{as} (SO_2)) and 994 cm^{-1} (ν_s (SO_2)). The bands observed at 1073 and 1049 cm^{-1} in Figure 11 (spectrum *d*) which were attributed to tri-coordinated sulfite species become less pronounced in the presence of sulfates. An additional minor feature is also visible after flashing the sample at $T \geq 473$ K (Figure 11, spectra *c* - *d*), indicating the presence of bulk $Al_2(SO_4)_3$ (1170 cm^{-1}). These results indicate that sulfites and sulfates are initially formed on the surface at the beginning of the SO_2 (g)

+ O_2 (g) co-adsorption and at elevated temperatures these species are converted into relatively stable surface sulfates (SO_4^{2-}/Al_2O_3) as well as bulk $Al_2(SO_4)_3$.

A similar study by Abdulhamid [102] showed that SO_2 adsorption on an alumina sample formed both surface aluminum sulfate (1318 cm^{-1}) and sulfite (972 cm^{-1}) species. According to Saur et al. [103], surface aluminum sulfate is characterised by two peaks with frequencies around 1380 and 1035 cm^{-1}. In the literature, there is an active debate on the vibrational spectroscopic assignments of various SO_x species. For example, Uy and Chang et al. [31, 98] allocate the 1035 cm^{-1} frequency to a bulk-like form of sulfate, whereas in most of the former studies, this has been assigned to the low-frequency (v_1) mode of the surface SO_4^{2-}/Al_2O_3 while the bulk form of $Al_2(SO_4)_3$ was suggested to appear at much higher frequencies around 1150 cm^{-1} (Table 4).

Table 4. Infrared Bands Assigned to SO_x species [31, 100, 103, 104, 107, 124-126]

Species	***Symmetry***	***$v_1(v_s)(cm^{-1})$***	***v_3 (v_{as})(cm^{-1})***	***References***
SO_2 (gas)	C_{2v}	1151	1362	[107]
SO_3^{2-}	C_{3v}	961	1010-1050	[100,107]
Free ion SO_4^{2-}	T_d	-	1104	[107]
Surface sulfates:				
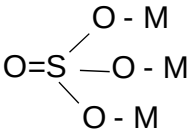	C_{3v} *M=Ti*	1045,1005	1370	[103]
	M=Al	1045	1380	
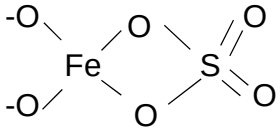	C_{2v}	1212,1190	1400	[103]
$BaSO_4$ (surf)		1060	1120	[124,125,126]
Bulk- like sulfates:				
$Al_2(SO_4)_3$		1130-1190		[31]
$BaSO_4$ (s)		1162	1242	[104]

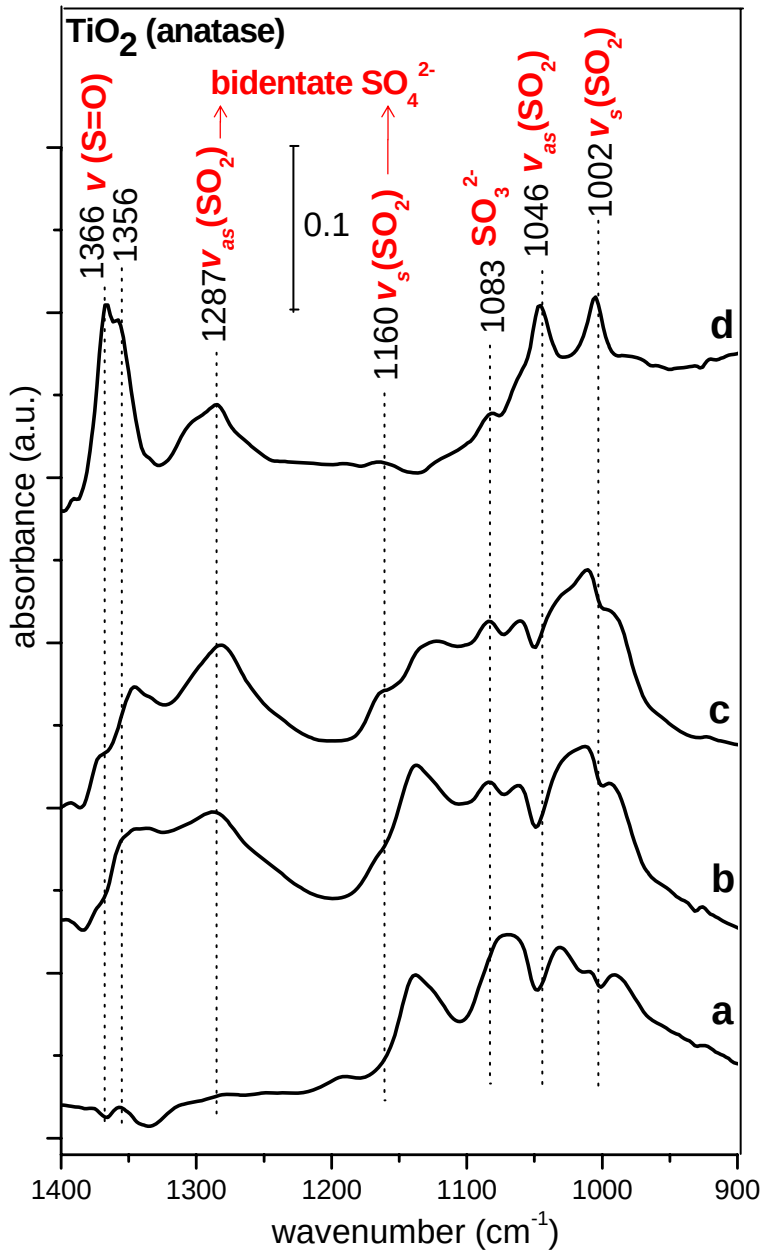

Figure 12. FTIR spectra for SO_2 (g) + O_2 (g) (SO_2:O_2, 0.1:1) co-adsorption on TiO_2 (anatase). **a)** After 1 h exposure to SO_2 (g) + O_2 (g) at 323 K (spectrum was obtained in the presence of the gas mixture), **b)** after flashing the sample in (a) to 473 K in SO_2 + O_2 and cooling to 323 K (spectrum was obtained in the presence of the gas mixture), **c)** after flashing the sample in (b) to 673 K in SO_2 (g) + O_2 (g) and further evacuation at 323 K for 20 min ($P_{reactor} < 1\times10^{-4}$ Torr), **d)** after flashing the sample in (c) to 673K in vacuum ($P_{reactor} < 1\times10^{-4}$ Torr) and cooling to 323 K.

In order to examine the sulfur accumulation on the TiO_2 (anatase) surface, FTIR spectra of SO_2 (g) + O_2 (g) treated anatase samples were obtained (Figure 12) in similar conditions as for the γ-Al_2O_3 sample (Figure 11). It was confirmed that SO_2 was chemisorbed on the TiO_2 under lean (oxidizing) conditions and converted into $Ti(SO_4)_2$ at elevated temperatures. A number of former studies [98, 103-105] point out that the adsorption of sulfates on oxides lead to a relatively invariant frequency difference of about 300 cm^{-1} between the symmetric and antisymmetric stretching modes of the SO_2 group [106]. Along these lines, the broad low-frequency band at c.a. 1050 cm^{-1} can be attributed to the vibrational strectcing modes of the M-O-S framework (M = Ti, Al Table 4). It is worth mentioning that the infrared spectrum of bulk aluminium sulfate (hydrated or anhydrous) is very different from the sulfated Al_2O_3 in terms of ν(SO) stretching features which lie between 1250-1000 cm^{-1} (and agrees with the typical vibrational frequencies observed for ionic SO_4^{2-} species). Similarly, the spectrum of solid $TiOSO_4$ is also very different from that of sulfated TiO_2.

It is apparent in Figure 12 that the spectra *a-c* have broad and overlapping sulfite (1083 cm^{-1}) and sulfate features which are located within 1100- 950 cm^{-1}. During thermal treatment steps at T $\geq$ 473K, it is visible that the 1400-1300 cm^{-1} region becomes more pronounced with an additional broad doublet having maxima at 1046 and 1002 cm^{-1} (ν_{as} (SO_2) and ν_s (SO_2) respectively). These features can be associated with the surface sulfates on TiO_2 (i.e. SO_4^{2-}/TiO_2). All of the adsorbed SO_x species mentioned above as well as the less pronounced features around 1287 cm^{-1} (ν_{as} (SO_2), bidentate sulfate) [107-109], 1160 cm^{-1} (ν_s (SO_2)) indicate the existence of bidentate SO_4^{2-} species on the anatase surface [101]. According to a former report [110] based on SO_2 poisoning on Ce/TiO_2 [101, 111] with SO_2 (g), sulfate groups binding to different surface sites, namely Ce-Ce or Ce-Ti, reveal a doublet in the IR spectrum with maxima at 1363 and 1309 cm^{-1}. Thus the doublet in Figure 12, spectrum *d*, located at 1366 cm^{-1} and 1356 cm^{-1} (ν (S=O)) may be ascribed to sulfate species that are interacting with Ti sites with different oxidation states such as Ti^{4+} / Ti^{3+} or Ti sites with different coordination numbers such as the regular octahedral Ti^{4+} sites or $Ti^{4+/3+}$ interstitial defect sites. It should be noted that such a doublet is not visible in similar experiments performed on γ-Al_2O_3 (Figure 11) which

is in agreement with the smaller number of oxygen vacancies on the alumina surface as well as the existence of a uniform oxidation state of +3 for the Al sites.

It is clear from both Figures 11d and 12 d that the SO_x species in the form of surface sulfates become more pronounced for both γ-Al_2O_3 and TiO_2 at 673K. It should be noted that as for many other metal oxides, γ-Al_2O_3 and TiO_2 surfaces also have a large number of overlapping SO_x features within 1400 - 900 cm^{-1} [97, 100, 101, 104].

Figures 13a and 13b show the IR spectra of the Ti/Al (P1) and Ti/Al (P2) mixed support materials after treatment in SO_2 (g) + O_2 (g) at different temperatures (473 K - 673 K) and the formation of different SO_x species.

The IR profiles of the SO_2 (g) + O_2 (g) coadsorption at 323 K on the binary oxide Ti/Al (P1, P2) support materials (spectra *i and ii* in Figure 13) show some resemblances. The main difference arises from the existence of the shoulder around c.a. 1130 cm^{-1} for the Ti/Al (P1) sample (spectra *i and ii* in Figure 13a). In other words, when Ti/Al (P1) and Ti/Al (P2) are exposed to SO_2 (g) + O_2 (g) at low temperatures (i.e. $T < 473$ K), predominant SO_x species on these surface seem to be sulfites while sulfates are also probably observed on both surfaces to a certain extent, particularly on the Ti/Al (P1) surface. Furthermore, the presence of weakly adsorbed molecular SO_2 species can not be excluded either for both surfaces. With increasing temperature to 673 K in the presence of SO_2 (g) + O_2 (g), additional features start to grow for both Ti/Al (P1) and Ti/Al (P2), predominantly at c.a. 1050 and 1350 cm^{-1} which can be attributed to surface sulfates. Thus it is readily seen that sulfites are oxidized to sulfates at $T \geq 673$ K on both surfaces. It is also evident in spectra *iv* of Figures 13a and 13b that, intensities of the bidentate sulfate features (1160 - 1170 cm^{-1} and 1235 - 1265 cm^{-1}) reach higher values for the Ti/Al (P2) sample after SO_2 (g) + O_2 (g) exposure at $T \geq 673$ K.

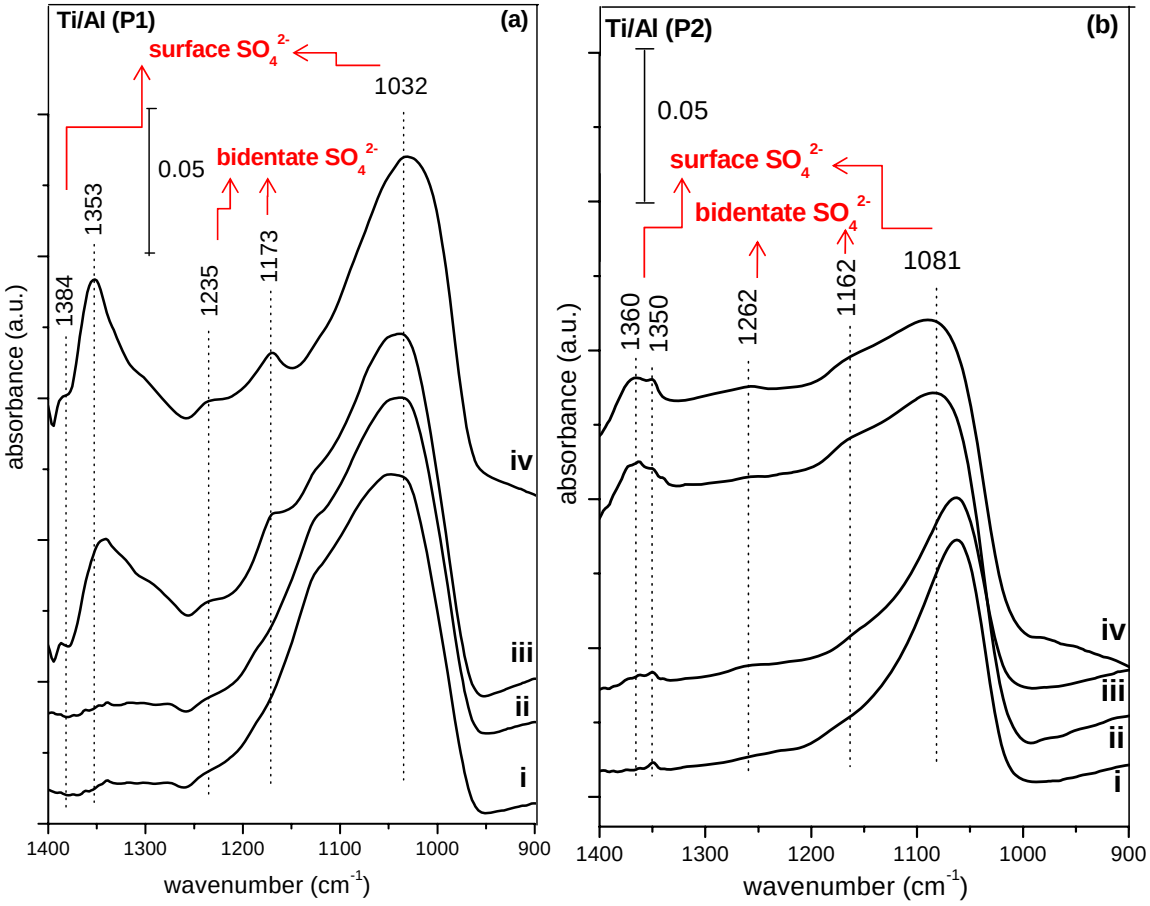

Figure 13. FTIR spectra for SO_2 (g) + O_2 (g) (SO_2:O_2, 0.1:1) co-adsorption on a) Ti/Al (P1) and b) Ti/Al (P2) i**)** After 1 h exposure to SO_2 (g) + O_2 (g) at 323 K (spectrum was obtained in the presence of the gas mixture), **ii)** after flashing the sample in (a) to 473 K in SO_2+O_2 and cooling to 323 K (spectrum was obtained in the presence of the gas mixture), **iii)** after flashing the sample in (b) to 673 K in SO_2 (g) + O_2 (g) and further evacuation at 323 K for 20 min ($P_{reactor} < 1\times10^{-4}$ Torr), **iv)** after flashing the sample in (c) to 673K in vacuum ($P_{reactor} < 1\times10^{-4}$ Torr) and cooling to 323 K.

High temperature SO_2 (g) + O_2 (g) exposure also seem to trigger the growth of the 1160-1170 cm^{-1} and 1230-1260 cm^{-1} features on both samples which may indicate the formation of either bidentate sulfates or bulk $Al_2(SO_4)_3$ and/or $TiOSO_4$.

It is also worth emphasizing that on the Ti/Al (P2) sample, after exposure to SO_2 (g) + O_2 (g) at 673 K, the high frequency sulfate feature at ~1350 cm^{-1} is observed to split into a doublet form as in the case of pure TiO_2 (Figure 12). However, TiAl (P1) has a more dominating 1353 cm^{-1} (ν S=O) surface sulfate feature with an additional shoulder at 1384 cm^{-1} (no splitting observed). This observation suggests that the Ti/Al (P2) sample has a higher dispersion of TiO_2/TiO_x domains on its surface in agreement with the discussion given in the previous sections.

3.1.3.2 Influence of SO_2 poisoning on the NO_x adsorption behavior of the Ti/Al Systems via FTIR Spectroscopy

The NO_x uptake experiments on the freshly prepared materials were discussed in detail in the previous sections. Thus, in order to have a better understanding of the synthesized support materials and the relevant reference oxide surfaces (i.e. γ-Al_2O_3 and TiO_2) the NO_x uptake behaviors of the poisoned surfaces were investigated via FTIR spectroscopy. In addition, the NO_x storage capacities of these poisoned surfaces were also thoroughly compared with the NO_x uptake properties of the fresh samples as well.

Figure 14 compares the NO_x uptake behaviors of the fresh and poisoned γ-Al_2O_3 surfaces at 323 K. As mentioned during the discussion of the data given in Figure 9c, after the saturation of the fresh γ-Al_2O_3 surface with NO_2 (g), vibrational features associated with different types of nitrate species were observed. These different types of nitrate species adsorbed on γ-Al_2O_3 were in the form of bridged (1258, 1628 cm^{-1}), bidentate (1300, 1604 cm^{-1}) and monodentate nitrates (1300, 1564 cm^{-1}) [87-89]. Additionally, the weak band located at ~1958 cm^{-1} was associated probably with the adsorbed NO^+ and/or weakly adsorbed N_2O_3 on the alumina surface formed by the reaction of NO_2 and NO [91].

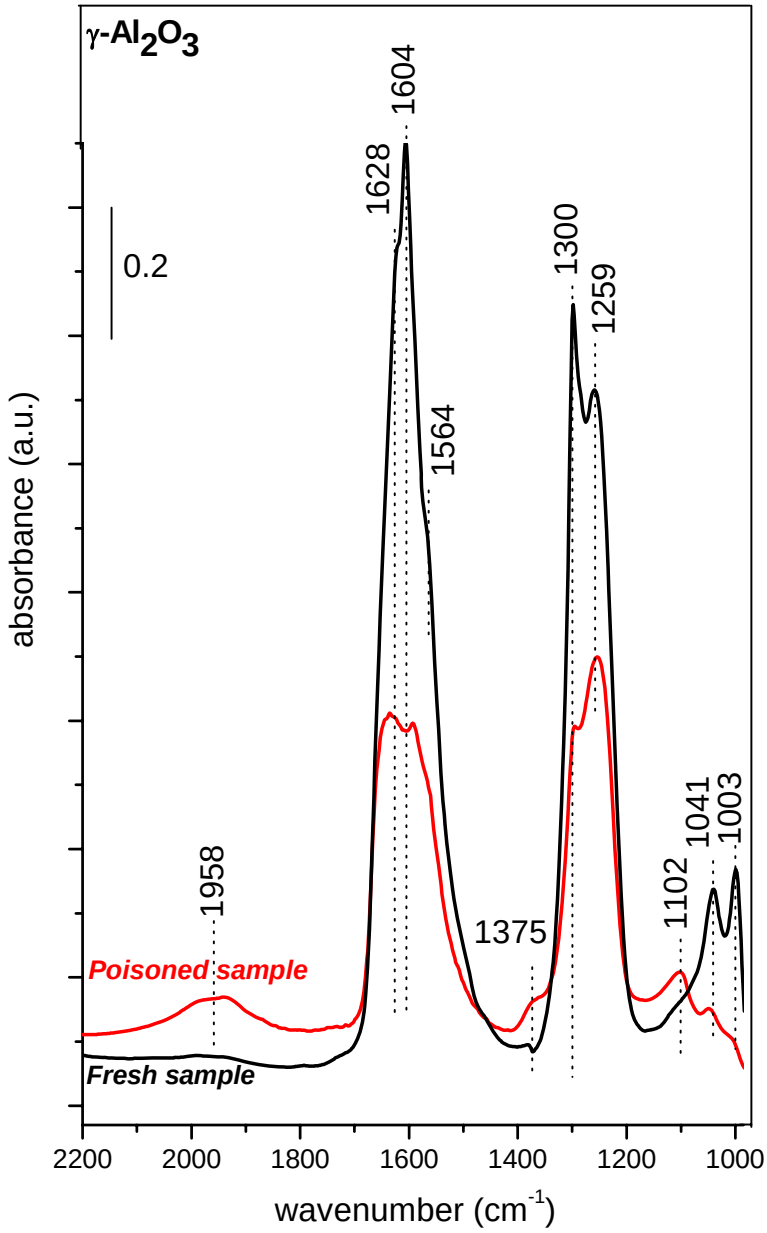

Figure 14. FTIR spectra corresponding to NO_2 (g) adsorption at 323 K on fresh (black spectrum) and poisoned (red spectrum) γ-Al_2O_3 surface. Poisoning of the surface was performed by exposing γ-Al_2O_3 to SO_2 (g) + O_2 (g) (SO_2:O_2, 0.1:1) at 323 K, followed by heating of the sample in the gaseous mixture at 473 K for 30 min and a final evacuation at 323 K ($P_{reactor} < 1x10^{-3}$ Torr). NO_x uptake of the fresh and poisoned surfaces were performed by exposing the samples to 8 Torr of NO_2 at 323 K for 20 min, followed by evacuation of the reactor to $< 1x10^{-3}$ Torr. All of the FTIR spectra were acquired in vacuum at 323 K.

The poisoning of the γ-Al_2O_3 surface by SO_2 (g) + O_2 (g) lowers the NO_x adsorption capacity of the surface and thus the formation of adsorbed nitrate species. It can be readily seen that poisoning of the sample alters the line shape of the IR spectra together with the quantity as well as the nature of the nitrates on the γ-Al_2O_3 surface, mostly yielding bridged nitrates. As shown in Figure 14, the appearance of absorption bands at 1375 and 1100 cm^{-1} reveal formation of surface SO_4^{2-}/Al_2O_3 at 323 K. It should be noted that although sulfate formation on the γ-Al_2O_3 surface in the absence of NO_x species (Figure 11) requires a relatively high temperature (i.e. 673 K), sulfate formation can occur at temperatures as low as 473 K in the presence of NO_x species. Thus, it is evident that NO_x species function as efficient oxidizing agents in the oxidation of the SO_x species on the γ-Al_2O_3 surface to sulfates at low temperatures (473 K). Some of the plausible interaction pathways of surface SO_x species with the adsorbed NO_x species on γ-Al_2O_3 are given below.

$$SO_3^{2-}\,(ads) + NO_2\,(ads, g) \rightarrow SO_4^{2-}\,(ads) + NO\,(g) \qquad (6)$$

$$SO_3^{2-}\,(ads) + 2\,NO_2\,(ads, g) \rightarrow SO_4^{2-}\,(ads) + NO_2^{-}\,(ads) + NO^{+}\,(g) \qquad (7)$$

$$3NO_3^{-}\,(ads) + SO_2\,(ads) \rightarrow SO_4^{2-}\,(ads) + NO_2^{-}\,(ads) + N_2O_3\,(ads,g) + O_2\,(g) \qquad (8)$$

Pathway (6, 7) suggests that the sulfite species on the γ-Al_2O_3 surface that are formed after the poisoning can be directly oxidized to sulfates with the help of weakly adsorbed molecular NO_2 or NO_2 (g). On the other hand, pathway (8) proposes an alternative route to sulfate formation, where surface nitrate species facilitate the oxidation of weakly adsorbed molecular SO_2 species. In this latter route, during the sulfate formation, nitrates are consumed at the expense of nitrite and N_2O_3 generation. These routes are particularly supported by the FTIR spectrum corresponding to the poisoned sample in Figure 14. In this spectrum, it is clearly visible that the NO_2 (g) adsorption on the poisoned surface leads to a feature at 1958 cm^{-1} which is not present in the corresponding spectrum for the fresh sample. This feature can readily be assigned to NO^+ (pathway 7) or N_2O_3 (ads) (pathway 8). An additional support for the latter pathway also comes from the change in the line shape of the spectra upon poisoning. It is apparent in Figure 14 that for the fresh γ-

Al_2O_3 surface, the intensity ratio between nitrate features located at 1300 and 1259 cm^{-1} features are in the favor of the 1300 cm^{-1} feature. On the other hand, for the poisoned sample this trend is reversed and the sample surface is covered by the bridged nitrates (1259 cm^{-1}).

Figure 15, presents analogous poisoning experiments conducted on the TiO_2 (anatase) reference material. As discussed above, for the fresh sample the Lewis acid sites on the anatase surface reveal four and five-coordinated Ti^{4+} ions (denoted as α and β sites, respectively) where α-Lewis acid sites (with two oxygen vacancies) favor bidentate/bridge nitrate formation while the β-sites (Ti^{4+} with one oxygen vacancy) favor the formation of monodentate nitrates [92-95]. A very similar behavior is also visible for the poisoned anatase sample marked in red in Figure 15, though with reduced intensities for NO_x vibrational signals.

Furthermore, poisoned sample also shows some additional bands at 1030 - 1070 cm^{-1} that are associated with the overlapping sulfite and sulfate species and one more shoulder at 1359 cm^{-1} due to $TiOSO_4$ species.

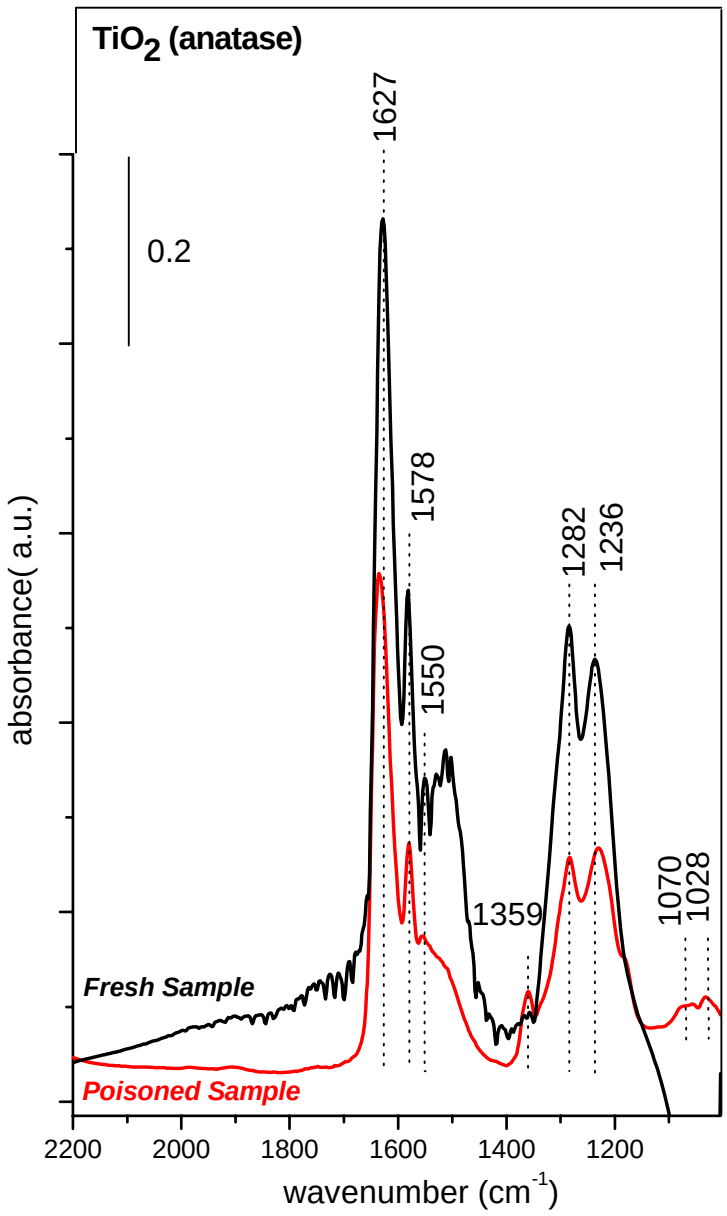

Figure 15. FTIR spectra corresponding to NO_2 (g) adsorption at 323 K on fresh (black spectrum) and poisoned (red spectrum) TiO_2 (anatase) surface. Poisoning of the surface was performed by exposing TiO_2 to SO_2 (g) + O_2 (g) (SO_2:O_2, 0.1:1) at 323 K, followed by heating of the sample in the gaseous mixture at 473 K for 30 min and a final evacuation at 323 K ($P_{reactor} < 1x10^{-3}$ Torr). NO_x uptake of the fresh and poisoned surfaces were performed by exposing the samples to 8 Torr of NO_2 at 323 K for 20 min, followed by evacuation of the reactor to $< 1x10^{-3}$ Torr. All of the FTIR spectra were acquired in vacuum at 323 K.

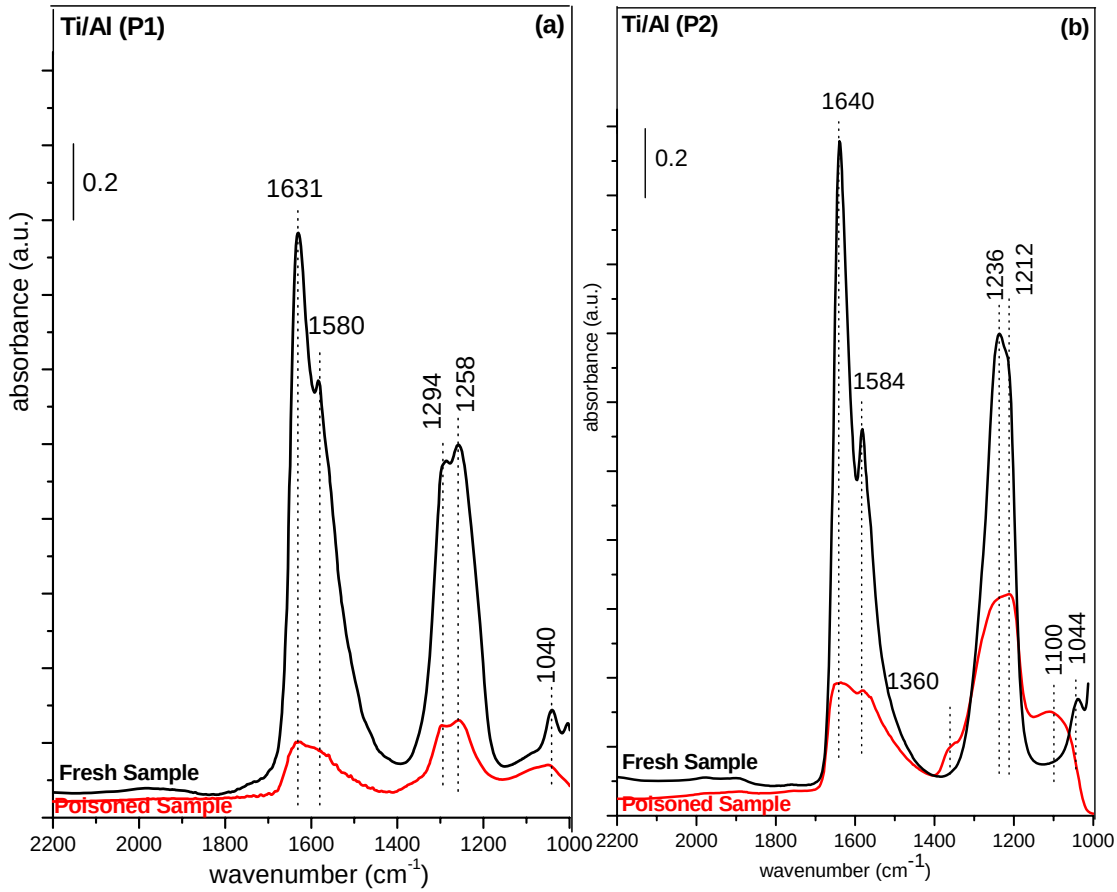

Figure 16. FTIR spectra corresponding to NO_2 (g) adsorption at 323 K on fresh (black spectra) and poisoned (red spectra) **a)** Ti/Al (P1) and **b)** Ti/Al (P2) samples. Poisoning of the surfaces were performed by exposing the samples to SO_2 (g) + O_2 (g) (SO_2:O_2, 0.1:1) at 323 K, followed by heating of the samples in the gaseous mixture at 473 K for 30 min and a final evacuation at 323 K ($P_{reactor} < 1x10^{-3}$ Torr). NO_x uptake of the fresh and poisoned surfaces were performed by exposing the samples to 8 Torr of NO_2 at 323 K for 20 min, followed by evacuation of the reactor to $< 1x10^{-3}$ Torr. All of the FTIR spectra were acquired in vacuum at 323 K.

The mixed binary oxides Ti/Al (P1, P2) and their NO_x adsorption properties after poisoning experiments are shown in Figure 16. It is readily seen in Figure 16 that the NO_x uptake is suppressed after poisoning of both surfaces.

The NO_2 uptake analysis of the Ti/Al (P1) fresh support material (Figure 16a) reveals that NO_x uptake of the Ti sites (1650 - 1550 cm^{-1}) are more significantly suppressed than that of the Al sites (1300-1250 cm^{-1}) as evident from the reversal in the intensity ratio of the 1650 - 1550 cm^{-1} features to 1300-1250 cm^{-1} features. This rather preferential suppression of the NO_x uptake of the Ti sites is even more discernible in Figure 16b which is consistent with the greater extent of TiO_2/TiO_x domains on Ti/Al (P2). It is also worth mentioning that the formation of surface sulfate species are also more pronounced on Ti/Al (P2) due to the presence of stronger 1369 cm^{-1} and 1100 cm^{-1} features.

In terms of the relative total NO_x uptake of these two different support materials after poisoning under identical conditions, it can be argued that Ti/Al (P2), has a slightly higher NO_x uptake after poisoning, probably due to the lower concentration of SO_x species (Figure 13 b).

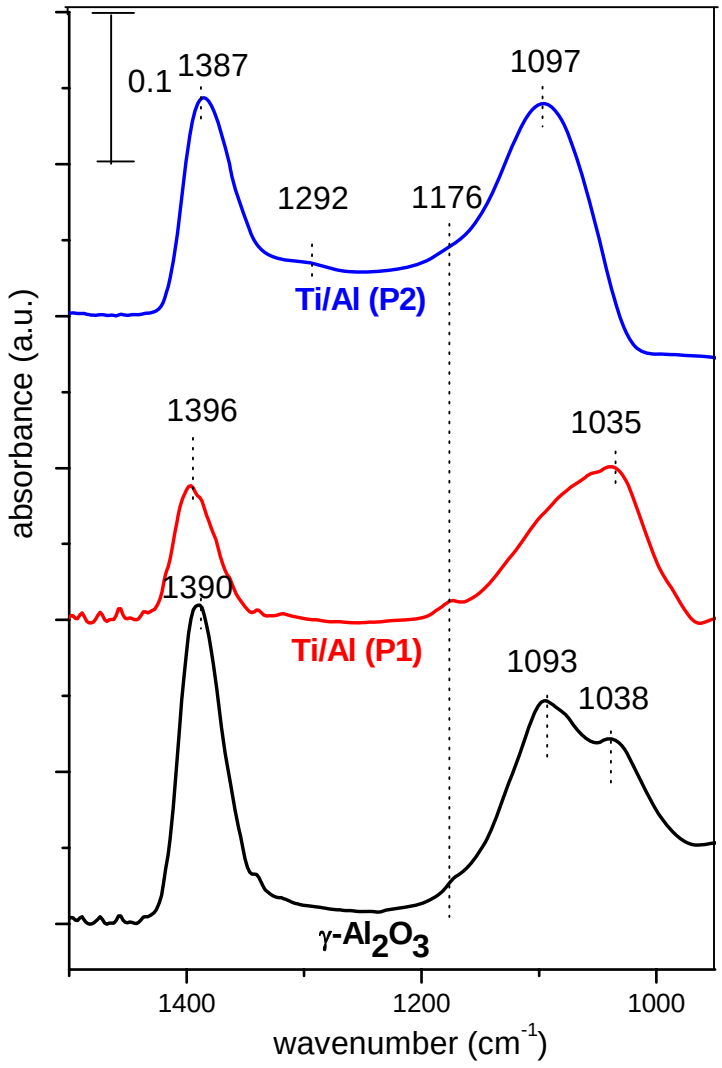

Figure 17. Comparison of the FTIR spectra revealing the species remaining on the γ–Al_2O_3 (black spectrum), Ti/Al (P1) (red spectrum) and Ti/Al (P2) (blue spectrum) surfaces after a procedure consisting of SO_x poisoning, NO_x saturation and evacuation/desorption at 1023 K. Poisoning of the surfaces were performed by exposing the samples to SO_2 (g) + O_2 (g) (SO_2:O_2, 0.1:1) at 323 K, followed by heating of the samples in the gaseous mixture at 473 K for 30 min and a final evacuation at 323 K ($P_{reactor} < 1x10^{-3}$ Torr). NO_x uptake of the fresh and poisoned surfaces were performed by exposing the samples to 8 Torr of NO_2 at 323 K for 20 min, followed by evacuation of the reactor to $< 1x10^{-3}$ Torr at 1023 K. All of the FTIR spectra were acquired in vacuum at 323 K.

Figure 17 displays the highly stable surface species that can survive after a rather vigorous pretreatment protocol which includes poisoning of the γ–Al_2O_3 (black spectrum), Ti/Al (P1) (red spectrum), Ti/Al (P2) (blue spectrum) samples, followed by the saturation of the samples with NO_2 at 323 K and a final evacuation at 1023 K in vacuum. After this elevated temperature pretreatment, only the sulfate species seem to be present on all of the investigated surfaces.

The IR spectra of γ–Al_2O_3 displays two bands appearing in the 1100-1000 cm^{-1} region, with maxima at 1040 and 1090 cm^{-1} suggesting the presence of both $Al_2(SO_4)_3$ and $Al_2(SO_3)_3$, unlike Ti/Al (P1, P2) which contain predominantly surface sulfates. Additionally, the anti-symmetrical stretching mode (ν_3) of the surface sulfate feature at 1390 cm^{-1} is characterized by a relatively higher intensity on the γ–Al_2O_3 surface than the Ti/Al (P1, P2) samples. Moreover, blue spectrum in Figure 17 (Ti/Al (P2)) indicates the presence of a larger extent of bulk Ti-Al sulfate species (1176 cm^{-1} and 1200-1300 cm^{-1}) on this surface. It is apparent in Figure 17 that even after a high temperature treatment, the sulfate species are still strongly adsorbed on the surface, indicating the powerful poisoning effect of sulfates as well as the significantly higher stability of sulfates species with respect to nitrates.

3.1.3.3 Thermal stability of the adsorbed NO_x species on the SO_2 treated Ti/Al support materials

In order to have a better understanding of the influence of SO_2 + O_2 treatment on the thermal stability and the desorption properties of the NO_x species on γ-Al_2O_3, TiO_2 and TiAl (P1, P2) TPD experiments were preformed.

Figure 18 shows the NO_x desorption profiles from the poisoned and fresh γ-Al_2O_3 samples. For clarity, only the 30, 32 and 46 amu desorption channels are shown in Figure 18. For the fresh alumina surface, two major desorption features are observed [66]. The first NO_x desorption feature visible at 389 K is related to the desorption of monodentate nitrates or weakly bound N_2O_3 which desorbs in the form of NO_2 and NO+O_2. The second major desorption band has its maximum at 625 K and is associated with the desorption/decomposition of bridging and bidentate nitrates [87, 88] which yield a greater NO_2 desorption signal.

The SO_2-poisoning of the alumina surface has a noticeable influence on the NO_x desorption features. It is evident from Figure 18 that sulfur poisoning alters the

type of stored/adsorbed NO_x species. For the poisoned sample, the major feature around 380 K (associated with the monodentate nitrates or weakly bound N_2O_3 desorption) appears to a larger extent than the bidentate/bridged nitrate desorption at 675 K from the same (poisoned) surface. This finding is also consistent with the FTIR results obtained for NO_2 adsorption on the sulfated γ-Al_2O_3 surface (Figure 14), yielding an intense band corresponding to adsorbed NO^+/N_2O_3 species. Thus, SO_x species seem to compete with the nitrate species for surface sites and in the presence of SO_x species, nitrates are partially consumed and converted into weakly bound N_2O_3 (presumably via pathway 8 described in section 3.1.3.2) or NO^+ (pathway 7) which in turn suppresses the high-temperature nitrate desorption feature in the TPD experiments.

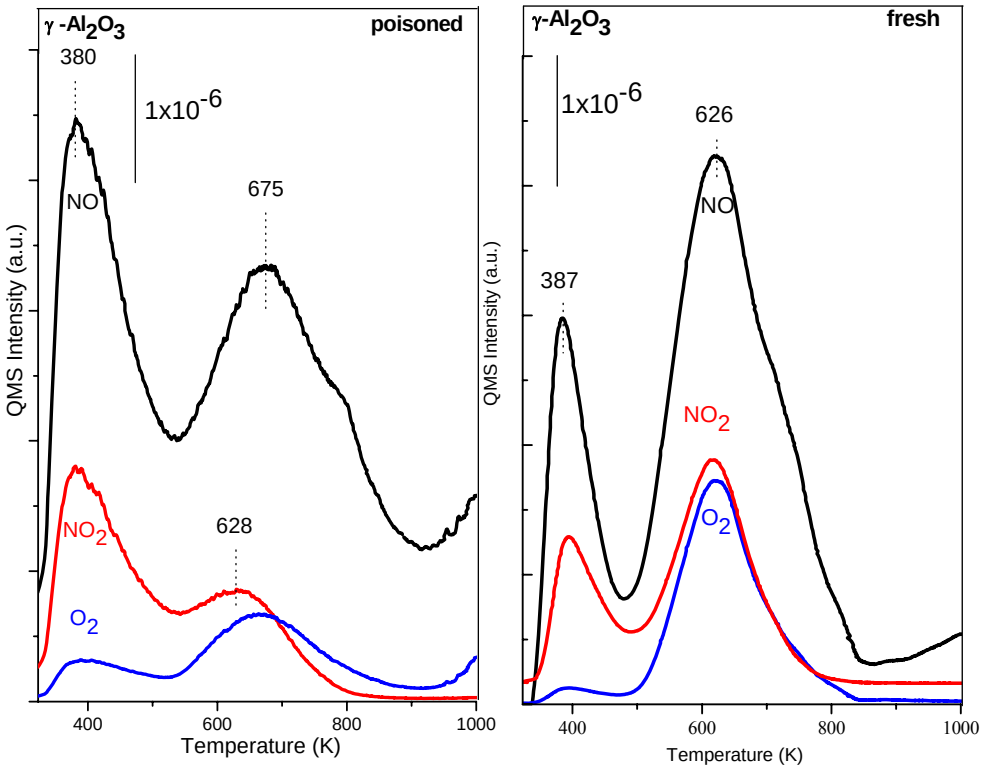

Figure 18. TPD profiles obtained from poisoned and fresh γ-Al_2O_3 samples which are saturated with 8 Torr NO_2 (g) at 323 K for 20 min. Black, blue and red curves correspond to 30 amu (NO), 32 amu (O_2) and 46 amu (NO_2) signals, respectively. (Before the NO_2 adsorption, sample was poisoned via SO_2 (g) + O_2 (g) exposure at 323 K, where SO_2:O_2 pressure ratio was 0.1 Torr :1 Torr, followed by further heating in the gaseous mixture at 473 K for 30 min and a final evacuation at 323 K).

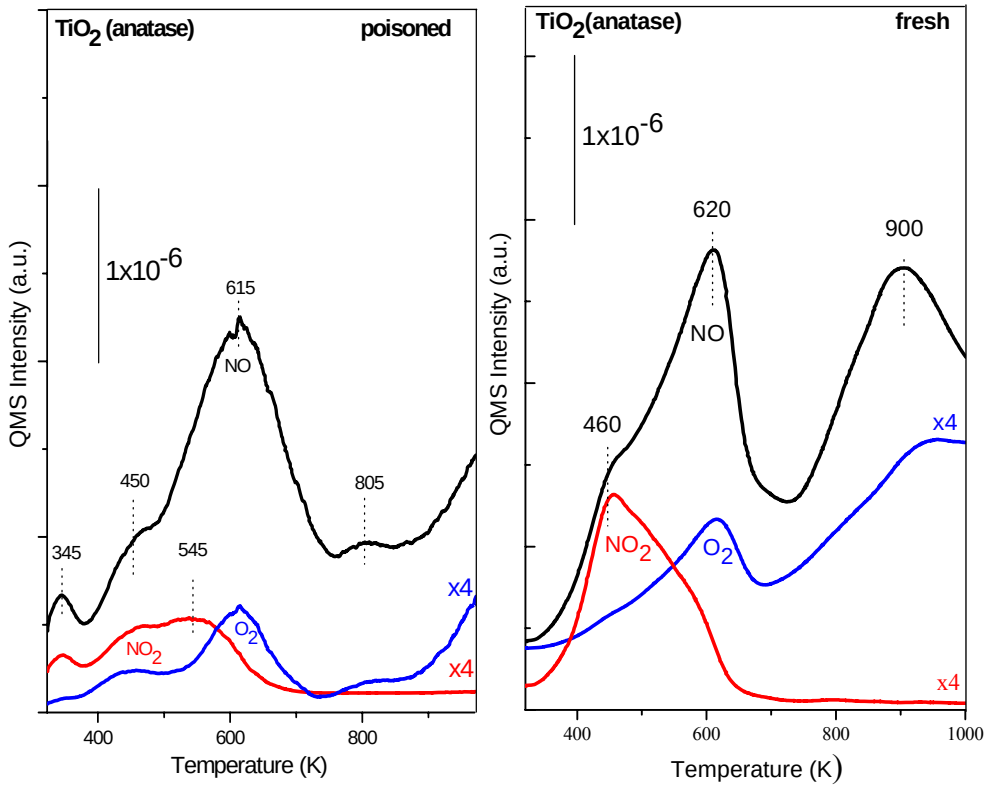

Figure 19. TPD profiles obtained from poisoned and fresh TiO_2 (anatase) samples which are saturated with 8 Torr NO_2 (g) at 323 K for 20 min. Black, blue and red curves correspond to 30 amu (NO), 32 amu (O_2) and 46 amu (NO_2) signals, respectively. (Before the NO_2 adsorption, sample was poisoned via SO_2 (g) + O_2 (g) exposure at 323 K, where SO_2:O_2 pressure ratio was 0.1 Torr :1 Torr, followed by further heating in the gaseous mixture at 473 K for 30 min and a final evacuation at 323 K).

Figure 19 shows the TPD profiles for NO_x desorption from the fresh and poisoned TiO_2 (anatase) reference sample. Briefly, the fresh TiO_2 sample presents a weak shoulder at 460 K mostly related with molecularly bound NO_2 species and/or partially monodentate nitrates and two broad features located at 620 K and 900 K. The bands at 620 and 900 K are attributed to the decomposition of the monodentate and bridged/bidentate nitrates. In a former study [93] the high temperature desorption feature (900 K) was attributed to nitro-nitrito obtained by transformation of chelate nitrates at ~650 K.

On the other hand, the poisoned TiO_2 sample shows an additional minor desorption feature at 345 K, related with the NO^+/N_2O_3 desorption (in the form of $NO + NO_2$). The later feature at 450 K is associated with monodentate nitrates and/or partially with weakly adsorbed molecular species. The main desorption band occurs at 615 K and this is suggested to be due to the monodentate nitrates from the surface. The most striking aspect of TPD profile of the poisoned anatase is that the nitrite/nitrate species are not formed. Thus the influence of the SO_x species on the NO_x desorption profiles of the anatase surface is rather similar to that of the alumina surface indicating similarities in the surface poisoning mechanisms

Figures 20 and 21 presents the NO_x desorption profiles of fresh and poisoned Ti/Al (P1) and Ti/Al (P2) surfaces, respectively. Considering the surface morphology of the fresh Ti/Al (P1) sample which is composed of mostly large TiO_2 domains, the feature at 780 K in Figure 20 can be associated with the nitrate decomposition from the isolated (bulk-like) TiO_2 clusters. Moreover, the shoulder at ~ 900 K is attributed to the NO_x desorption from the less-abundant TiO_2 domains with relatively smaller average crystallite sizes having a less-ordered structure and a higher surface defect density. The main effect of sulfur poisoning on the Ti/Al (P1) sample is the accentuation of the 370 K feature and the suppression of the high-temperature desorption signal at 870 K (Figure 20).

From the TPD profile of Ti/Al (P2) (Figure 21), it is visible that the desorption features at 375 K, 645 K, 745 K and 918 K are all suppressed upon sulphur poisoning. This observation suggests that SO_x species block some of the adsorption sites for the molecular NO_x species (e.g. NO^+/N_2O_3), nitrates on large TiO_2 crystallites (645 and 745 K) as well as nitrites/nitrates that are located on well-dispersed small TiO_2 domains (918 K).

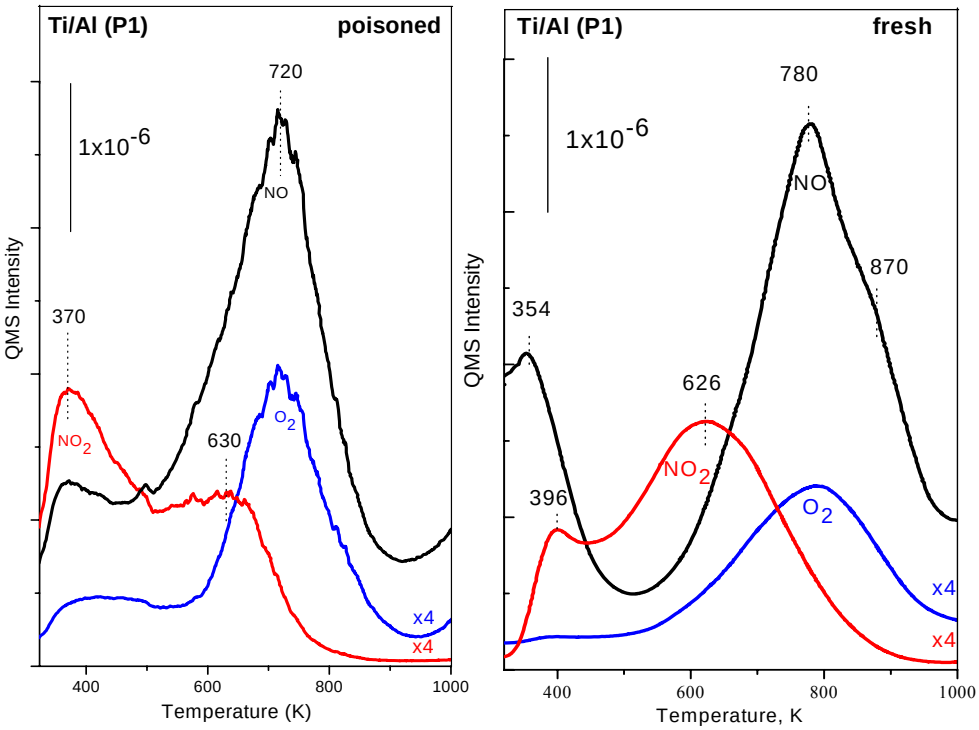

Figure 20. TPD profiles obtained from poisoned and fresh Ti/Al (P1) samples which are saturated with 8 Torr NO_2 (g) at 323 K for 20 min. Black, blue and red curves correspond to 30 amu (NO), 32 amu (O_2) and 46 amu (NO_2) signals, respectively. (Before the NO_2 adsorption, sample was poisoned via SO_2 (g) + O_2 (g) exposure at 323 K, where SO_2:O_2 pressure ratio was 0.1 Torr :1 Torr, followed by further heating in the gaseous mixture at 473 K for 30 min and a final evacuation at 323 K).

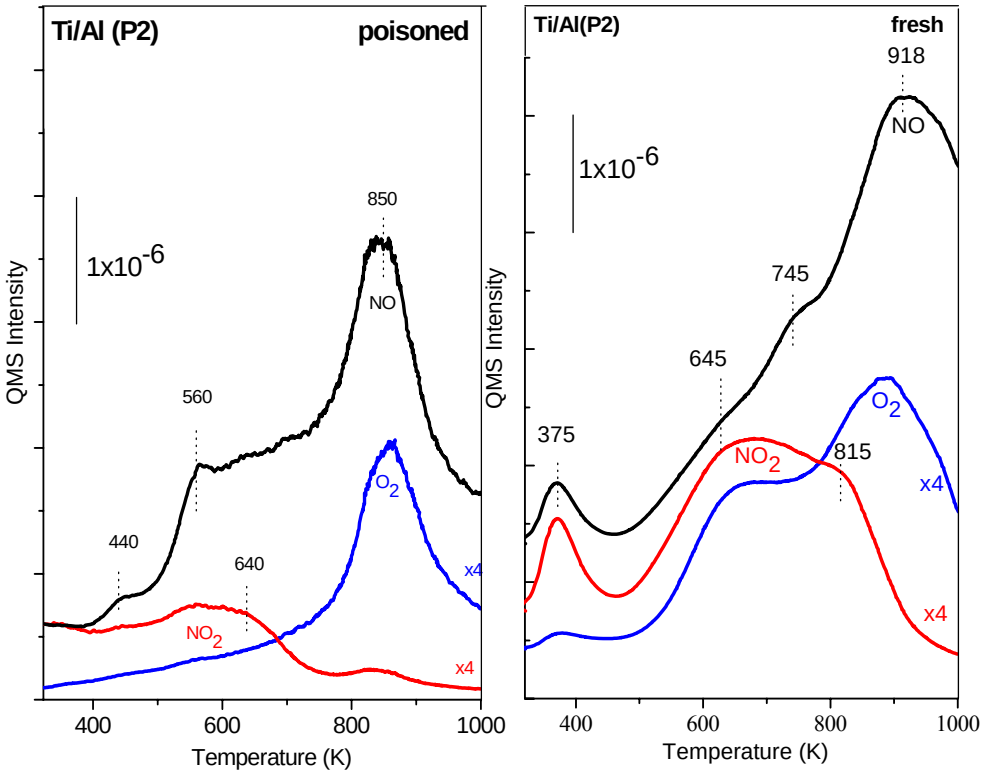

Figure 21. TPD profiles obtained from poisoned and fresh Ti/Al (P2) samples which are saturated with 8 Torr NO_2 (g) at 323 K for 20 min. Black, blue and red curves correspond to 30 amu (NO), 32 amu (O_2) and 46 amu (NO_2) signals, respectively. (Before the NO_2 adsorption, sample was poisoned via SO_2 (g) + O_2 (g) exposure at 323 K, where SO_2:O_2 pressure ratio was 0.1 Torr :1 Torr, followed by further heating in the gaseous mixture at 473 K for 30 min and a final evacuation at 323 K).

3.1.3.4 Thermal stability of the adsorbed SO_x species on the Ti/Al support materials

The desorption of sulfur containing species during the TPD experiments described in section 3.1.3.3. was also studied in detail. During these experiments, SO_2 (m/z = 64) and H_2S (m/z = 34) desorption signals were monitored after the saturation of a poisoned samples (i.e. γ-Al_2O_3, TiO_2, Ti/Al (P1) and Ti/Al (P2) with NO_2 at 323 K as seen in Figure 22. When the SO_x desorption profile of γ-Al_2O_3 is investigated two major signals are observed in the SO_2 desorption trace. One of these major signals is at 508 K (due to SO_3^{2-} and/or weakly bound molecular SO_2) [110] and the other major signal is at T > 1000 K (strongly bound surface and/or bulk sulfates). The presence of the latter (high -temperature feature is also in very good agreement with the FTIR results for this surface suggesting the existence of the sulfates on the surface even after thermal treatment at 1073 K (Figure 17 a).

On the other hand, the general characteristics of the SO_x desorption from the TiO_2 (anatase) surface is quite different and typically reveal less-strongly bound SO_x species that desorb at typically lower temperatures. SO_2 desorption occurs from the anatase predominantly at 452 K (due to SO_3^{2-} and/or weakly bound molecular SO_2) and at 760 K (due to moderately stable sulfates). Unlike γ-Al_2O_3, TiO_2 illustrates almost complete desorption below 800 K. This might be linked to the collapse/transformation of the anatase matrix into the rutile polymorph with the increasing temperature and a sharp decrease in the surface area which may trigger the decomposition of the surface SO_4^{2-}/TiO_2 units and their desorption. Furthermore it is worth mentioning that there exists a relatively well-defined characteristic H_2S desorption signal that is seen in the TPD profile of the poisoned anatase which reveals itself at 778 K.

SO_x desorption profiles of γ-Al_2O_3 and TiO_2 reference materials can be used as useful guidelines for the interpretation of the SO_x desorption from the Ti/Al (P1) and Ti/Al (P2) surfaces. When the corresponding SO_2 desorption profile of the poisoned Ti/Al (P1) surface is examined, it can be realized that the low-temperature desorption signal is comprised of two convoluted but distinguishable features at 480 K and 542 K. Comparison of this convoluted low-temperature band arising from the Ti/Al (P1) surface with the γ-Al_2O_3 and TiO_2 reference materials, indicates that the

480 K feature is most likely associated with the TiO_2 domains, while the 542 K feature is associated with the Al_2O_3 domains. Although this low temperature SO_2 desorption band possesses characteristics of both γ-Al_2O_3 and TiO_2 domains, the high temperature feature that appear at T > 1000 K is probably related to the sulfate desorption from the γ-Al_2O_3 domains only. These observations and the lack of a major desorption signal at 760 K (that is typical for anatase) point to the fact that, the general SO_2 desorption characteristics of the Ti/Al (P1) surface, resembles mostly to that of the γ-Al_2O_3 surface. On the other hand, when the SO_2 desorption profile of the Ti/Al (P1) surface is investigated, it is readily observed that the 64 amu signal is composed of desorption components at 480 K (associated with the Al_2O_3 domains), 580 K (associated with the TiO_2 domains) and a very pronounced shoulder at 760 K (associated with the TiO_2 domains). Furthermore, though minor, an H_2S desorption feature at 850 K is also discernible. All of these observations support the argument that Ti/Al (P2) surface has a Al_2O_3 - TiO_2 mixed oxide structure with well-dispersed titania domains.

Matsumoto et al. [9] suggested that the decomposition temperature of sulfates on TiO_2 support is lower than that of the Al_2O_3 support under reducing conditions. Hirata et al. [57] suggested that H_2S desorbs more easily if the interface between Al_2O_3 and TiO_2 increases, which can be done via a finer distribution of TiO_2 particles on alumina. Takeuchi [112] focused on the size issue: the smaller the size of the sulfate particles, the more easily they are removed from the catalyst under reducing conditions Thus it is likely that the large interface between the well-dispersed TiO_2 domains and the alumina domains may pull the SO_2 desorption temperature to lower values as observed in the case of Ti/Al (P2) given in Figure 22.

Therefore, the overall stabilities of the various adsorbed SO_x species tend to increase in the following order: TiO_2 (anatase) < Ti/Al (P2) < Ti/Al (P1) < γ-Al_2O_3.

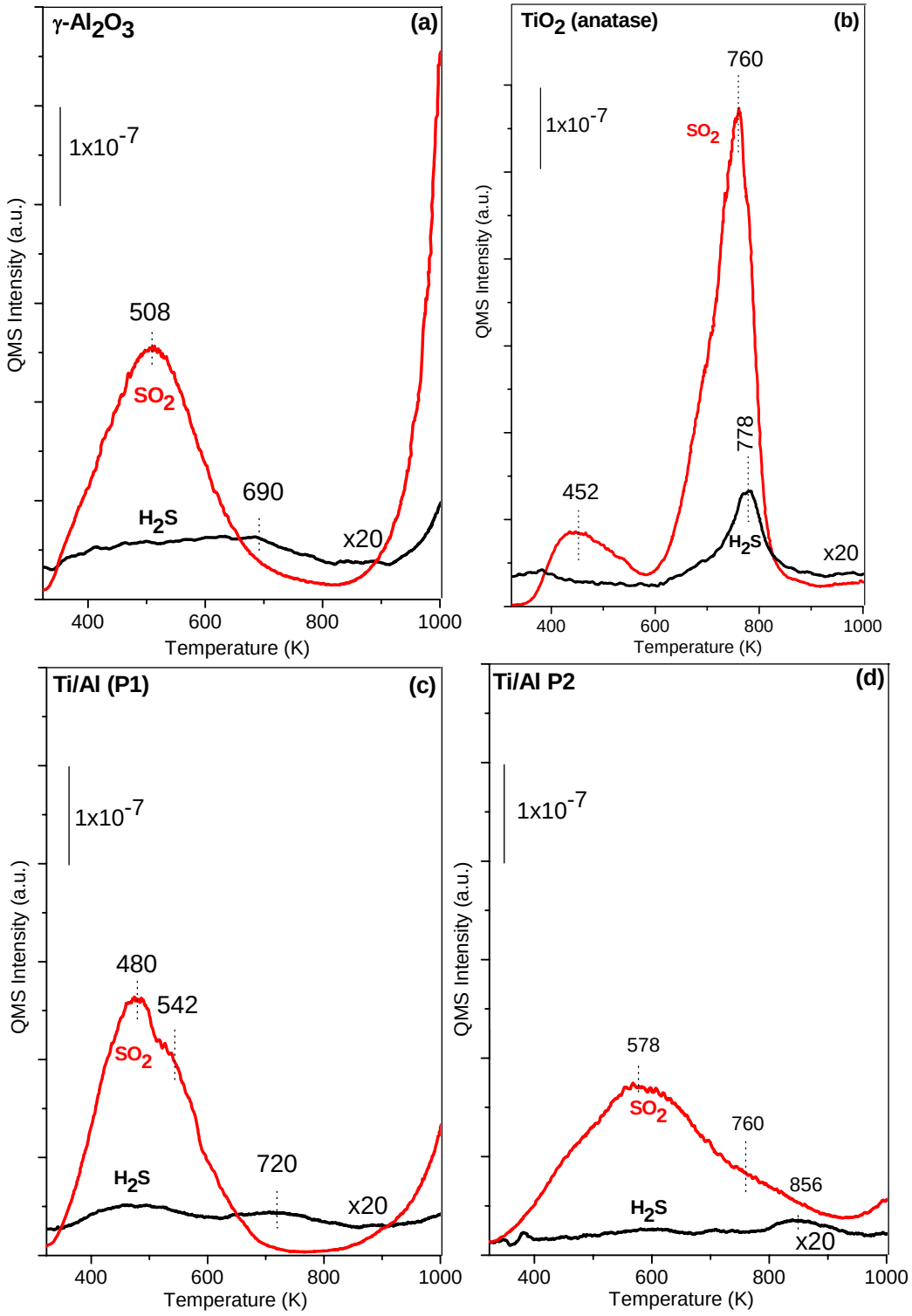

Figure 22. SO_2 and H_2S desorption profiles for **a)** γ-Al_2O_3 **b)** TiO_2 **c)** Ti/Al (P1) **d)** Ti/Al (P2) surfaces which are first poisoned with SO_2 (g) + O_2 (g) at 323 K (SO_2:O_2 pressure ratio = 0.1 Torr : 1 Torr) and then heated in this gas mixture at 473 K for 30 min followed by saturation with NO_2 at 323 K.

3.2 $BaO/TiO_2/Al_2O_3$ Ternary Oxide NO_x Storage Materials

3.2.1 Structural Characterization of the Thermally Treated Ba/Ti/Al NO_x Storage Materials: P1 vs. P2

3.2.1.1 XRD Experiments

Figures 23 and 24 show the XRD patterns of the uncalcined and calcined 8Ba/Ti/Al and 20Ba/Ti/Al samples prepared via P1. Typical diffraction peaks corresponding to γ-Al_2O_3 and crystalline $Ba(NO_3)_2$ (JCPDS 24-0053) were detected for both samples. The decomposition of Ba-nitrate diffraction signals was observed after calcination at 873K for both samples independent of the Ba-loading. As expected, $Ba(NO_3)_2$ species for the higher loaded 20Ba/Ti/Al sample are characterized with considerably higher crystallinity and stronger signals than that of the samples with the lower Ba content.

The thermal treatment at higher temperatures results in significant alterations in the crystallographic compositions of the Ba/Ti/Al samples with different Ba contents. XRD pattern of the 8Ba/Ti/Al sample calcined at 873 K given in Figure 21a shows broad diffraction features associated with the γ- Al_2O_3 and minor features related to anatase. On the other hand, 20Ba/Ti/Al sample reveals γ-Al_2O_3 features, coexisting with strong signals associated with the $BaTiO_3$ structure having a cubic *Pm*3*m* symmetry (JCPDS 74-1964) at 873 K. With increasing the temperature to 1273 K, this phase undergoes a further structural reconfiguration due to its interaction with the anatase and Al_2O_3 domains present in the system. This is also evident from the lowered intensities of the $BaTiO_3$ peaks at 1273 K and the formation of a new set of doublets separated by ~0.4°, assigned to the formation of $BaTi_2O_5$ and/or a new composite phase in the form of $Ba_xTi_yO_z$ or $Ba_xTi_yAl_zO_n$.

It is also visible in Figure 23 and 24 that after thermal treatments at 1073 and 1273 K, relatively sharp diffraction features attributed to the presence of anatase and a complex phase in the form of $Ba_{1.23}Al_{2.46}Ti_{5.54}O_{16}$ (JCPDS 033-0133) appear in the XRD patterns for both samples. Degree of crystallinity of this complex oxide increases with increasing the calcination temperature from 1073 to 1273 K.

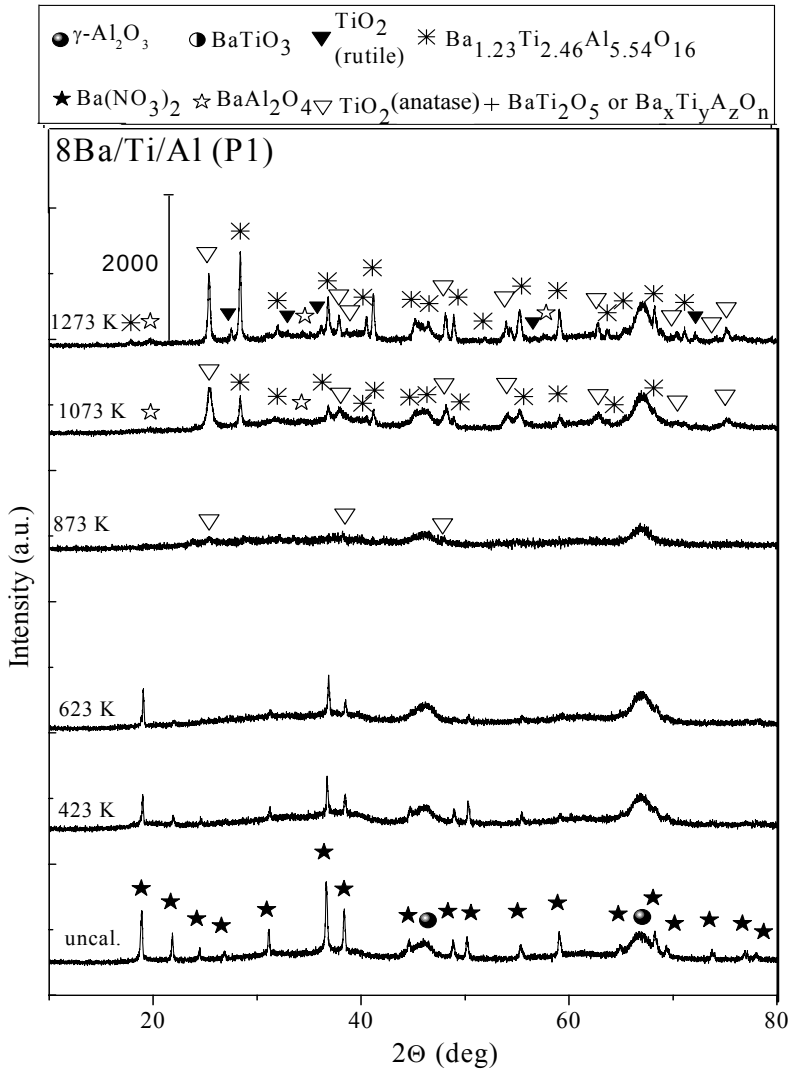

Figure 23. Thermal behavior of the XRD profiles corresponding to the as-prepared 8Ba/Ti/Al (P1) materials and the 8Ba/Ti/Al (P1) samples annealed at 423-1273 K in Ar(g).

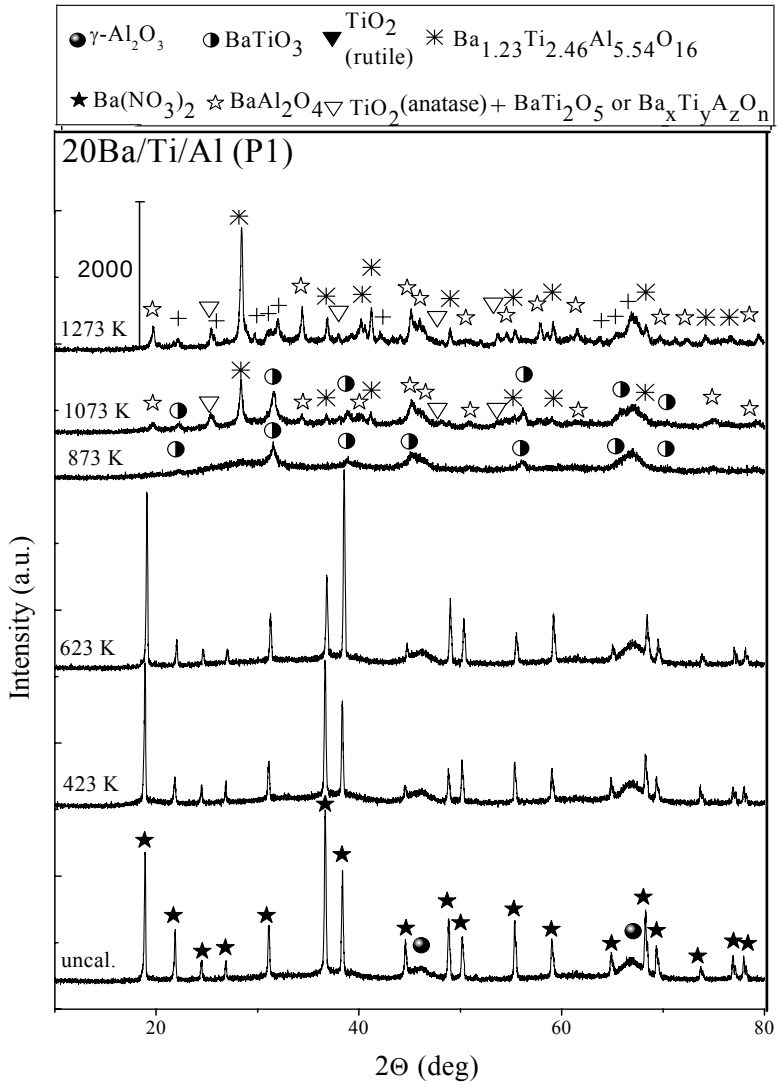

Figure 24. Thermal behavior of the XRD profiles corresponding to the as-prepared 20Ba/Ti/Al (P1) materials and the 20Ba/Ti/Al (P1) samples annealed at 423-1273 K in Ar(g).

In Figure 24 it is visible that within 1073-1273 K, the anatase-related diffraction features originating from the 20Ba/Ti/Al sample show considerably lower intensities in comparison with those observed for the 8Ba/Ti/Al sample. In addition to these observations, rather weak and broad features are also detected. These minor features are assigned to the presence of $BaAl_2O_4$ (JCPDS 17-0306). $BaAl_2O_4$ signals are characterized with considerably higher intensities for the 20Ba/Ti/Al sample. Figure 24 shows that at 1273K there is a phase transformation from anatase to rutile. However, rutile formation is not observed for the 20Ba/Ti/Al sample at the same temperature.

Comparing the temperature-dependent XRD profiles of the Ti/Al (Figure 3) and Ba/Ti/Al systems (Figures 23 and 24) at 1273 K reveals that anatase to rutile polymorphic phase transformation is suppressed in the presence of Ba, particularly for higher Ba loadings. This can be related with the strong interaction between the Ba and Ti domains and solid-state reactions leading to a structural reconfiguration and formation of a solid solution between these components. A similar interaction where the formation of a solid solution in the form of $Ba(Ti_{1-2x}Al_{2x})O_{3-x}$ was also reported in a former study [113] where the inhibition of the grain growth in $BaTiO_3$ by addition of Al_2O_3 was investigated.

The XRD patterns of the Ba/Ti/Al samples with different Ba loadings (8 and 20 wt. % BaO) prepared via P2 are presented in Figures 25 and 26. The XRD profiles corresponding to the as-prepared and annealed 8(20)Ba/Ti/Al (P2) samples within 423 to 623 K reveal very broad diffraction features that are assigned to γ-Al_2O_3 (JCPDS 29-0063) and additional intense peaks due to the crystalline $Ba(NO_3)_2$ (JCPDS 24-0053). In addition, the 20Ba/Ti/Al (P2) sample is characterized with considerably higher $Ba(NO_3)_2$ crystallinity than that of the 20Ba/Ti/Al (P1) sample [1] which is also consistent with the relatively higher thermal stability of the $Ba(NO_3)_2$-related peaks for the 20Ba/Ti/Al (P2) sample which can exist on the surface even after annealing at 873 K seen in Figure 26.

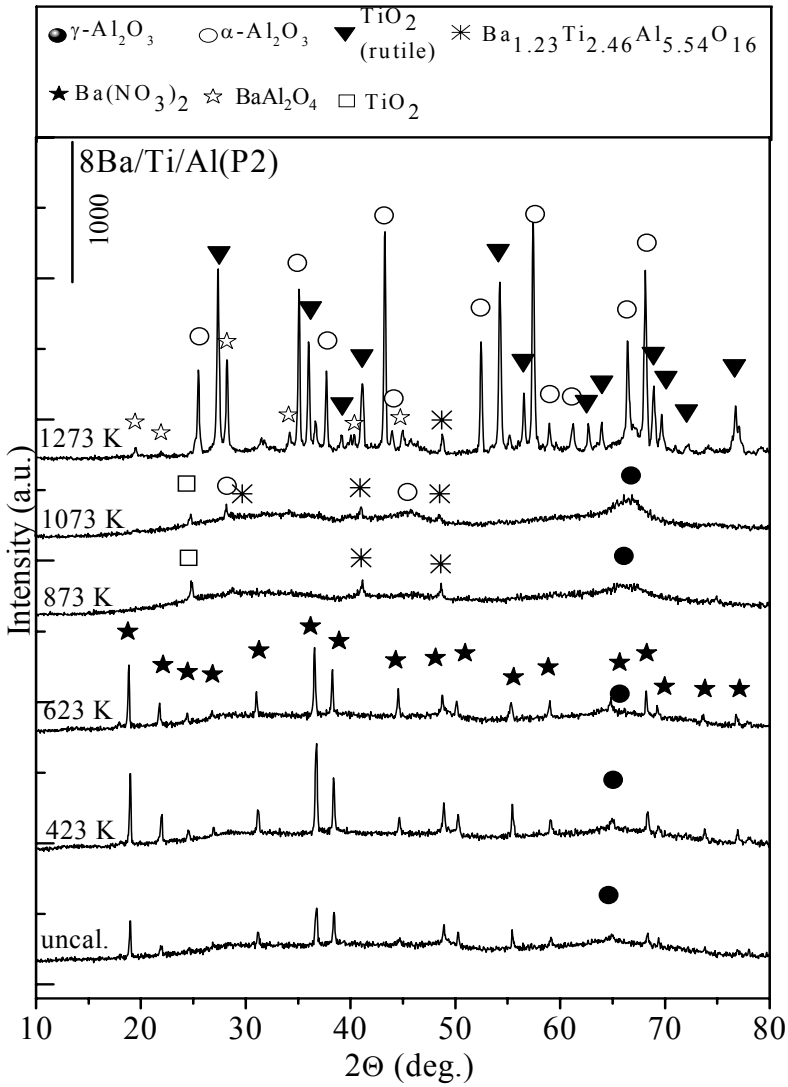

Figure 25. Thermal behavior of the XRD profiles corresponding to the as-prepared 8Ba/Ti/Al (P2) materials and the 8Ba/Ti/Al (P2) samples annealed at 423-1273 K in Ar(g).

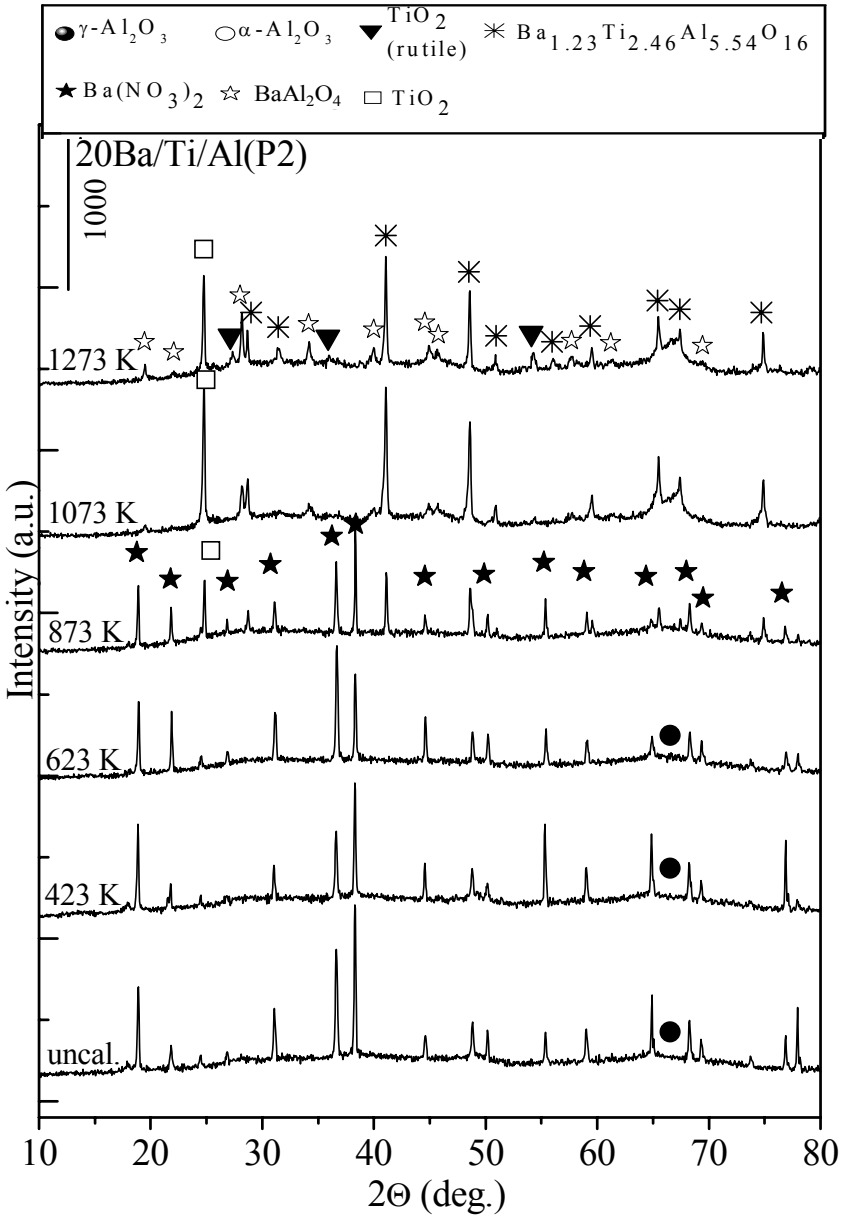

Figure 26. Thermal behavior of the XRD profiles corresponding to the as-prepared 20Ba/Ti/Al (P2) materials and the 20Ba/Ti/Al (P2) samples annealed at 423-1273 K in Ar(g).

A new set of reflection signals in the form of $Ba_{1.23}Al_{2.46}Ti_{5.54}O_{16}$ (JCPDS 33-0133) appear in the XRD patterns for the 8(20)Ba/Ti/Al (P2) samples after thermal treatment at 873 K. This complex phase appears to be more (with sharper and more intense XRD reflections) for the higher Ba loaded sample (Figure 26). In addition to these features, minor diffraction peaks corresponding to $BaAl_2O_4$ (JCPDS 17-0306) are also detected at temperatures above 873 K for the 8(20)BaTi/Al (P2) samples. The degree of crystallinity of the $Ba_{1.23}Al_{2.46}Ti_{5.54}O_{16}$ phase increases with increasing the temperature from 873 to 1073 K for the 20BaTi/Al (P2) sample, and the reverse (decreasing of the phase) is observed for 8BaTi/Al (P2) sample (Figure 25), where this complex disappears at 1273 K.

XRD profile corresponding to the 8BaTi/Al (P2) sample at 1273 is dominated by the strong reflections due to the formation of α-Al_2O_3 (JCPDS 10-0173) and rutile (JCPDS 04-0551) with a slight contribution from $BaAl_2O_4$. It should be mentioned that such γ to α-alumina phase transformation in the XRD profile of the 20BaTi/Al (P2) sample at 1273 K was not detected. It is visible in Figure 26 that the XRD pattern of the 20BaTi/Al (P2) sample at 1273 K is dominated by the $Ba_{1.23}Al_{2.46}Ti_{5.54}O_{16}$, $BaAl_2O_4$ and minor contributions from the rutile phase. Besides, an additional feature also exists in Figures 25 and 26 that is tentatively assigned to a TiO_2 phase (JCPDS 35-088), which is not visible for P1.

These results, which are also consistent with the current Raman spectroscopic results given in the next section, indicate a stronger interaction between the BaO and TiO_2 components for the 20BaTi/Al (P2) system which also hinders the phase transformation of anatase to rutile. This observation is also in very good agreement with the significantly greater reduction in the surface area of the 8Ba/Ti/Al (P2) sample at 1273 K than that of the 20Ba/Ti/Al (P2) sample (Table 3).

3.2.1.2 Raman Spectroscopy Experiments

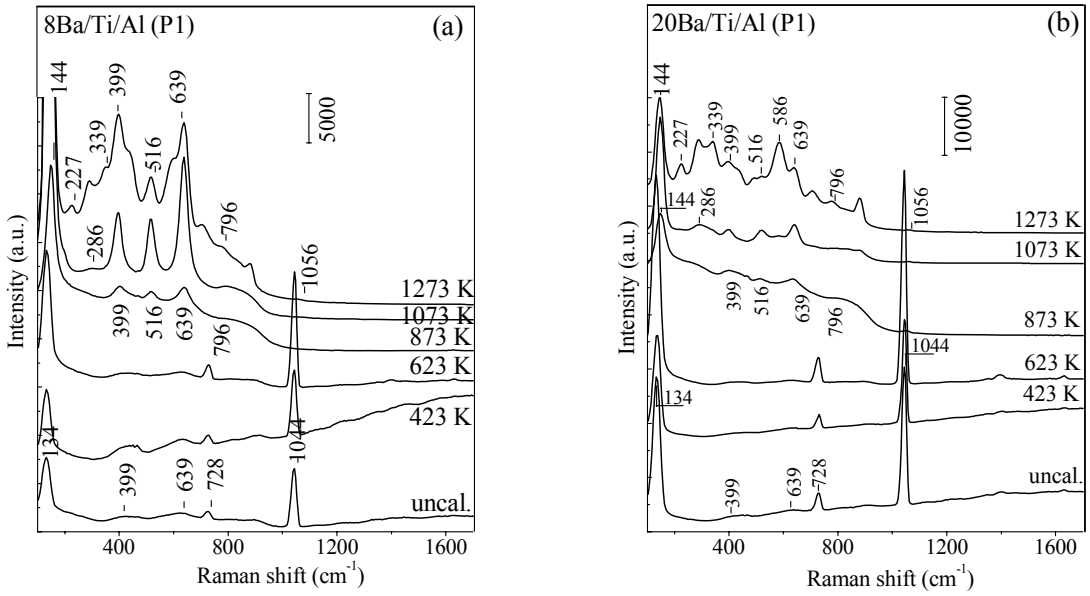

Figure 27. Temperature-dependent ex-situ Raman spectra corresponding to the calcined (423-1273 K) and uncalcined Ba/Ti/Al (P1) samples with different Ba loadings: (a) 8Ba/Ti/Al and (b) 20Ba/Ti/Al.

Figure 27a and 27b displays the temperature-dependent ex-situ Raman spectra corresponding to the uncalcined, calcined (423-1273 K) 8Ba/Ti/Al (P1) and 20Ba/Ti/Al (P1) samples. On the basis of previous studies, [66, 114-116] it is clear that Raman spectra corresponding to T ≤ 673K consist of Raman bands that can readily be assigned to crystalline $Ba(NO_3)_2$, consistent with the XRD patterns given in Figure 23. The most dominant band at 1044 cm^{-1} is attributed to the symmetric stretching mode of the nitrate (NO_3^-) ion, the band with medium intensity at 728 cm^{-1} is due to the nitrate bending mode, and the group of weak bands at 1634, 1357, and 1406 cm^{-1} are assigned to the longitudinal optical (LO) and transverse optical (TO) modes of the antisymmetric stretching. The observed lattice phonon band at 134 cm^{-1} shows high degree of crystallinity of the $Ba(NO_3)_2$ domains [66, 114]. In addition, there are bands which are weakly expressed around 399, 639 cm^{-1} and a broad shoulder in the spectral range of 800-900 cm^{-1}. These broad minor features are related to anatase similar to the reference spectrum in inset (i) of Figure 3. It should also be noted that these features are very small in terms of their crystalline sizes or they may exist in an amorphous form and thus are elusive to detect via XRD.

After increasing the calcination temperature to 873 K in Figure 27, all of the nitrate-related Raman bands completely disappear. This is particularly evident by monitoring the weakening of the $Ba(NO_3)_2$ lattice phonon band (134 cm^{-1}) and the symmetric nitrate stretching mode (1044 cm^{-1}) where they completely vanish at 873K. At this temperature, both samples are characterized by relatively weak features at 399, 516, and 639 cm^{-1}, a shoulder at 796 cm^{-1} and a relatively stronger band at 144 cm^{-1} which can all be assigned to anatase, consistent with the XRD data. The $Ba(NO_3)_2$ decomposition to BaO may also facilitate the formation of complex Ba-Ti mixed oxides such as $BaTiO_3$ or $Ba_{1.23}Al_{2.46}Ti_{5.54}O_{16}$.

The first-order Raman scattering is symmetry forbidden for crystalline BaO [114, 117] however, the defect-rich BaO structure is characterized by a broad set of weak bands within the spectral region of 350-500 cm^{-1} [66, 114] Therefore, in Figure 27a and 27b, Raman spectra corresponding to T > 623 K may contain the weak BaO signal that is likely to be convoluted with the stronger anatase features appearing around 350-500 cm^{-1}. At higher temperature treatments, the Ba/Ti/Al (P1) samples lead to noticeable spectral Raman changes. It is visible in Figure 27a that at 1073 K, 8Ba/Ti/Al (P1) sample is characterized by more intense anatase bands when

compared to the 20Ba/Ti/Al (P1) system, this was also evident from the XRD results presented in Figure 22a. Figure 23b shows that at 1073 K the Raman spectrum corresponding to the 20Ba/Ti/Al (P1) sample contains additional Raman bands at 286, 586, 709, and 879 cm^{-1} which is unlike anatase. The intensities of these additional features increase with increasing calcination temperature and dominate the surface. These bands are also detected for the 8 wt % BaO loaded Ti/Al sample, however for the latter case, anatase related bands exists the surface instead of the additional Raman features. Interpretation of the crystallographic changes in the light of the vibrational structure suggests that the additional features can be due to the complex $Ba_{1.23}Al_{2.46}Ti_{5.54}O_{16}$ phase.

The presence of TiO_2 mainly in the form of anatase results in a decrease in the thermal stability of the nitrate species formed on the Ba/Ti/Al surface, when compared with previous studies lacking the promoter titania [89, 118, 119]. This result indicates that the presence of TiO_2 domains actively influences the nitrate decomposition temperature by modifying the interaction between the NO_x storage units and its underlying support material. In the Ba/Ti/Al ternary systems, it is apparent that the TiO_2 domains show a high affinity toward Ba domains. Thus, it can be believed that the Ba units prefer to anchor predominantly on the TiO_2 islands. This argument is also supported via SEM/EDX results presented below. Such a preferential interaction between Ti- and Ba-containing domains may influence the surface dispersion and morphology therefore the mobility of the BaO domains.

The samples prepared via P2 (i.e. 8(20)BaTi/Al (P2)) also present a strong interaction between the BaO and TiO_2 components for the 20BaTi/Al (P2) system which also hinders the phase transformation of anatase into rutile (data not shown). This observation is in very good agreement with the significantly higher reduction in the surface area of the 8Ba/Ti/Al (P2) sample at 1273 K with respect to that of the 20Ba/Ti/Al (P2) system (Table 3).

3.2.1.3 SEM-EDX Measurements

EDX elemental mapping also yields valuable qualitative information regarding the morphologies of different surface oxide domains. Figure 28a-28d illustrate SEM/EDX images that belong to the same 8Ba/Ti/Al (P1) sample surface that was initially thermally treated at 623 K.

Figure 28b demonstrates that the EDX images corresponding to Ba (shown in red) and Al (shown in green) maps, reveal an inhomogeneous surface distribution for Ba and Al-containing domains. A similar trend is also observed for the combination of Ti and Al on the EDX signals (Figure 28c). On the other hand, Figure 28d shows that the EDX maps for Ba and Ti domains (represented in red and green, respectively) yield a yellow color indicating the presence of a combination signal originating from the spatial overlap of Ba and Ti signals. Considering the spatial resolution of the EDX signals being in the order of a few micrometers, the observation of the predominant yellow signal suggests that Ti and Ba elements form spatially overlapping domains (e.g. $Ba(NO_3)_2/TiO_2$, BaO/TiO_2, and/or $Ba_xTi_yO_z$ etc.) in the submicrometer scale. This observation is in perfect agreement with the current Raman and XRD data, indicating a high affinity of Ti domains towards Ba-containing surface species. This high affinity of Ti domains toward Ba-containing species is present in both 8Ba/Ti/Al and 20Ba/Ti/Al systems at a variety of temperatures within 423-1073 K (data not shown).

All of the observations given above indicate that TiO_2 sites present strong anchoring sites for the NO_x storage component in the Ba/Ti/Al system. Therefore, these units modify the stability of the stored nitrates by altering the interfacial interaction between the Ba-containing sites and the underlying support surface.These observations also reveal facile solid-state reactions between Ti and Ba domains at higher temperatures on the Ba/Ti/Al system.

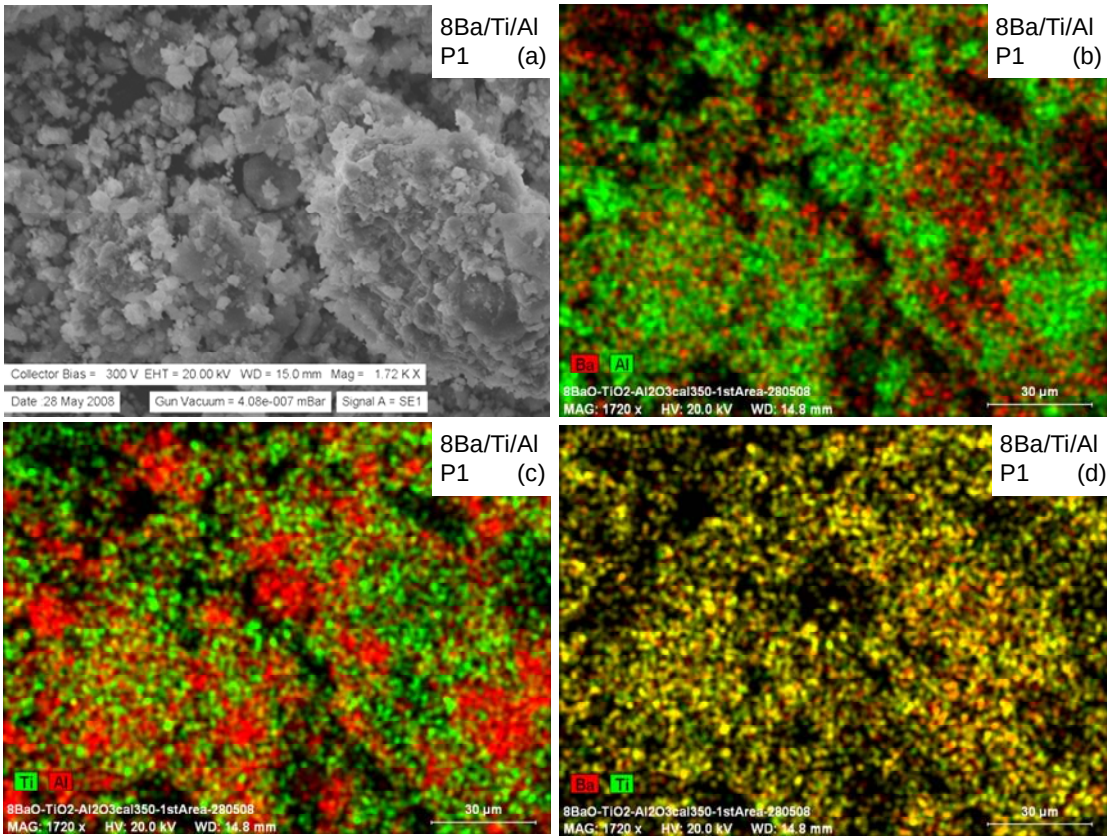

Figure 28. Selected SEM/EDX images for 8 Ba/Ti/Al (P1) samples calcined at 623K. (a) SEM image, images given in b-d correspond to the elemental EDX mapping (b) Ba + Al, (c) Ti + Al, (d) Ba + Ti .

3.2.1.4 Surface Acidity: FTIR Spectra of Chemisorbed Pyridine

The temperature-dependent FTIR spectra for chemisorbed pyridine on the surfaces of the simple 8(20)Ba/Al NO_x storage materials are given in Figures 29a and 29b, respectively. In a similar fashion, Figures 30a and 30b show the IR data corresponding to the Ti-containing samples with two different BaO loadings (i.e. 8(20)Ba/Ti/Al (P1)).

Pyridine adsorptions on the surface of all of the Ba-containing samples reveal characteristic features similar to that of the support materials. Namely, the IR bands in the 1640 - 1565 cm^{-1} (υ_{8a}, υ_{8b}) spectral region suggest the coordination of pyridine on the Al^{3+} Lewis acid sites, while the band at 1593 cm^{-1} indicates the presence of weakly interacting pyridine that is bound to the surface through hydrogen bonding. It should be noted that the feature corresponding to the presence of Ti^{4+} Lewis acid sites (1605 cm^{-1}) is also observed in the case of the Ti-containing Ba/Al samples (Figure 30a and 30b).

The presence of Ba-containing domains clearly has a drastic influence on the Lewis acidity. This is particularly noticed by a significant reduction in the intensities of the IR signals originating from the Lewis acid sites in Figures 29 and 30, in comparison with the IR signals observed in Figure 8. This observation indicates that more basic Ba-containing domains strongly interact with the acidic titania and alumina [120] domains and therefore cover these acidic sites. This results in blocking of the number of medium/strong Lewis acid sites on the binary Ba/Al and ternary Ba/Ti/Al oxide systems. These findings are in good agreement with the formation of complex Ba-Ti and Ba-Ti-Al structures identified in the current XRD, Raman, and EDX measurements.

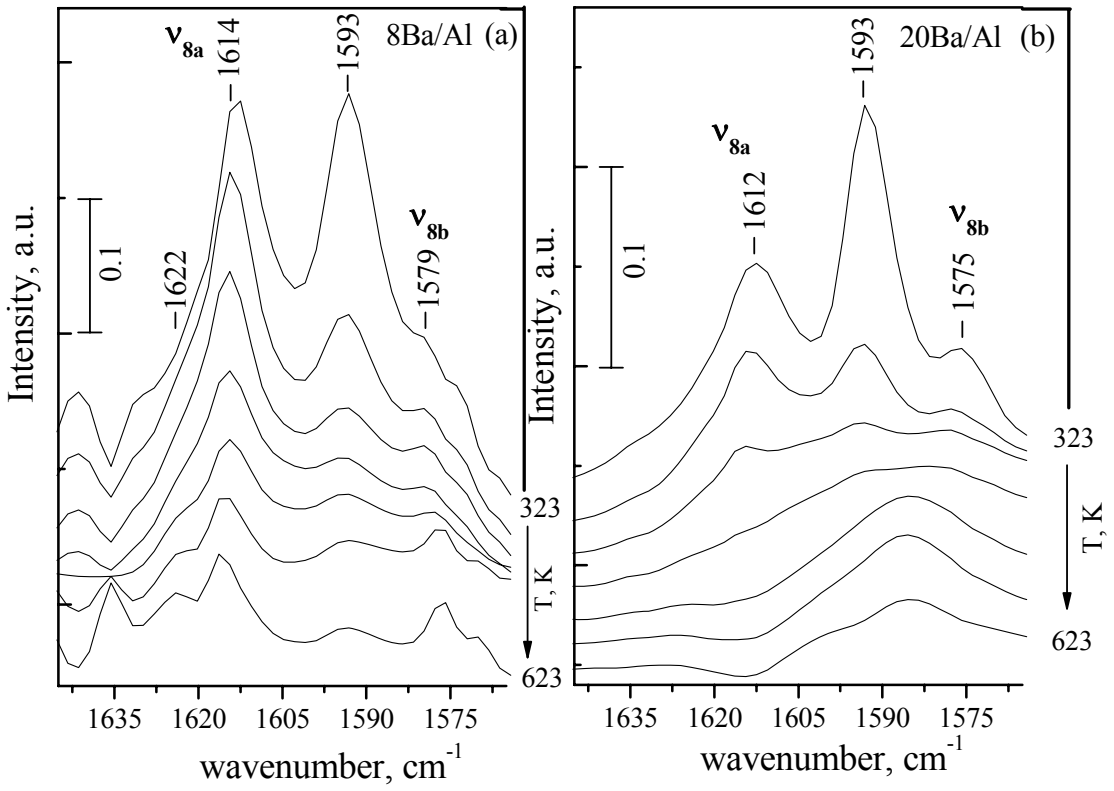

Figure 29. Temperature-dependent (323-723 K) FTIR spectra for chemisorbed pyridine species formed at room temperature on the surface of the Ba/Al NO*x* storage materials with different BaO loadings precalcined at 873 K: (a) 8Ba/Al and (b) 20Ba/Al. All spectra were acquired in vacuum at 323 K after the pyridine exposure, followed by the evacuation at 323 K, annealing to the given temperature and then cooling to 323 K in vacuum

In addition to the number of Lewis acid sites, Ba-containing domains also significantly modify the strength of the surface acid sites, which is readily visible by considering the lower thermal stability of pyridine on the Ba/Ti/Al samples (Figures 29 and 30). This is also illustrated in Figure 29b, where a higher Ba loading suppresses the υ_{8a} band (1622 and 1612 cm^{-1}) at relatively low temperatures (423 K). On the other hand, the band at 1593 cm^{-1} which is due to the weakly interacting hydrogen-bonded pyridine, is observed to interact strongly with the Ba domains. This suggests that the electronic environment of the Al^{3+} Lewis acid sites is profoundly altered by the Ba domains.

The combination of these results clearly illustrate that the existence of basic BaO or $Ba(NO_3)_2$ on the surface of the pure γ-Al_2O_3 and Ti/Al sample leads to a considerable decrease in surface Lewis acidity. Furthermore, the number of remaining coordinatively unsaturated Al^{3+} and Ti^{4+} Lewis acid sites that are exposed on the surface strongly depends on the Ba loading and its distribution on the surface of the NO_x storage systems. The IR experiments conducted with pyridine adsorption on the Ba/Al systems show that increasing the Ba loading on the surface blocks the available alumina sites. Thus, this results in a lower surface acidity where pyridine prefers to bind on Ba domains (1593 cm^{-1} band) through a hydrogen-bonding interaction. On the other hand, comparison of Figures 29 and 30 imply that such a suppressive influence associated with the Ba domains on the strong/medium-strength alumina Lewis acid sites is less pronounced in the case of the Ba/Ti/Al system (Figure 26). This again proves that Ba domains prefer to interact strongly with the Ti domains rather than the alumina domains, resulting in a less pronounced suppression of the alumina-related Lewis acid sites.

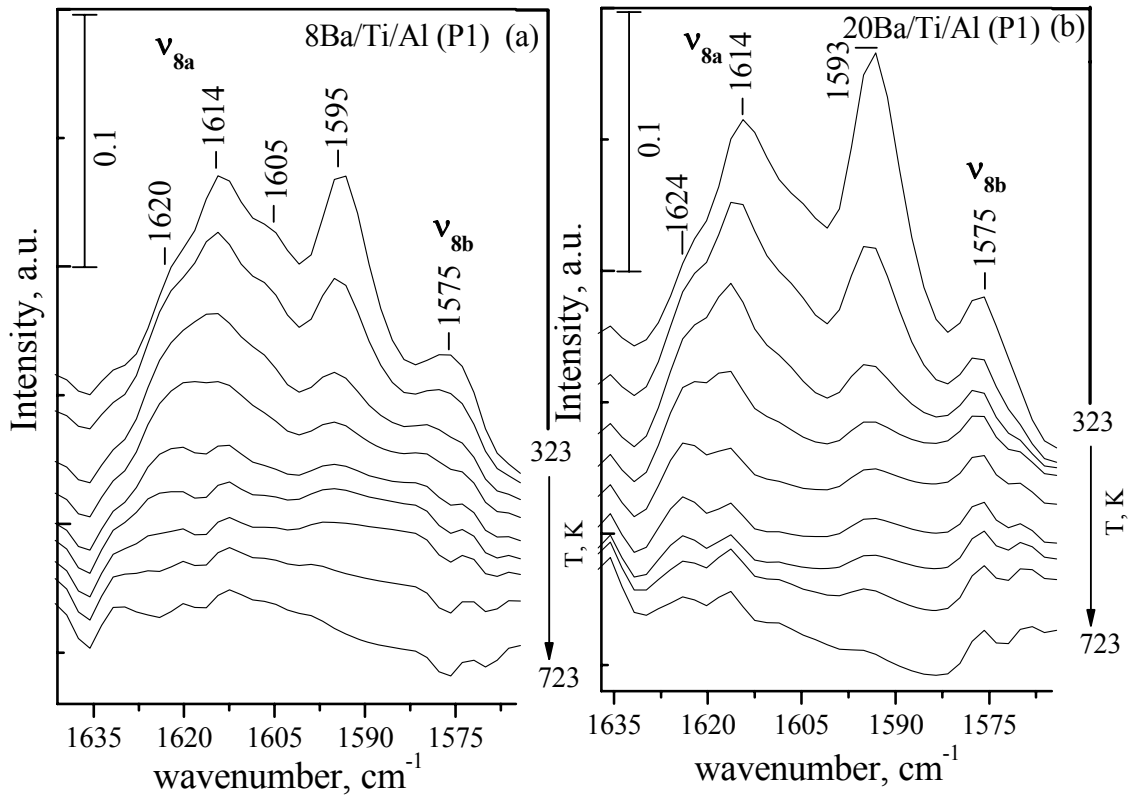

Figure 30. Temperature-dependent (323-723 K) FTIR spectra for chemisorbed pyridine species formed at room temperature on the surface of the Ba/Ti/Al (P1) ternary oxide NO*x* storage materials with different BaO loadings precalcined at 873 K: (a) 8Ba/Ti/Al and (b) 20Ba/Ti/Al. All spectra were acquired in vacuum at 323 K after the pyridine exposure, followed by the evacuation at 323 K, annealing to the given temperature and then cooling to 323 K in vacuum.

Current Raman and XRD data indicate that the 8Ba/Ti/Al (P1) sample calcined at 873 K predominantly consists of free anatase domains, where as the 20Ba/Ti/Al system shows a strong interaction between Ba and Ti domains that lead to the formation of $BaTiO_3$. It is clearly visible that there is a suppression of the IR intensity of the Ti^{4+}-related Lewis acid sites (1605 cm^{-1}) in Figure 30b with respect to the similar feature in Figure 30a, indicating a relative loss of Ti^{4+} Lewis acid sites which are coordinating to and/or covered with more Ba domains. Along these lines, it can be stated that Ba domains which prefer to anchor mainly on the Ti domains leave a larger fraction of free Al^{3+} sites exposed to pyridine adsorption, in comparison with the Ba/Al system (Figure 29). Such dissimilarities in the Ba surface distribution in the Ba/Al and Ba/Ti/Al systems results in a higher surface acidity for the Ba/Ti/Al system.

3.2.2 NO_x Uptake Protocol: Functionality/Performance of the $BaO/TiO_2/Al_2O_3$ NO_x Storage Materials

3.2.2.1 NO_x adsorption on Ba/Ti/Al systems via FTIR Spectroscopy

Figures 31 and 32 present the series of IR spectra for NO_2 (g) adsorption on the 8(20)Ba/Ti/Al (P1/P2) samples at 323 K.

Nature of the NO_x species formed on the surface of the $BaO/\gamma\text{-}Al_2O_3$ binary oxide system as a function of the Ba loading has been studied extensively in the literature via FTIR spectroscopy in a number of former reports [66, 89, 90, 120-122].

The very initial NO_2(g) uptake of the 8Ba/Ti/Al(P1) material (the bottommost spectrum given in Figure 31a) results in the formation of predominantly nitrite features located at 1225 cm^{-1} (most likely coordinated to Ba^{2+} sites) with a shoulder at about 1185 cm^{-1} (most likely coordinated to Ti^{4+} sites) [94, 123]. Further NO_2 (g) exposure leads to the oxidation of the surface nitrite species into various nitrate species. The intensities of these species increase with increasing surface NO_x coverage. There is evidence in the literature [121, 122] for the presence of two different types of nitrate species, the first being the surface (bidentate) nitrates that are associated with a BaO monolayer (or oligomers) on the alumina support surface and the second bulk-like $Ba(NO_3)_2$ species that grows on the BaO clusters. It was found in these studies that the characteristic features related to the presence of surface (bidentate) nitrates on the BaO sites appear at 1585 cm^{-1}, 1565 and ~1300 cm^{-1} while bulk Ba-nitrates yield bands that are located at 1320, 1442, 1483 cm^{-1}. In addition, it was also reported that the FTIR intensity ratio of the surface to bulk nitrate species is a function of the BaO loading [121, 122].

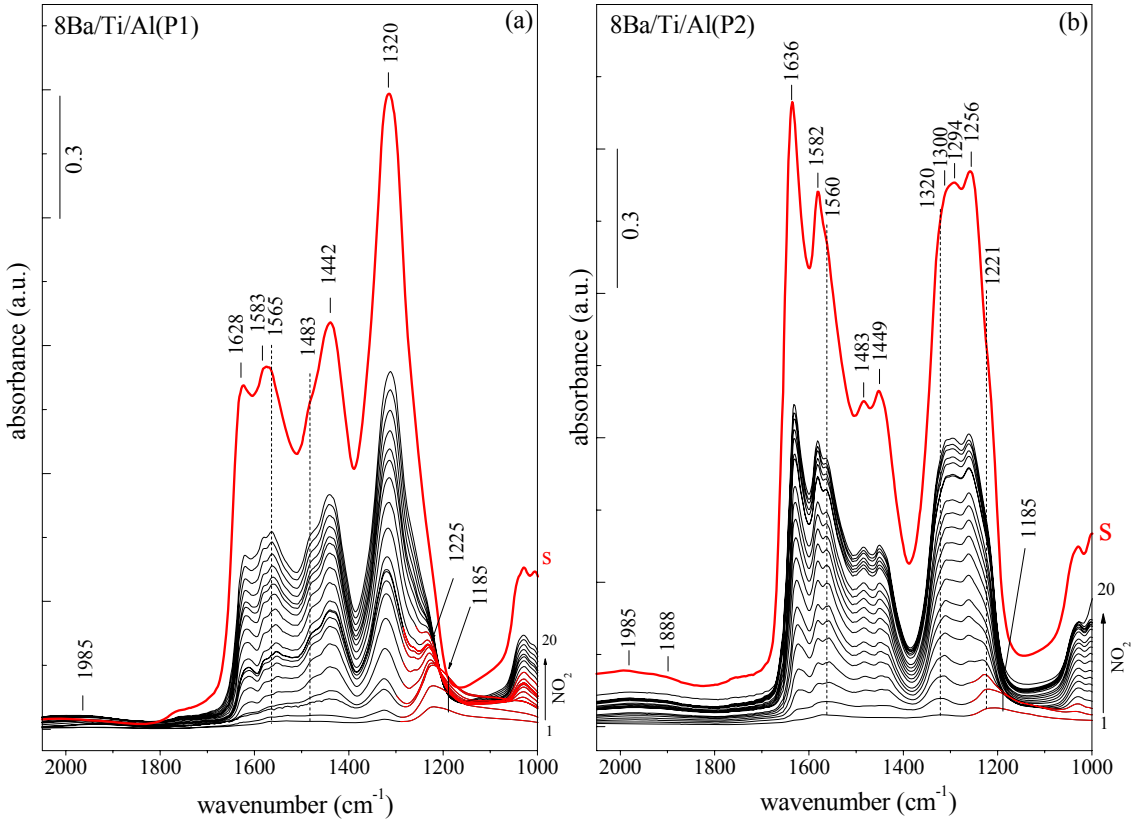

Figure 31. FTIR spectra corresponding to the stepwise NO_2 adsorption at 323 K on: (a) 8Ba/TiAl (P1) and (b) 8BaA/Ti/Al (P2) samples. The spectra corresponding to the fully saturated sample surfaces are marked with "S". (All spectra are acquired in vacuum at 323 K)

In Figure 31a the fully saturated sample surface is characterized by adsorption bands located at 1320, 1442 and 1483 cm^{-1} adsorbed on bulk (ionic) Ba-nitrates and additional nitrates at 1583 and 1628 cm^{-1} on TiO_2 domains with bidentate/bridged configurations. A comparative analysis of the IR spectra indicates that the nitrate-related features associated with the Ti^{4+} adsorption sites on the 8Ba/Ti/Al (P1) sample are significantly suppressed in comparison with that of the Ti/Al (P1) support material (Figure 9a). Furthermore, nitrate species bound to alumina sites are hardly seen on the 8Ba/Ti/Al (P1) sample indicating a smaller number of exposed alumina adsorption sites available. This observation is also in good agreement with the presence of only a very minor feature at ~ 1985 cm^{-1} related to the weakly adsorbed N_2O_3 or NO^+ on the exposed alumina sites.

Figure 31a shows that the intensities of the bands due to the formation of bulk Ba-nitrates are much more pronounced for the 8Ba/Ti/Al (P1) system. The IR signals related to the surface (bidentate) Ba-nitrates are significantly suppressed and are overlapping with the nitrate signals associated with the titania domains. These observations imply that BaO sites on the 8Ba/Ti/Al (P1) system exist mostly in the form of large BaO clusters and a relatively smaller amount of well-dispersed $(BaO)_x$ units exists in the form of "surface" Ba-nitrates. Therefore, the agglomerated BaO clusters partially cover and block the accessible Ti^{4+} and Al^{3+} surface sites for NO_x adsorption which is evident by the significant decrease of the signals due to the nitrates on the TiO_2 clusters and on the γ-alumina surface. These arguments are also in good accordance with the TPD data discussed in the next section.

Comparison of the IR data corresponding to the stepwise NO_2 (g) adsorption presented in Figures 31a and 31b indicates that the 8Ba/Ti/Al (P2) sample displays significant dissimilarities in the NO_x uptake behavior with respect to the 8Ba/Ti/Al (P1) system. It is evident from Figure 31b that the very initial NO_2 (g) exposure on the surface of the 8Ba/Ti/Al (P2) sample results in the appearance of adsorption bands at 1221 cm^{-1} with a shoulder at ~1185 cm^{-1} due to the formation of bidentate nitrates and nitrites on the surface. Related with the shrinking of the shoulder at 1185 cm^{-1}, further NO_2 (g) exposure leads to the appearance and growth of various types of nitrates coordinated to different adsorption sites. The spectrum of the fully saturated surface in Figure 31b consists of multiple vibrational bands of the bulk Ba-nitrates (at 1320, 1449 and 1483 cm^{-1}), surface (bidentate) nitrates on the Ba^{2+} sites

(1560, 1585 and ~1300 cm^{-1}), bidentate/bridged nitrates on the TiO_2 domains (at 1583 and 1628 cm^{-1}) and bidentate/bridged nitrates on the Al^{3+} adsorption sites (at 1294 and 1256 cm^{-1}). In addition, the feature at ~1985 cm^{-1} attributed to weakly adsorbed N_2O_3/ NO^+ on the alumina domains is more visible for the 8Ba/Ti/Al (P2) sample.

It is therefore apparent that NO_x adsorption signals associated with the titania domains are much more strongly pronounced for the 8Ba/Ti/Al (P2) sample in comparison to that of the 8Ba/Ti/Al (P1) system. Furthermore, in contrast to the 8Ba/Ti/Al (P1) sample, the ratio of the IR intensities of the bulk Ba-nitrate to surface Ba-nitrate signals is profoundly smaller for the 8Ba/Ti/Al (P2) surface. In other words, a greater amount of nitrates are stored on the 8Ba/Ti/Al (P2) surface, where they are adsorbed particularly on Ti^{4+} and surface $(BaO)_x$ units. In fact, the surface distribution of BaO strongly depends on the surface morphology of the TiO_2 domains. As discussed, surface TiO_2 domains provide very strong anchoring sites for BaO domains by limiting their surface mobility [1]. Most likely, the presence of homogenously distributed smaller TiO_2 crystallites on the Ti/Al (P2) support surface dictates a morphology of the surface BaO domains which exists mostly in the form of well-dispersed BaO units interacting with the underlying Ti/Al (P2) support surface.

In addition, it is worth mentioning that, the addition of 8 wt% BaO to the Ti/Al (P2) support material has also brought about an alteration in the distribution of the TiO_2/TiO_x domains, leaving bare Al^{3+} sites available for NO_x adsorption. This is evident by the observed adsorption bands at 1294 and 1256 cm^{-1} ascribed to the nitrates on the exposed alumina sites on the 8Ba/Ti/Al (P2) sample which are not that much visible in for the Ti/Al (P2) and 8Ba/Ti/Al (P1) samples. This argument is in line with the TPD data.

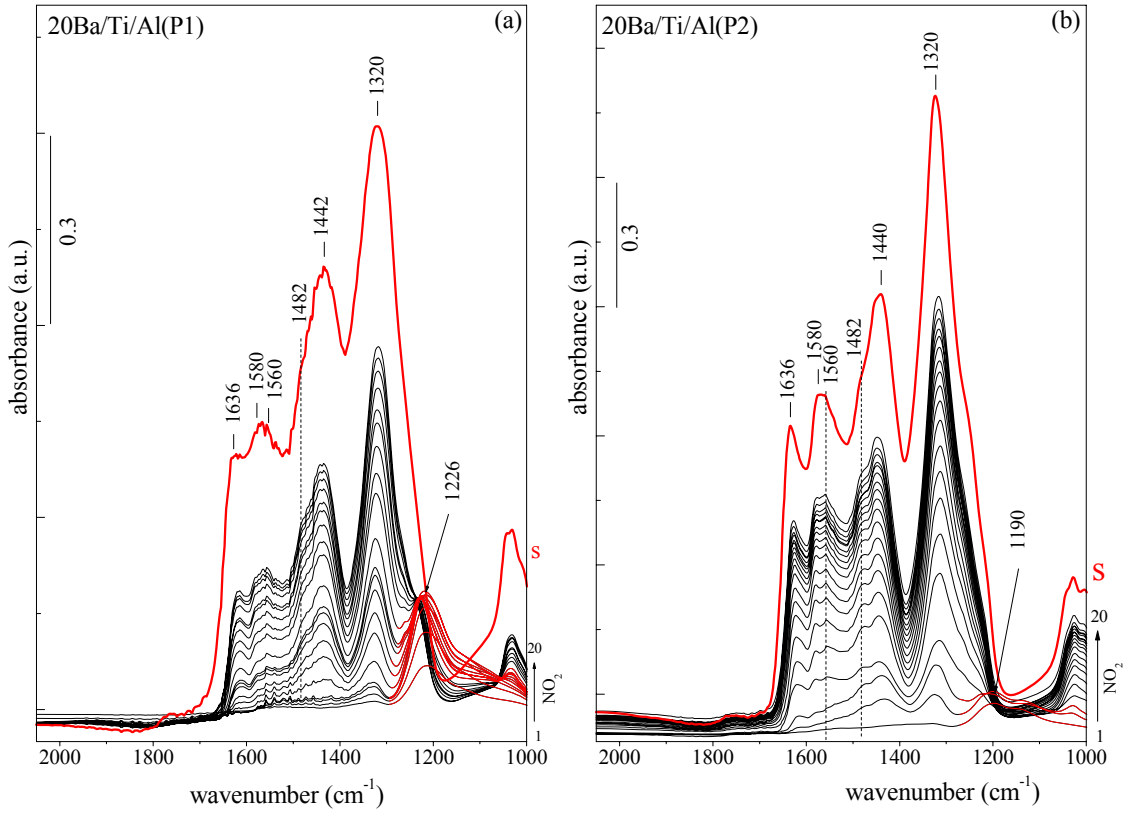

Figure 32. FTIR spectra corresponding to the stepwise NO_2 adsorption at 323 K on: (a) 20Ba/TiAl (P1) and (b) 20BaA/Ti/Al (P2) samples. The spectra corresponding to the fully saturated sample surfaces are marked with "S". (All spectra are acquired in vacuum at 323 K)

As can be seen in Figure 32, at higher BaO surface coverages (i.e. 20Ba/TiAl (P1, P2)), the vibrational bands due to the formation of bulk Ba-nitrates at 1320, 1442 and ~1482 cm^{-1} are strongly enhanced. On the other hand, the surface Ba-nitrate IR signals and the bidentate/bridged nitrates on the TiO_2 domains (1636 and 1580 cm^{-1}) become weaker in comparison to those observed for the 8Ba/Ti/Al (P1/P2) samples (Figures 31a and 31b). This effect is particularly visible for the 20Ba/Ti/Al (P1) sample (Figure 32a) implying that the formation of bulk BaO domains mostly in the form of large crystallites cover the large portion of the support surface. The surface is therefore left with a small fraction of the titania or alumina sites free for NO_x adsorption. Thus, the origin of the differences in the NO_x uptake properties of the 20Ba/Ti/Al (P1) sample with respect to the 20Ba/Ti/Al (P2) sample can be predominantly attributed to the formation of large and poorly-dispersed bulk BaO clusters located on the agglomerated TiO_2 domains of the 20Ba/Ti/Al (P1) surface. Such a morphology change also results in a significantly lower surface area for the 20Ba/Ti/Al (P1) sample as compared to the 20Ba/Ti/Al (P2) case (Table 3).

3.2.2.2 Thermal behavior of the adsorbed NO_x species on Ba/Ti/Al NO_x storage materials via TPD.

TPD profiles of 8Ba/Al and 20Ba/Al samples upon NO_2(g) adsorption (Figures 33 and 34), can be readily analyzed based on one of our former reports [66] and other studies in the literature [87, 89, 120, 122, 123]. The first major desorption feature for both 8(20)Ba/Al samples appears at 389 K due to the decomposition of the N_2O_3/NO^+ species. This is followed by a latter desorption feature associated with the decomposition of the nitrates that reside on the exposed γ-Al_2O_3 sites (600-650 K). Next, the decomposition of the surface (bidentate) nitrates on the BaO monomers/dimers that are strongly interacting with the support material (650-700 K) takes place by mostly releasing NO_2. Lastly, the decomposition of the bulk nitrates takes place at T > 900 K), mostly in the form of NO + O_2 [66, 87, 89, 120, 122, 123]. TPD data for the 8(20)Ba/Al samples can be used as a benchmark for the further analysis of the TPD results obtained for the 8(20)Ba/Ti/Al (P1/P2) materials

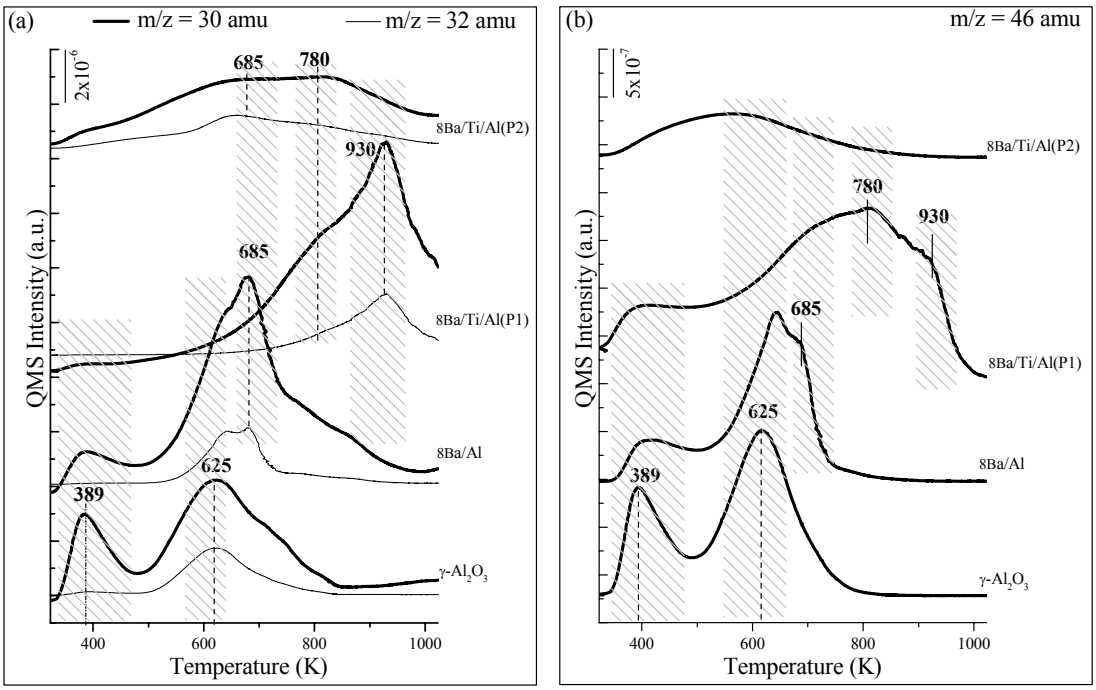

Figure 33. TPD profiles obtained from 8Ba/Ti/Al (P1), 8Ba/Ti/Al (P2), γ-Al_2O_3 and 8Ba/Al samples which were initially saturated with NO_2 (g) at 323 K. a) 30 amu and 32 amu signals, b) 46 amu signal.

TPD profile corresponding to the 8Ba/Ti/Al (P1) system (Figure 33a and 33b) shows that this material has a closer resemblance to the TPD data of the 20Ba/Al sample. It can be seen that the NO_x desorption profiles of the 8Ba/Ti/Al (P1) sample are dominated by an intense feature located at higher temperatures (930 K). In addition to this feature, an asymmetric lower desorption tail with a desorption maximum located at about 780 K is also detected. Despite the similarities between the desorption features of the 8Ba/Ti/Al (P1) and the 20Ba/Al samples, it is seen that the main desorption feature for the 8Ba/Ti/Al (P1) sample (930 K) appears at a higher temperature (20K) than for the 20Ba/Al sample (907 K). Furthermore, the asymmetric desorption feature for the 8Ba/Ti/Al (P1) at about 780 K is more intense than that of the 20Ba/Al case. Considering the surface morphology of the TiO_2 and BaO domains on the surface of the 8Ba/Ti/Al (P1) sample, it can be suggested that the dominant feature at 930 K is due to the decomposition of the bulk Ba-nitrates on the large BaO clusters which are located on the surface of the agglomerated TiO_2 particles. On the other hand, the low-temperature feature can be attributed to the convolution of signals originating from the decomposition of the nitrates on the TiO_2 crystallites (780 K) and the decomposition of the surface (bidentate) nitrates on the Ba-domains (650 – 700 K).

TPD data of 8Ba/Ti/Al (P2) system presented in Figures 33a and 33b (the topmost profiles) show significant differences from the results obtained for the 8Ba/Ti/Al (P1) sample. It is visible from the 8Ba/Ti/Al (P2) sample that the desorption feature at 930 K corresponding to the bulk nitrates on the BaO domains located on the surface of the TiO_2 crystallites is significantly suppressed. Moreover, the NO_x desorption profiles are almost exclusively dominated by the signals related to the nitrates on the TiO_2 domains (c.a. 780 K), the surface (bidentate) nitrates on the BaO monomers/dimers strongly interacting with the support material (650 - 700 K) and finally the NO_x adsorbed species on the exposed sites of γ-Al_2O_3 (~ 389 K and 600-650 K). These results are in very good accordance with the FTIR results for the NO_2 adsorption on the 8Ba/Ti/Al (P2) surface. Thus, the argument regarding the existence of BaO domains mostly in the form of well-dispersed BaO units directly interacting with the underlying support Ti/Al (P2) surface can also be used for interpreting the TPD results.

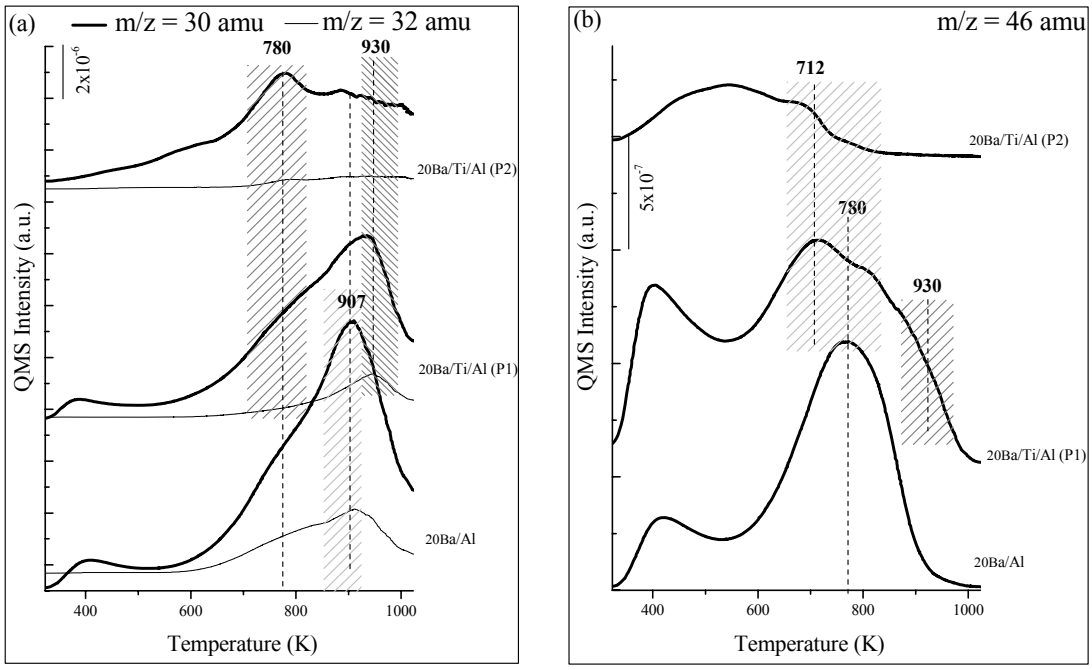

Figure 34. TPD profiles obtained from 20Ba/Ti/Al (P1), 20Ba/Ti/Al (P2) and 20Ba/Al samples which were initially saturated with NO_2 (g) at 323 K. a) 30 amu and 32 amu signals, b) 46 amu signal.

Despite the line shape resemblances of the NO_x desorption profiles of the 20Ba/Ti/Al (P1) sample with the 20Ba/Al system, the positions and the intensities of the desorption maxima are noticeably different. It can be seen that, the major desorption signals in the TPD profiles of the 20Ba/Ti/Al (P1) sample is shifted towards higher temperatures yielding a desorption maximum at about 930 K. The relative thermal stability of the bulk Ba-nitrates and their decomposition at higher temperatures are most likely due to the stronger interaction between the bulk BaO domains and the underlying titania sites where large BaO clusters are immobilized on the TiO_2/TiO_x domains. In addition to this, it is seen that the desorption feature at 700 K - 780 K (associated with surface nitrates on BaO and nitrates on titania sites) appearing as an asymmetric tail in the TPD profile of the 20Ba/Ti/Al (P1) sample in Figure 34a is relatively more visible than that for the 20Ba/Al system. Therefore, it is evident that that the surface morphology of the BaO domains on the 20Ba/Al and the 20Ba/Ti/Al (P1) samples are both dominated by large bulk-like BaO clusters. This explanation is also is in very good agreement with the current FTIR results as well as the characteristically low BET surface area values of the 20Ba/Ti/Al (P1) sample (Table 3). On the other hand, the TPD data given in Figure 34 for the 20Ba/Ti/Al (P2) sample reveals a different behavior where the most prominent desorption feature appears at 780 K. This major feature is also accompanied by a high-temperature desorption signal at 900 - 950 K and a low-temperature asymmetric tail at 600-700 K. In accordance with the current FTIR results, TPD data also indicate that the major NO_x species (i.e. desorption feature at 780 K) is associated with the nitrates that are bound to the surface of well-dispersed small $(BaO)_x$ units as well as to the nitrates bound to the titania domains. The high-temperature shoulder at 900 - 950 K can be attributed to relatively more stable nitrates in the form of bulk $Ba(NO_3)_2$ whereas the low temperature shoulder at 600 - 700 K can be associated with nitrates on alumina sites. The differences in the desorption characteristics of the 30 amu signal for the 20Ba/Ti/Al (P1) and 20Ba/Ti/Al (P2) samples are also in line with the significantly dissimilar 46 amu desorption signals for these two samples, emphasizing different decomposition and desorption pathways. Thus, TPD data is in harmony with the previously discussed results indicating that 20Ba/Ti/Al (P2) sample presents well-dispersed titania domains that control the surface mobility and the dispersion of the BaO domains.

3.2.3 Improvement of Sulfur Tolerance in NSR catalysts using $BaO/TiO_2/Al_2O_3$ ternary oxide systems as NO_x Storage Materials

3.2.3.1 FTIR Study of SO_x interaction with Ba/Ti/Al NO_x storage materials under lean conditions

It is known that the NO_x storage component NSR catalysts is susceptible to react with SO_2. SO_2 can be readily oxidized on the NSR catalyst forming $BaSO_4$ which deactivates the catalyst [29, 35, 44, 57]. Therefore, the challenge is to find an effective approach for the desulfation of the NSR catalysts. In the current work, a solution to this problem was proposed which involves the addition of TiO_2 into the binary 8(20)BaO/Al_2O_3 systems. The sulfation of the mixed Ti/Al (P1, P2) support materials were analyzed in detail in the above sections. Thus, this section deals with the fundamental understanding of the surface chemistry upon $SO_2 + O_2$ exposure on the ternary $BaO/TiO_2/Al_2O_3$ oxide systems via a powerful combination of FTIR and TPD techniques.

Before investigating the sulfation process occurring on the complex $BaO/TiO_2/Al_2O_3$ ternary oxide system, the IR-spectra of the adsorption of $SO_2 + O_2$ on the simpler 20 Ba/Al binary oxide system were studied as shown in Figure 35. It is visible that during the contact with SO_2 (g) + O_2 (g) at 323 K (Figure 35, spectrum *a*), 20 Ba/Al sample presents a broad absorption band at 1063 cm^{-1} indicating the presence of overlapping Ba-related sulfates/sulfites on the surface. When the sample temperature is increased to 473 K (Figure 35, spectrum *b*) the line shape slightly changes and the 1063 cm^{-1} feature shifts to 1046 cm^{-1} and an additional shoulder at 1109 cm^{-1} becomes apparent. The bands at 1109 cm^{-1} and 1063 cm^{-1} are characteristic for the S-O stretching vibrations of bidentate sulfates located on the surface of BaO [124-126**Error! Bookmark not defined.**]. At the same time, two minor bands located at 1242 cm^{-1} and 1162 cm^{-1} also appear. The bands at 1242 and 1162 cm^{-1} are attributed to bulk barium sulfate species [104]. It can be proposed that at 473 K both bulk and surface sulfates are present on the BaO domains.

.

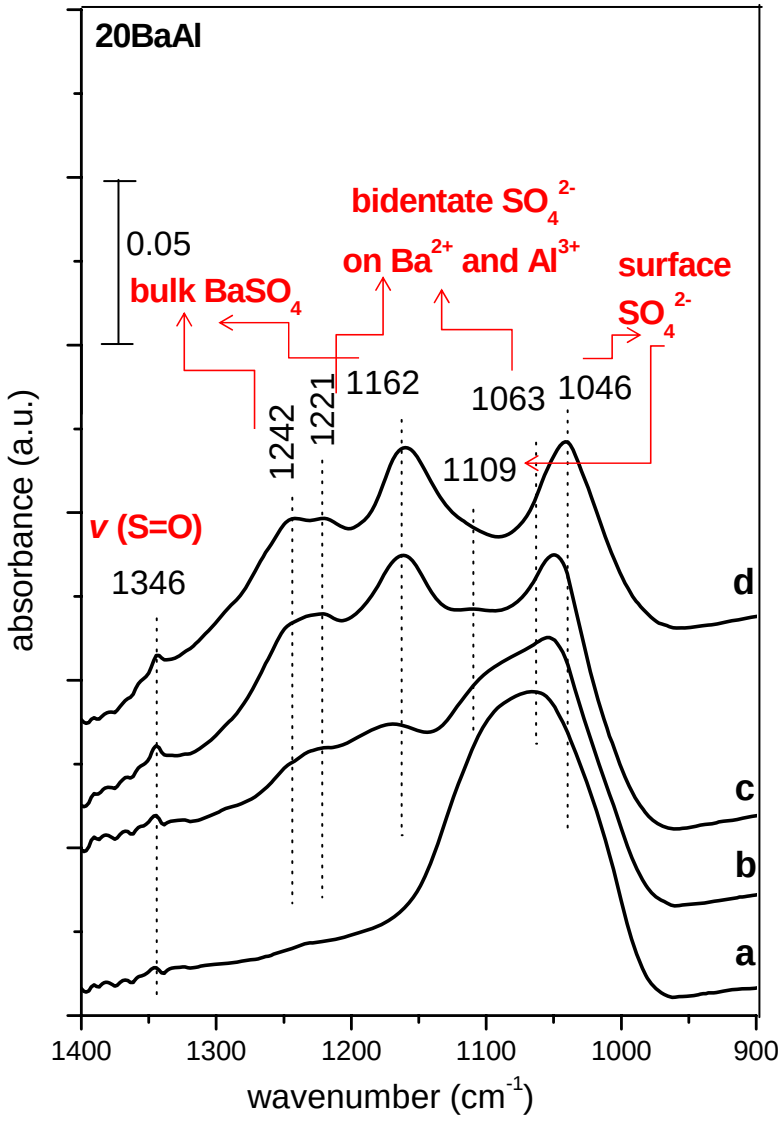

Figure 35. FTIR spectra acquired at 323 K for 20Ba/Al after exposure to SO_2 (g) + O_2 (g) (SO_2:O_2 Pressure Ratio = 0.1 Torr : 1 Torr) **a)** after 1 h in the mixture at 323 K, **b)** after flashing to 473 K in SO_2+O_2 and cooling back to 323 K in the gas mixture, **c)** after flashing the sample to 673 K in the gas mixture and further evacuation at 323 K for 20 min ($P_{reactor} < 1\times10^{-4}$ Torr), **d)** after flashing the sample to 673 K in vacuum ($P_{reactor} < 1\times10^{-4}$ Torr) and cooling back to 323 K.

The IR results obtained after flashing the sample to 673 K (Figure 35, spectra *c-d*) suggest that the intensity of the bulk barium sulfate related 1242 (ν_{as}) and 1162cm^{-1} (ν_s) peaks gradually grow, while the surface related $BaSO_4$ (1046 and 1109 cm^{-1}) species become suppressed. This indicates that as the sample temperature increases, a conversion of the surface Ba-sulfates to bulk Ba-sulfates are observed. Additionally, Figure 35 (spectrum *d*) shows a sharp band at 1046 cm^{-1} and a minor feature at 1346 cm^{-1} which is observed after heating the sample to 673 K followed by a further evacuation of the system. The 1346 cm^{-1} corresponds to the ν(S=O) vibration and is related to the tri-coordinated sulfate species on the Al_2O_3 support [103]. Bidentate (ionic) SO_4^{2-} coordinated to both Ba^{2+} and Al^{3+} sites might be the latter bands observed at $a_{\nu s}$ (SO_2) at 1221 cm^{-1} and ν_s (SO_2) at 1046cm^{-1}. The intensity of 1046 cm^{-1} is too high probably because of the overlapping surface Ba-SO_4^{2-} and/or ionic SO_4^{2-} coordinated to both Ba and Al sites. These observations suggest that initially there are bands related with the surface sulfates on BaO units and after the temperature treatment to 673K, bulk barium and surface aluminum sulfates are detected. This implies the migration and transformation of the surface Ba-sulfates into bulk Ba- sulfates.

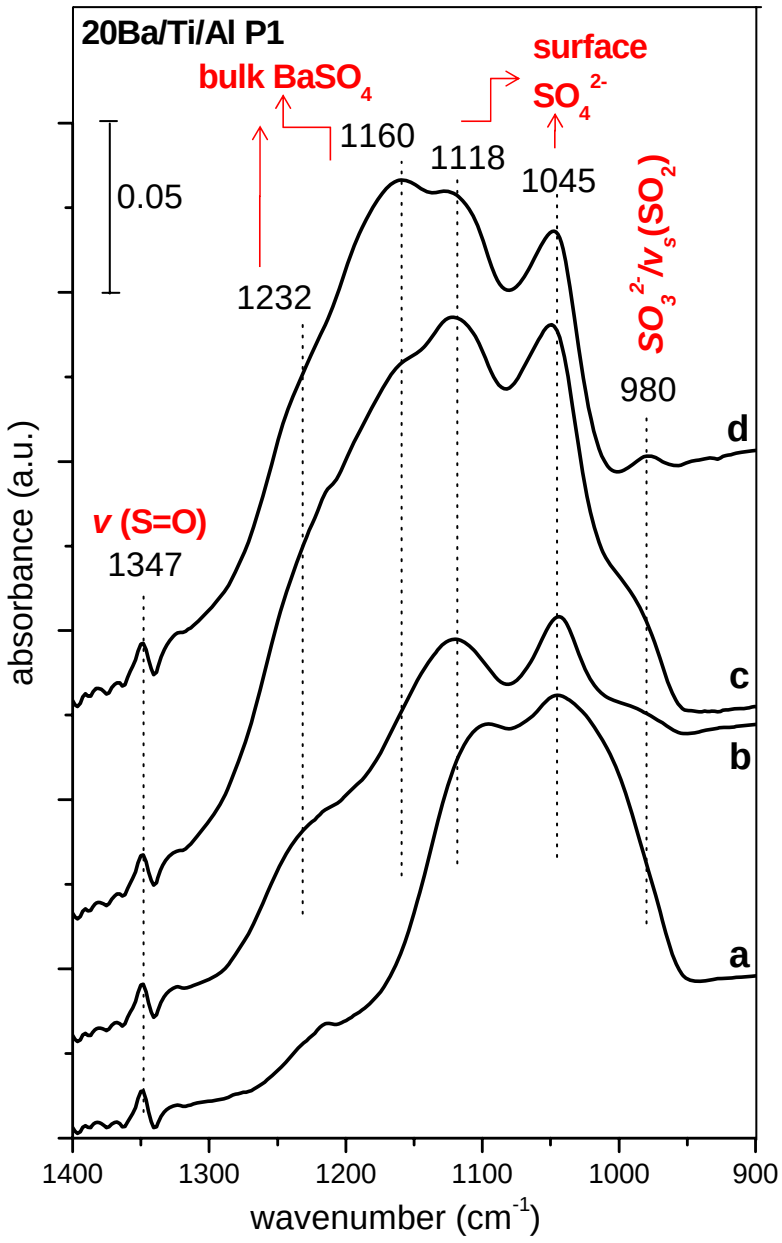

Figure 36. FTIR spectra acquired at 323 K for 20Ba/Ti/Al (P1) after exposure to SO_2 + O_2 (SO_2:O_2 Pressure Ratio = 0.1 Torr : 1 Torr) **a)** after 1 h in the mixture at 323 K, **b)** after flashing to 473 K in SO_2 + O_2 and cooling back to 323 K in the gas mixture, **c)** after flashing the sample to 673 K in the gas mixture and further evacuation at 323 K for 20 min ($P_{reactor} < 1\times10^{-4}$ Torr), **d)** after flashing the sample to 673 K in vacuum ($P_{reactor} < 1\times10^{-4}$ Torr) and cooling back to 323 K.

In order to illustrate the effect of SO_2 on the NO_x storage materials and investigate the influence of TiO_2 on the 20BaTi/Al (P1) system, sulfur poisoning experiments were performed (Figure 36). The pretreatment of the 20 Ba/Ti/Al (P1) sample with SO_2 + O_2 at 323 K (Figure 36, spectrum *a*) leads to the formation of surface Ba-sulfate species yielding features at 1118 and 1045 cm^{-1} [126]. The minor band at 1347cm^{-1} is related with the surface Al sulfates [126]. As the temperature increases to 473 K (Figure 36, spectrum *b*) the bulk-Ba sulfate species become more visible with the band at 1160 cm-1 (ν_s) and a shoulder at 1232 cm^{-1} (ν_{as}). Figure 36 spectra *c-d* show the evolution of an additional feature forming at 980 cm^{-1} after thermally treating at 673 K. The 980 cm^{-1} band might be related with the overlapping frequencies of sulfites and ν_s (SO_2) of surface sulfates. As discussed earlier in the current text TiO_2 on the 20BaTi/Al (P1) surface provides strong anchoring sites for the BaO domains, leaving a large fraction of free Al^{3+} sites available for SO_x adsorption, thus more Al-related sulfite/sulfates are expected to be observed in the presence of titania. The topmost spectrum in Figure 36 shows major features at 1160 (bulk Ba-sulfates), 1118 (surface Ba-sulfates), 1045 cm^{-1} (overlapping surface sulfates on Ba or Al) and minor bands positioned at 980 cm^{-1} (sulfites on Al or ν_s (SO_2)), 1237 (bulk Ba-sulfates) and 1347 cm^{-1} (surface alumina sulfates). These findings suggest that, TiO_2 changes the SO_x adsorption on the 20 Ba/Ti/Al (P1) sample by altering the surface acidity of the material and further preventing the bulk sulfate formation. Thus, surface sulfates are more prominent on the 20BaTi/Al (P1) surface and the transformation to bulk-like $BaSO_4$ species (1232, 1160 cm^{-1}) is hindered. Concomitantly, Al-related sulfite species become visible as the temperature increases

3.2.3.2 Influence of SO_2 poisoning on the NO_x adsorption behavior of the Ba/Ti/Al Systems via FTIR

The influence of sulfur poisoning on the NO_x adsorption behavior of the 8Ba/Ti/Al (P1), 20Ba/Ti/Al (P1) and 20 Ba/Ti/Al (P2) samples at 323 K were analyzed via IR spectroscopy. The NO_x storage performances/capacities of both fresh and poisoned samples were investigated in detail in a comparative manner.

Figure 37 compares the NO_x adsorption capacities of the 8 Ba/Ti/Al (P1), 20 Ba/Ti/Al (P1) and 20 Ba/Ti/Al (P2) samples before and after sulfation at 323 K. The adsorption of NO_2 on the fresh samples was already discussed in detail above. Briefly, the sample surfaces are characterized by adsorption bands due to the presence of the bulk (ionic) Ba-nitrates located at ~1320 cm^{-1}, ~1440 cm^{-1} and ~1480 cm^{-1} and surface (bidentate) BaO nitrates at 1585 cm^{-1}, 1565 cm^{-1}, 1300 cm^{-1} and additional nitrates at 1583 cm^{-1} and ~1630 cm^{-1} that are adsorbed on the TiO_2 domains with bidentate and bridged configurations. The surface (bidentate) Ba-nitrates are significantly suppressed and are overlapping with the nitrate signals associated with the titania domains.

After poisoning the samples with $SO_2 + O_2$ it is clearly visible that the NO_x storage capacities decrease significantly. Additionally, the presence of minor bands at ~1150 cm^{-1} and ~1245 cm^{-1} implies that there exists bulk-like Ba-sulfate species on all of the three samples at 323 K.

20Ba/Ti/Al (P1) sample exhibits large BaO crystallites (with a lower surface area) that cover both the Al^{3+} and Ti^{4+} sites. These larger BaO crystallites might have a lower relative tendency to accumulate SO_x species than that of the smaller BaO particles due to the higher diffusion barrier present for the larger particles which hinder the transport of SO_x species from the $BaSO_4$ surface shell to the BaO core.

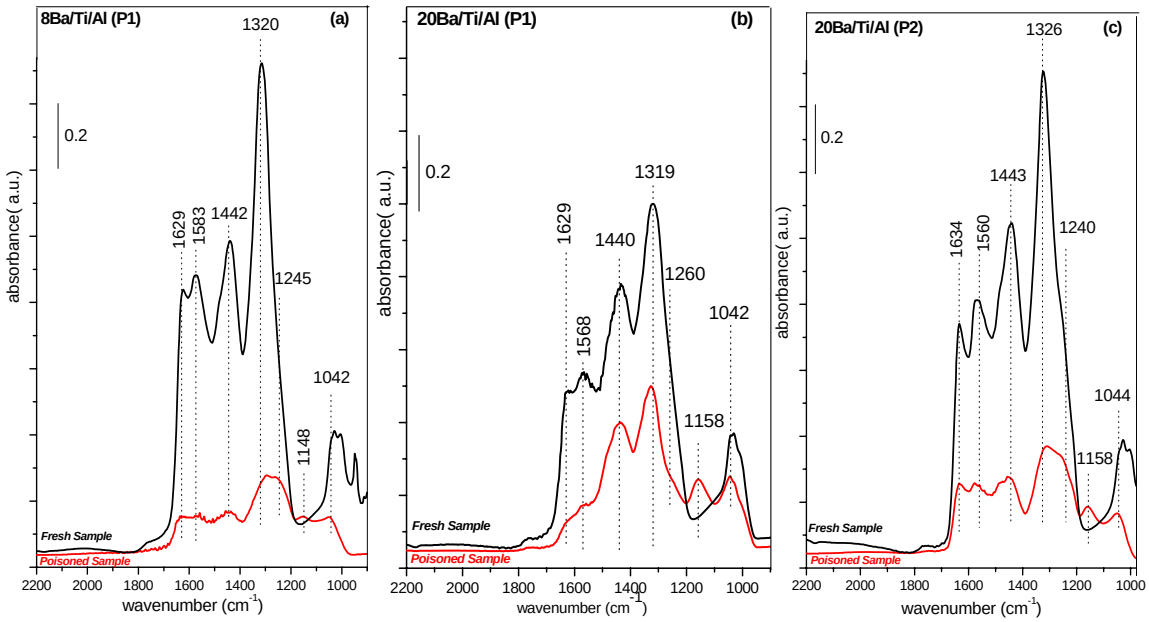

Figure 37. FTIR spectra corresponding to 8 Torr of NO_2 adsorption at 323 K on fresh (black spectra) and poisoned (red spectra) **a)** 8Ba/Ti/Al (P1) **b)** 20Ba/Ti/Al (P1) **c)** 20Ba/Ti/Al (P1) surfaces. Sulfation was performed by exposing SO_2 (g) + O_2 (g) (SO_2:O_2 Pressure ratio = 0.1 Torr : 1 Torr) on the sample at 323 K, followed by the heating of the sample in the gaseous mixture at 473 K for 30 min and a final evacuation at 323 ($P_{reactor} < 1x10^{-3}$). (NO_2 saturation of the surfaces were performed by dosing 8 Torr of NO_2 at 323 K for 20 min, followed by evacuation at 323 K. (All spectra are acquired at 323 K in vacuum).

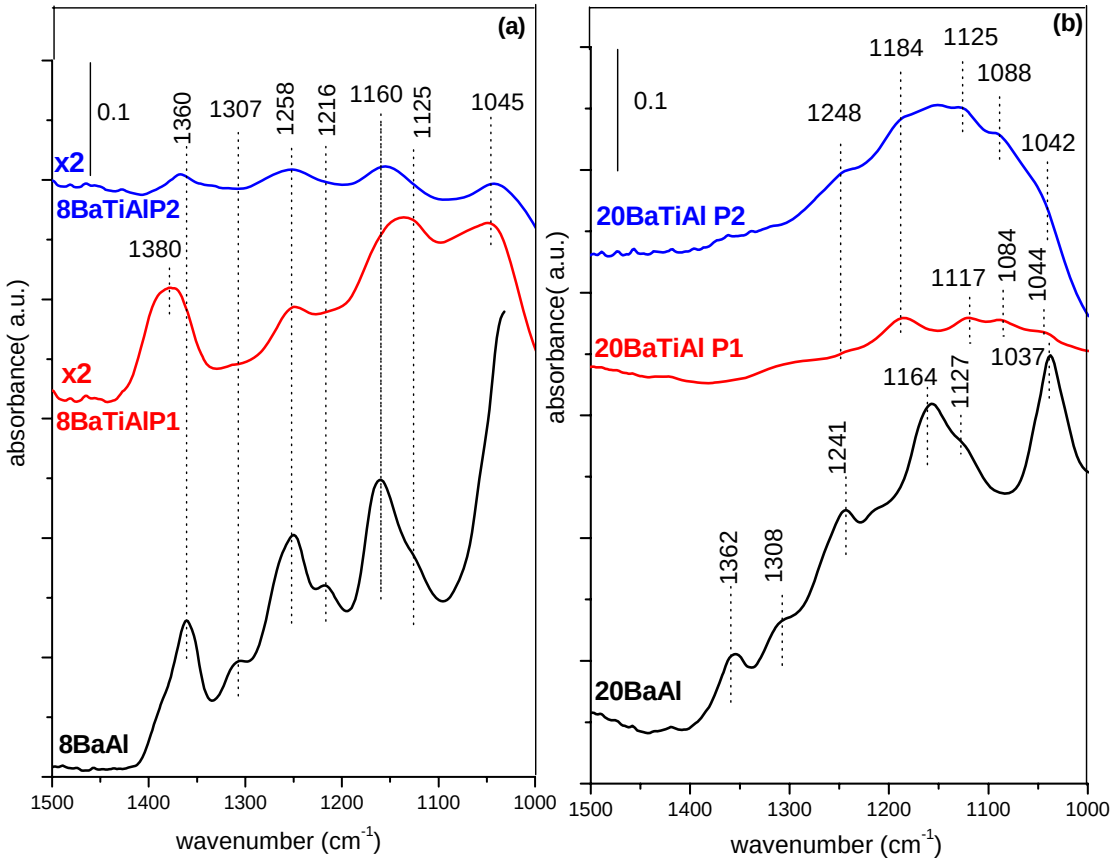

Figure 38. FTIR spectra acquired after dosing 8 Torr of NO_2 at 323 K on sulfated **a)** 8 Ba/Al (black spectra), 8 Ba/Ti/Al (P1) (red spectra), 8 Ba/Ti/Al (P2) (blue spectra) **b)** 20 Ba/Al (black spectra), 20 Ba/Ti/Al (P1) (red spectra), 20 Ba/Ti/Al (P2) (blue spectra) followed by further heating at 1023 K in vacuum. Sulfation was performed by exposing SO_2 (g) + O_2 (g) (SO_2:O_2 Pressure ratio = 0.1 Torr : 1 Torr) on the sample at 323 K, followed by the heating of the sample in the gaseous mixture at 473 K for 30 min and a final evacuation at 323 ($P_{reactor} < 1x10^{-3}$). (NO_2 saturation of the surfaces were performed by dosing 8 Torr of NO_2 at 323 K for 20 min, followed by evacuation at 323 K. (All spectra are acquired at 323 K in vacuum).

Figure 38 shows a series of FTIR results obtained on poisoned samples which are saturated with NO_2, then annealed to 1023 K in vaccum. It is visible that thermal treatment at 1023 K decomposes all of the nitrate-related features. It is directly evident that SO_x species are more stable than NO_x at high temperatures (1073 K). Moreover, the stabilities of the SO_x species on various NO_x storage materials containing different BaO loadings (8 and 20 wt %) show dissimilar trends at 1073 K. Figure 38 also clearly highlight the effect of TiO_2 on the sulfated NO_x storage materials. It is noticeable that 8Ba/Al and 20Ba/Al samples reveal more intense sulfate bands in comparison to the samples containing TiO_2 (8,20 Ba/Ti/Al (P1,P2)).

It can be seen in Figure 38 that 8Ba/Ti/Al (P2) sample has a smaller SO_x accumulation on its surface when compared with the 8Ba/Ti/Al (P1). This might be due to the fact that on 8Ba/Ti/Al (P2) the surface exhibits a rather disordered or an amorphous nature (compare XRD profiles corresponding to 1073 K in Figures 23 and 25). On the other hand, the 8Ba/Ti/Al (P1) surface consists of more ordered and better crystallized, $BaTiO_3$, TiO_2 (anatase) and $Ba_{1.23}Al_{2.46}Ti_{5.54}O_{16}$ domains which seem to have a higher affinity towards sulfates while 8Ba/Al surface which lacks Ti, seems to be the most vulnerable surface for sulfur poisoning. Note that the specific surface areas of the 8Ba/Ti/Al (P1, P2) samples are rather close to each other as seen on Table 3 (111 m^2/g and 146 m^2/g, respectively). Thus, the differences in the sulfur poisoning for these surfaces are not easy to account for by a mere surface area comparison.

For the 20Ba/Ti/Al (P1, P2) surfaces, XRD data given in Figures 24 and 26 and the BET results presented on Table 3 suggest that the 1073 K annealing protocol which is routinely performed to clean the surfaces before all of the adsorption experiments, result in significant structural differences between the 20Ba/Ti/Al (P1) and 20Ba/Ti/Al (P2) samples. First of all, while the specific surface area of the 20Ba/Ti/Al (P1) sample corresponding to red spectrum in Figure 38b is only about 59 m^2/g, this value corresponds to 95 m^2/g for the 20Ba/Ti/Al (P2). Thus, the surface with the significantly higher surface area is expected to have a greater exposure to SO_x and thus accumulate a larger extent of sulfates. Furthermore, XRD data given in Figures 24 and 26 also reveal that while the 20Ba/Ti/Al (P1) surface (after 1073 K annealing) consists of rather ordered/compact and relatively more stable/inert phases such as rutile and $BaAl_2O_4$, under the same conditions,

20Ba/Ti/Al (P2) surface consists of rather disordered/open and rather more reactive phases such as $BaTiO_3$ and $Ba_{1.23}Al_{2.46}Ti_{5.54}O_{16}$. Hence it can be argued that the more disordered, more open and more reactive 20Ba/Ti/Al (P2) surface is more prone to sulfate poisoning as seen in Figure 38b while the 20Ba/Al sample that lacks any Ti has least tolerance for sulfur poisoning.

3.2.3.3 Thermal stability of the adsorbed NO_x species on the SO_2 treated Ba/Ti/Al NOx storage materials

In order to compare the NO_x uptake properties of poisoned and fresh $BaO/TiO_2/Al_2O_3$ ternary oxide NO_x storage materials, TPD experiments were performed after NO_2 adsorption. Results of these experiments are presented in Figures 39 and 40.

The NO_x desorption features from the fresh 8 Ba/Ti/Al (P1) sample were already discussed in detail. Briefly, the dominant feature at 930 K was suggested to be the decomposition of the bulk Ba-nitrates on the larger BaO clusters which were located on the agglomerated TiO_2 particles. The low-temperature feature was attributed to the convolution of signals originating from the decomposition of the nitrates on the large TiO_2 crystallites (780 K) and the decomposition of the surface (bidentate) nitrates on the Ba-domains (650 – 700 K).

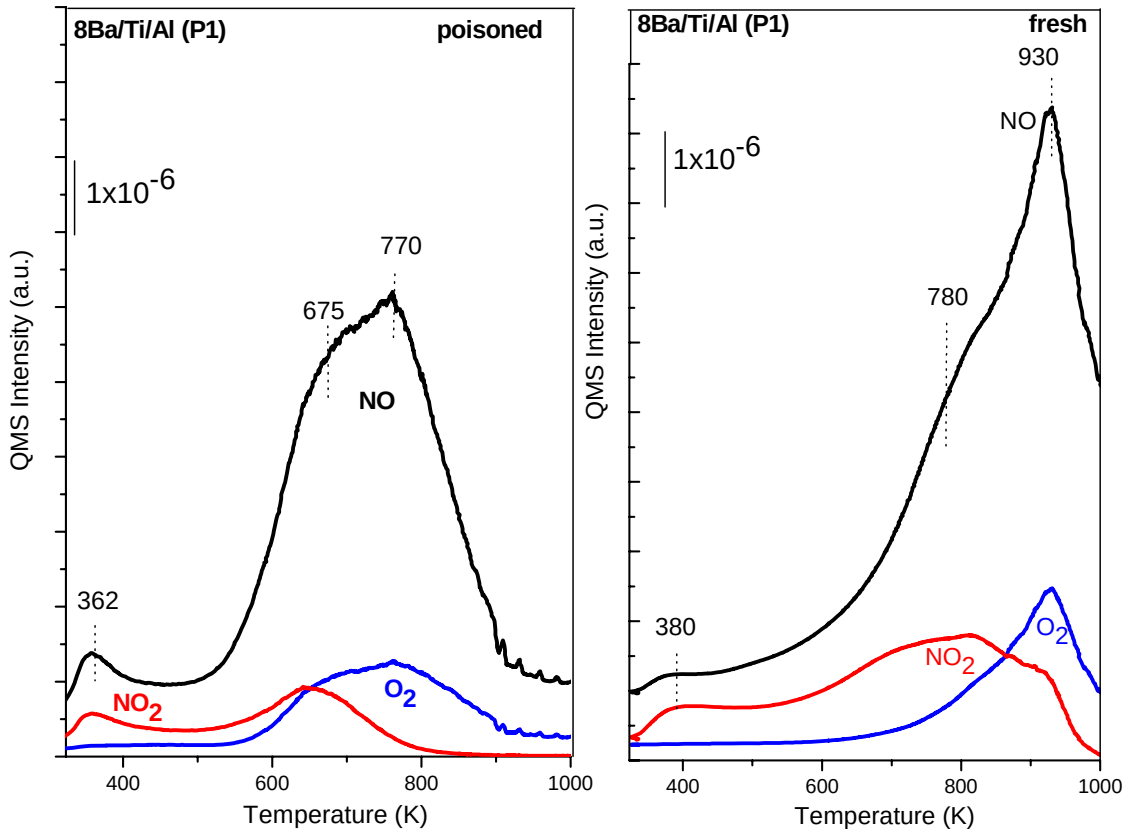

Figure 39. TPD profiles obtained from poisoned and fresh 8Ba/Ti/Al (P1) samples which are saturated with 8 Torr NO_2 (g) at 323 K for 20 min. Black, blue and red curves correspond to 30 amu (NO), 32 amu (O_2) and 46 amu (NO_2) signals, respectively. (Before the NO_2 adsorption, sample was poisoned via SO_2 (g) + O_2 (g) exposure at 323 K, where SO_2:O_2 pressure ratio was 0.1 Torr : 1 Torr, followed by further heating in the gaseous mixture at 473 K for 30 min and a final evacuation at 323 K).

The addition of SO_x increases the desorption of weakly adsorbed species as observed for the corresponding support material Ti/Al (P1). The IR spectra illustrates that sulfur poisoning of the sample decreases both the amount of NO_x that is stored on the sample as well as the stability of these stored NO_x species, which was also confirmed in the FTIR spectra in Figure 37a. The prominent desorption band observed for the poisoned sample is located at 770 K, with a shoulder at 675 K. The high temperature desorption feature allocated at 930 K is not detected, meaning that the SO_x species most probably interacts with the larger BaO clusters and blocks these sites for NO_x adsorption. Unlike the fresh sample, poisoned sample yields more pronounced NO_x desorption features (650-700 K) associated with surface BaO and TiO_2 sites rather than the bulk BaO. Furthermore, it is worth mentioning that the desorption/decomposition of the stored NO_x is completed at c.a. 900 K for the 8 Ba/Ti/Al (P1) sample which clearly emphasizes the destabilization effect of the sulfates on the stored nitrate species.

TPD data given in Figure 40 for the 20Ba/Ti/Al (P2) samples reveal a rather similar line shape for both fresh and poisoned samples where the major desorption feature appears at 780 K. However, it is obvious that the total NO_x uptake significantly diminishes after sulfur poisoning which is in perfect agreement with the corresponding FTIR results presented in Figure 37c. This 780 K NO_x desorption feature is suggested to be associated with the well dispersed titania domains as well as bulk BaO domains. Furthermore, a high-temperature desorption signal at 900-950 K and a low temperature asymmetric tail at 600-700 K are also visible. The high temperature shoulder at 900-950 K can be attributed to more stable nitrates from bulk $Ba(NO_3)_2$ whereas the low temperature shoulder at 600-700 K can be associated with nitrates on alumina sites.

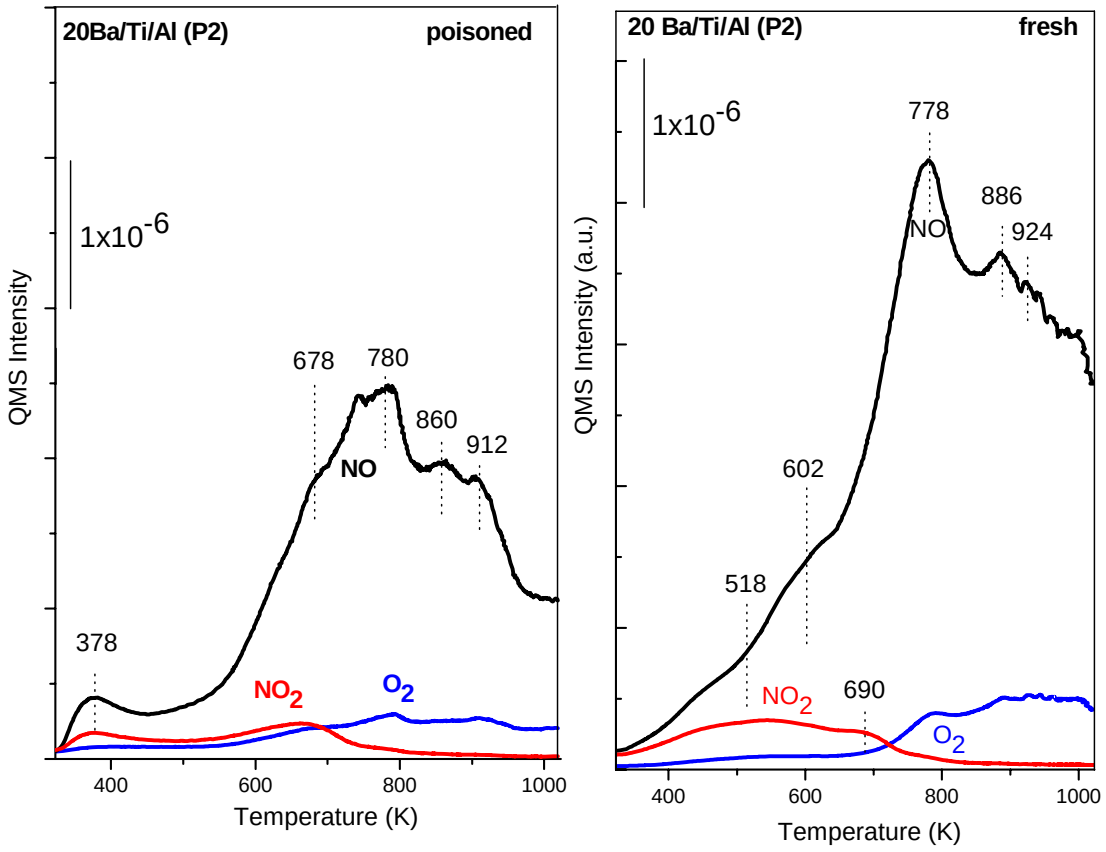

Figure 40. TPD profiles obtained from poisoned and fresh 20Ba/Ti/Al (P2) samples which are saturated with 8 Torr NO_2 (g) at 323 K for 20 min. Black, blue and red curves correspond to 30 amu (NO), 32 amu (O_2) and 46 amu (NO_2) signals, respectively. (Before the NO_2 adsorption, sample was poisoned via SO_2 (g) + O_2 (g) exposure at 323 K, where SO_2:O_2 pressure ratio was 0.1 Torr : 1 Torr, followed by further heating in the gaseous mixture at 473 K for 30 min and a final evacuation at 323 K).

3.2.3.4 Thermal stability of the adsorbed SO_x species on the Ti/Al support materials

The stability of the formed SO_x species on the NO_x storage materials after saturating with NO_2 was further analyzed. In order to understand the adsorption/desorption profiles of the poisoned samples, SO_2 (m/z = 64) and H_2S (m/z = 34) signals were monitored for each sample spectrum as seen in Figure 41.

The desorption profiles of SO_2 from the NO_x storage materials are shown in Figure 41. The desorption spectra generally exhibit a broad desorption profile in the temperature range of 400 - 800 K, probably attributed to weakly adsorbed SO_2 species or surface-related sulfate decomposition. It is seen that the sulfate decomposition continues at temperatures above 1000 K. In Figure 41, it is generally seen that the NO_x storage materials prepared via P2 reveal smaller sulfur accumulation. Furthermore, the addition of titania is also observed to decrease the SO_x desorption maxima by destabilizing the sulfate species.

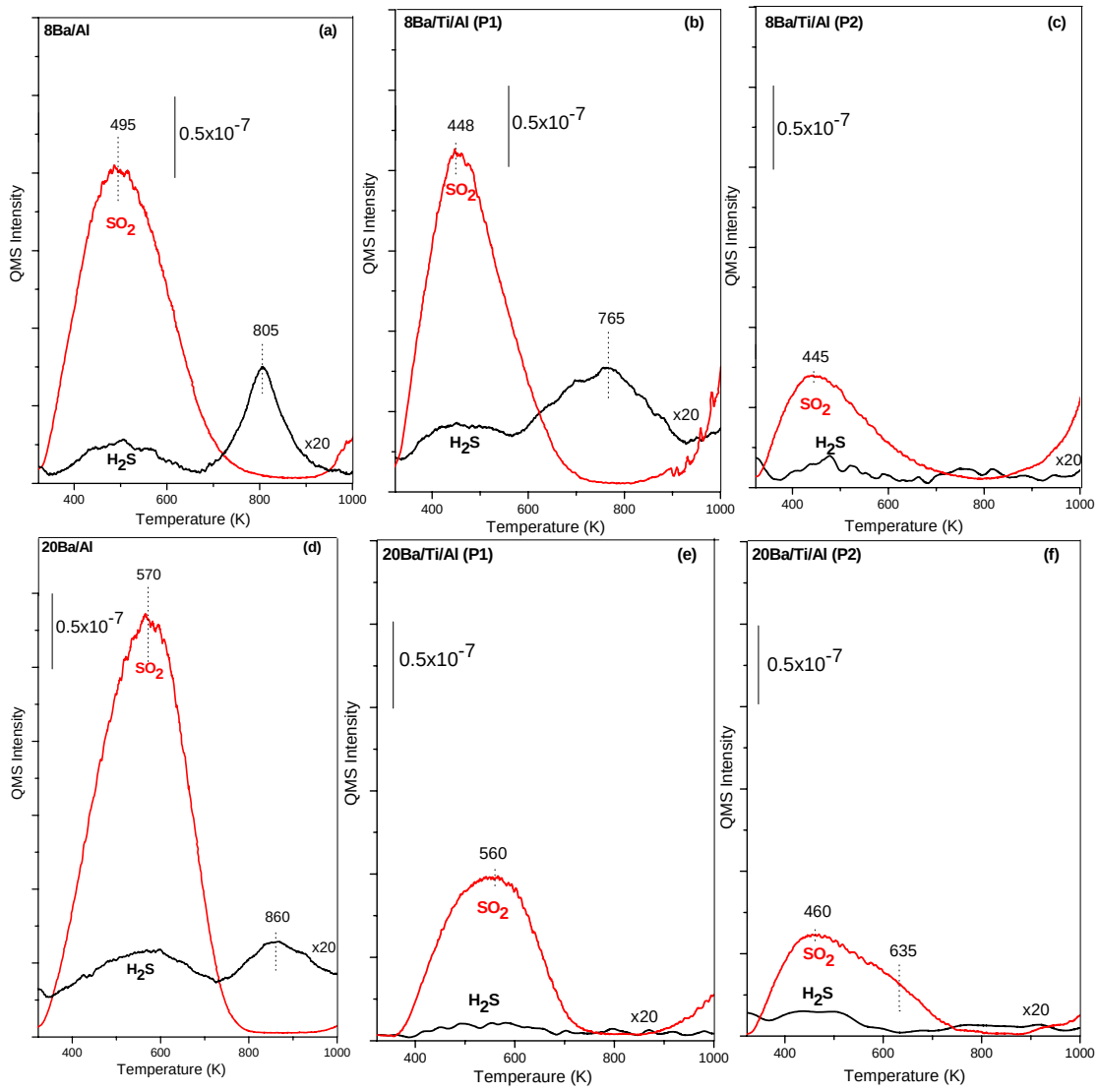

Figure 41. SO_2 and H_2S desorption profiles for a) 8Ba/Al, b) 8Ba/Ti/Al (P1) c) 8Ba/Ti/Al (P2) d) 20Ba/Al, e) 20Ba/Ti/Al (P1), f) 20Ba/Ti/Al (P2) surfaces which are first poisoned with SO_2 (g) + O_2 (g) at 323 K (SO_2:O_2 pressure ratio = 0.1 Torr : 1 Torr) and then heated in this gas mixture at 473 K for 30 min followed by saturation with NO_2 at 323 K.

4 CONCLUSIONS

It is important to understand the interactions occurring between the catalytic components of the complex NO_x storage materials in order to design new materials with improved catalytic properties. In this current work, the structural characterization and functionality/performance of Ti/Al binary oxide support materials in comparison with Ba/Ti/Al ternary oxide NO_x storage materials were investigated in detail. It was demonstrated that the surface dispersion and the mobility of the BaO domains in a NO_x storage material can be fine-tuned with the help of a well-dispersed underlying oxide domain (e.g. TiO_2) which functions as a strong anchoring site for the BaO units. The results are particularly relevant for having a molecular understanding of the sulfur tolerance effect of TiO_2 in NSR systems. The main results of the current work can be summarized as follows:

(a) Ti/Al (P2) samples synthesized by the sol-gel co-precipitation technique have significantly higher specific surface area values for the temperature interval within 623 – 873 K than that of the Ti/Al (P1) material.

(b) TiO_x / TiO_2 domains on the TiO_2/Al_2O_3 support materials derived from two different synthetic protocols exhibited different surface distributions where P2 synthetic route yielded a distinctively more homogenous distribution of TiO_x domains.

(c) The sol-gel co-precipitation synthetic route (P2) results in the formation of a support material structure (Ti/Al(P2)) with almost no discernible crystalline phases at $T \leq 1073$ K.

(d) An improved Ba surface dispersion was observed for the $BaO/TiO_2/Al_2O_3$ materials synthesized via the co-precipitation of alkoxide precursors (P2). Increased BaO dispersion was found to originate mostly from the increased fraction of accessible TiO_2/TiO_x sites on the surface.

(e) The studied NO_x storage systems exhibited different surface acidities. The presence of Ti-containing domains yielded additional medium-strength Lewis acid sites, whereas the presence of Ba domains decreased both the number and the strength of the surface Lewis acid sites.

(f) In the Ba/Ti/Al system, strong interaction between Ti- and Ba-containing domains results in significant surface reactions above 873 K where formation of $Ba_{1.23}Al_{2.46}Ti_{5.54}O_{16}$, $BaTiO_3$ and possibly $BaTi_2O_5$ and/or a complex $Ba_xAl_yTi_zO_n$ phase was observed. These high-temperature species can also shed some light on the surface transformations that the NSR systems undergo up on thermal aging.

(g) The presence of TiO_2 (anatase) crystallites on the TiO_2/Al_2O_3 and $BaO/TiO_2/Al_2O_3$ systems with different surface morphologies significantly influences the nature of the formed NO_x species by providing additional Ti^{4+} NO_x storage sites which are able to store NO_x predominantly in the form of bridged and bidentate nitrates and also by altering the domain size of the BaO clusters.

(h) Two different types of NO_x species were detected on the titania sites, with distinctively different thermal stabilities. The relative thermal stabilities of the NO_x species investigated in the current study can be ranked in the following increasing order: NO^+/N_2O_3 on alumina << nitrates on alumina < surface nitrates on BaO < bridged/bidentate nitrates on large/isolated TiO_2 clusters < bulk nitrates on BaO on alumina surface and bridged/bidentate nitrates on TiO_2 crystallites homogenously distributed on the surface < bulk nitrates on the BaO sites located on the TiO_2 domains.

(i) TPD profiles suggested that $SO_2 + O_2$ adsorption on pure Al_2O_3 resulted in strongly bonded surface sulfate, SO_4^{2-}/Al_2O_3, species that were thermally stable up to T > 1073 K. The surface sulfates related with TiO_2 completely decomposed below T < 780 K.

(j) SO_x species enhances the weakly adsorbed NO^+/N_2O_3 formation on the γ-Al_2O_3 and the molecular adsorbed SO_2 species on the ternary oxide systems.

(k) SO_x adsorption hinders the formation of stable nitrate species that desorb at relatively high temperatures and definitely decrease the NO_x adsorption capacities.

(l) SO_x uptake properties of the $BaO/TiO_2/Al_2O_3$ materials were found to be strongly influenced by the morphology of the TiO_2/TiO_x domains and the BaO loadings (8/20 wt% BaO).

(m) The presence of TiO_2 domains was seen to decrease the SO_x desorption temperatures from investigated the NO_x storage materials.

(n) Bulk sulfate formation was influenced by the presence of NO_x species. At high temperatures (T > 1073K), the sulfate species were strongly adsorbed on NO_x storage materials whereas the nitrates decomposed at relatively lower temperatures, indicating the higher stability of the sulfates.

5 REFERENCES

[1] Andonova, S.M., Şentürk, G.S., Kayhan, E., Ozensoy, E., *J. Phys. Chem. C* **2009,** *113*, 11014.

[2] Andonova, S.M., Şentürk, G.S., Ozensoy E., accepted in *J.Phys.Chem. C*

[3] http://en.wikipedia.org/wiki/Fossil_fuel.

[4] Takahashi, N.; Suda, A.; Hachisuka, I.; Sugiura, M.; Sobukawa, H.; Shinjoh, H. *Appl. Catal. B: Environ.* **2007**, *72*, 187.

[5] Matsumoto, S. *Cattech* **2000**, *4, 102.*

[6] Klingstedt, F.; Arve, K.; Eränen, K.; Murzin, D.Y. *Acc. Chem. Res.* **2006**, *4*, 273.

[7] Neeft, J.P.A.; Makkee, M.; Moulijn, J.A. *Fuel Process. Technol.* **1996**, *47* 1.

[8] http://www.aecc.be/en/Publications/Publications.html.

[9] http://openlearn.open.ac.uk.

[10] Koebel, M.; Media, G.; Elsener, M.; *Catal. Today*, **2002**, *73*, 239.

[11] Toyota Patent, European Patent Application no. 0573 672A1, **1992**.

[12] Takahashi, N.; Shinjoh, H.; Iijima, T.; Suzuki, T.; Yamazaki, K.; Yokota, K.; Suzuki, H.; Miyoshi, N.; Matsumoto, S.; Tanizawa, T.; Tanaka, T.; Tateishi, S.; Kasahara K. *Catal. Today,* **1996**, *27, 63.*

[13] Miyoshi, N.; Matsumoto, S.; Katoh, K.; Tanaka, T.; Harada, J.; Takahashi, N.; Yokota, K.; Sugiura M.; Kasahara, K., *SAE Technical Paper* 950809, **1995**.

[14] Matsumoto, S.; *Catal. Today, **1996**, 29, 43.*

[15] Epling, W.S.; Campbell, L.E.; Yezerets, A.; Currier, N.W.; Parks II, J.E. *Catal. Reviews,* **2004**, *46, 163.*

[16] Roy, S.; Baiker, A. *Chem. Rev.*, **2009**, *109,* 4054.

[17] Olsson, L.; Fridell E., *J. Catal.*, **2002**, *210,* 34.

[18] Olsson, L.; Andersson, B., *Top. Catal.* **2004**, *28*, 89.

[19] Szailer, T.; Kwak, J.H.; Kim, D.H.; Hanson J.C.; Peden, C.H.F.; Szanyi, J., *Journal of Catalysis,* **2006**, *239*, 51.

[20] Hepburn, J.S.; Thanaslu, E.; Dobson, D.A.; Watkins, W.L., SAE Technical Paper 962051, **1996**

[21] Bögner, W.; Krämer, M.; Krutzsch, B.; Pischinger, S.; Voigtländer, D.; Wenninger, G.; Wirbeleit, F.; Brogan, M.S.; Brisley, R.J.; Webster, D.E., *Appl. Catal. B*, **1995**, *7*, 153.

[22] Machida, M.; Yasuoka, K.; Eguchi, K.; Arai, H., *J. Chem. Soc., Chem. Commun.* **1990**, *17*, 1165.

[23] Fridell, E.; Skoglundh, M.; Johansson, S.; Westerberg, B.; Torncrona, A.; Smedler, G., *Stud. Surf. Sci. Catal.,* **1998**, *116*, 537.

[24] Mahzoul, H.; Brilhac, J.F.; Gilot, P., *Appl. Catal. B*, **1999**, *20*, 47.

[25] Fridell, E.; Skoglundh, M.; Westerberg, B.; Johansson, S.; Smedler, G., *J. Catal.,* **1999**, *183*, 196.

[26] Fekete, N.; Kemmler, R.; Voigtlander, D.; Krutzsch, B.; Zimmer, E.; Wenninger, G.; Strehlau, W.; Van Der Tillaart, J.A.A.; Leyrer, J.; Lox, E.S.; Müller, W., *SAE Technical Paper* 970746, **1997**

[27] Gill, L. J.; Blakeman, P.G.; Twigg, M.V.; Walker, A.P., *Topics in Catalysis*, **2004**, *28*, 1.

[28] Matsumoto, S.; Ikeda, Y.; Suzuki, H.; Ogai, M.; Miyoshi N. *Appl. Catal. B,* **2000**, *25*, 115.

[29] Matsumoto, S.; Kazuaki, S.; Shinji, T.; Yasuo, I. *Catalysts Catal.,* **2000**, *42*, 65.

[30] Chang, J.-R.; Chang, S. L.; Lin, T.-B. *J. Catal.,* **1997**, *169*, 338.

[31] Uy, D.; Wiegand, K. A.; O'Neill, A. E.; Dearth, M. A.; Weber, W. H., *J. Phys. Chem. B,* **2002**, *106*, 387.

[32] Wei, X.; Liu, X.; Deeba, M. *Appl. Catal., B,* **2005**, *58*, 41.

[33] Snis, A.; Miettinen, H. *J. Phys. Chem. B,* **1998**, *102*, 2555.

[34] Rohr, F.; Peter, S.D.; Lox, E.; Kogel, M.; Sassi, A.; Juste, L.; Rigaudeau, C.; Belot, G.; Gelin, P.; Primet, M. *Appl. Catal. B: Environ.* **2005**, *56, 201.*

[35] Stakheev, A.Yu.; Gabrielsson, P.; Gekas, I.; Teleguina, N.S.; Bragina, G.O.; Tolkachev, N.N.; Baeva, G.N., *Top. Catal.,* **2007**, *42-43,* 143.

[36] Corbos, E.C.; Elbouazzaoui, S.; Courtois, X.; Bion, N.; Marecot, P.; Duprez, D. *Top., Catal.,* **2007**, *42-43, 9.*

[37] Misono, M.; Inui, T. *Catal. Today,* **1999**, *51,* 369.

[38] Fritz, A.; Pitchon, V. *Appl. Catal. B,* **1997**, *13*, 1.

[39] Dawody, J.; Tonniesa, I.; Fridell, E.; Skoglundh, M. *Top. Catal*., **2007**, *4243*, 183.

[40] Hendershot, R.J.; Rogers, W.B.; Snively, C.M.; Ogunnaike, B.A.; Lauterbach, J., *Catal.Today,* **2004**, *98*, 375.

[41] Hendershot, R.J.; Rogers, W.B.; Snively, C.M.; Lauterbach, J., *Appl. Catal. B,* **2007**, *70*, 160.

[42] Luo, J-Y.; Meng, M.; Zha, Yu.-Q.; Xie, Ya-N.; Hu, T.-D.; Zhang J., Liu, T. *Appl., Catal. B, **2008**, 78,* 38.

[43] http://www.metro.tokyo.jp/ENGLISH/TOPICS/2004/fteac300.htm

[44] Yamazaki, K.; Suzuki, T.; Takahashi, N.; Yokota, K.; Sugiura, M., *Appl. Catal. B*., **2001**, *30*, 459.

[45] Fanson, P.T.; Horton, M.R.; Deglass, W.N.; Lauterbach, J., *Appl. Catal. B*., **2003**, *46*, 393.

[46] Basile, F.; Fornasari, G.; Grimandi, A.; Livi, M.; Vaccari, A., *Appl. Catal. B*., **2006**, *69*, 58.

[47] Huang, H.Y.; Long, R.Q.; Yang, R.T., *Appl. Catal. B*., **2001**, *33*, 127.

[48] Hodjati, S.; Petit, C.; Pitchon, V.; Kiennemann, A., *Appl. Catal. B*., **2001**, *30*, 247.

[49] Hepburn, J.S.; Watkins, W.L.H., US Patent 5,758,489, **1998**.

[50] Centi, G.; Fornasari, G.; Gobbi, C.; Livi, M.; Trifiro, F.; Vaccari, A., *Catal. Today*, **2002**, *73*, 287.

[51] Clacens, J.M.; Montiel, R.; Kochkar, H.; Figueras, F.; Guyon, M.; Beziat, J.C., *Appl. Catal. B.*, **2004**, *53*, 21.

[52] Hachisuka, I.; Hirata, H.; Ikeda, Y.; Matsumoto, S., SAE Technical Paper, **2000**, 2000-01-1196

[53] Miyoshi, N.; Matsumoto, S., Stud. Surf. Sci. Catal., 1999, 121, 245.

[54] Breen, J.P.; Marella, M.; Pistarino, C.; Ross, J.R.H., *Catal. Lett*., **2002**, *123*, 128.

[55] Corbos, E.C.; Courtois, X.; Bion, N.; Marecot, P.; Duprez, D., *Appl. Catal. B*., **2008**, *80*, 62

[56] Wetchakun, N.; Phanichphant, S., *Current Applied Physics,* **2008***, 8,* 343.

[57] Hirata, H.; Hachisuka, I.; Ikeda, Y.; Tsuji, S.; Matsumoto, S., *Top.Catal.* **2001**, *16/17*, 145.

[58] Yamamoto, K.; Kikuchi, R.; Takeguchi, T.; Eguchi, K. *J. Catal.,* **2006**, *238*, 449.

[59] Suzuki, H.; Muramoto, R.; Takahashi, N., *Toyota Tech. Re*V., **1996**, *46*, 68.

[60] Imagawa, H.; Tanaka, T.; Takahashi, N.; Matsunaga, S.; Suda, A.; Shinjoh, H., *Appl. Catal., B,* **2009**, *86*, 63.

[61] Liu, Y.; Meng, M.; Zou, X.; Li, X.; Zha, Y., *Catal. Commun.,* **2008**, *10*, 173.

[62] Liu, Y.; Meng, M.; Li, X.-G.; Guo, L.-H.; Zha, Y.-Q., *Chem. Eng.Res. Des.,* **2008**, *86*, 932.

[63] Shelimov, B.N.; Tolkachev, N.N.; Tkachenko, O.P.; Baeva, G.N.; Klementiev, K.V.; Stakheev, A.Yu.; Kazansky, V.B., *J. Photochem. Photobiol A,* **2008**, *195*, 81.

[64] Kawabata, K.; Yoshimatsu, H.; Fujiwara, K.; Yabuki, T.; Osaka, A.; Miura, Y., *J. Mater. Science,* **1999**, *34*, 2529.

[65] Macleod, N.; Cropley, R.; Keel, J.M.; Lambert, R.M., *J. Catal*., **2004**, *221*, 20.

[66] Kayhan, E.; Andonova, S.M.; Şentürk, G.S.; Chusuei, C. C.; Ozensoy, E., *J. Phys. Chem. C,* **2010**, *114*, 357.

[67] Kantcheva, M. ; Hadjiivanov, K. I.; Klissurski, D. G., *J. Catal.,* **1992**, *134*, 299.

[68] Yang, J.; Huang, Y. X.; Ferreira, J. M. F., *J. Mater. Sci. Lett.,* **1997**, *16*, 1933.

[69] Orendorz, A.; Brodyanski, A.; Lo¨sch, A.; Bai, L. H.; Chen, Z. H.; Le, Y. K.; Ziegler, C.; Gnaser, H., *Surf. Sci.,* **2007**, *601*, 4390.

[70] Su, W.; Zhang, J.; Feng, Zh.; Chen, T.; Ying, P.; Li, C., *J. Phys.Chem. C,* **2008**, *112*, 7710.

[71] Oshaka, T.; Izumi, F.; Fujiki, Y., *J. Raman Spectrosc.,* **1978**, *7*, 321.

[72] Bersani, D.; Lottici, P. P.; Ding, X.-Z., *Appl. Phys. Lett.,* **1998**, *72*, 73.

[73] Zhang, Y.-H.; Chan, C. K.; Porter, J. F.; Guo, W.J., *J. Mater. Res.,* **1998**, *13*, 2602.

[74] Bersani, D.; Antonioli, G.; Lottici, P. P.; Lopez, T., *J. Non-Cryst.Solids,* **1998**, *232-234*, 175.

[75] Kumar, K. N. P.; Keizer, K.; Burggraff, A. J.; Okubo, T.; Nagomoto, H.; Morooka, S., *Nature,* **1992**, *358*, 48.

[76] Wang, Z.; Deng, X. *Mater. Sci. Eng. B,* **2007**, *140*, 109.

[77] Kim, S.; Wang, X.; Buda, C.; Neurock, M.; Koper, O. B.; Yates, J. T., *J. Phys. Chem. C,* **2009**, *113*, 2219.

[78] Healy, M. H.; Wieserman, L. F.; Arnett, E. M.; Wefers, K., *Langmuir,* **1989**, *5*, 114.

[79] Morterra, C.; Chiorino, A.; Ghiotti, G.; Garrone, E., *J. Chem. Soc., Faraday Trans.,* **1979**, *75*, 271.

[80] Abbattista, F.; Delmastro, S.; Gozzelino, G.; Mazza, D.; Vallino, M.; Busca, G.; Lorenzelli, V.; Ramis, G., *J. Catal.,* **1989**, *117*, 42.

[81] Kline, C.H.Jr.; Turkevich, J. *J. Chem. Phys.* **1944**, *12*, 300.

[82] Haneda, M.; Joubert, E.; Menezo, J.-Ch.; Duprez, D.; Barbier, J.; Bion, N.; Daturi, M.; Saussey, J.; Lavalley, J.-C.; Hamada, H., *Phys. Chem. Chem. Phys.,* **2001**, *3*, 1366.

[83] Lundie, D. T.; Mclnroy, A. R.; Marshall, R.; Winfield, J. M.; Jones, P.; Dudman, C. C.; Parker, S. F.; Mitchell, C.; Lennon, D., *J. Phys. Chem. B,* **2005**, *109*, 11592.

[84] Kooli, F.; Sasaki, T.; Watanabe, M.; Martin, C.; Rives, V. *Langmuir,***1999**, *15*, 1090.

[85] Bezrodna, T.; Puchkovska, G.; Shimanovska, V.; Chashechnikova, I.; Khalyavka, T.; Baran, J., *Appl. Surf. Sci.,* **2003**, *214*, 222.

[86] Li, J.; Zhu, Y.; Ke, R.; Hao, J. *Appl. Catal., B:En*V*iron.,* **2008**, *80*, 202.

[87] Szanyi, J.; Kwak, J.H.; Chimentao, R.J.; Peden, C.H.F., *J. Phys. Chem. C,* **2007**, *111*, 2661.

[88] Ozensoy, E.; Herling, D.; Szanyi, J., *Catal. Today,* **2008**, *136,* 46.

[89] Szailer, T.; Kwak, J. –H.; Kim, D. –H.; Szanyi, J; Wang, C.; Peden, C.H.F. *Catal. Today* **2006**, *114,* 86.

[90] Sedlmair, C..; Seshan, K.; Jentys, A.; Lercher, J.A., *J. Catal.,* **2003**, 214, 308.

[91] Venkov, T.; Hadjiivanov, K.; Klissurski, D., *Phys. Chem. Chem. Phys.,* **2002**, *4*, 2443.

[92] Kantcheva, M, *J. Catal.,* **2001**, *204*, 479.

[93] Hadjiivanov, K.; Bushev V.; Kantcheva, M.; Klissurski, D., *Langmuir,* **1994,** *10,* 464.

[94] Wu, J.C.S.; Cheng, Y.-T., *J. Catal.*, **2006**, *237*, 393.

[95] Ramis, G.; Busca G.; Lorenzelli V.; Forzatti, P.; *Appl. Catal*., **1990**, *64*, 243.

[96] Ozkan, U.S.; Watson, R.B., *Catal. Today*, **2005**, *100*, 101.

[97] Mitchell, M.B.; Sheinker, N., J. Phys. Chem., **1996,** 100, 7550.

[98] Chang, C. C. *J. Catal,*. **1978**, *53*, 374.

[99] Karge, H. G.; Dalla Lana, I. G. *J. Phys.; Chem.,* **1984**, *88*, 1538

[100] Davydov, A.A., *Molecular spectroscopy of oxide catalyst surfaces*, Wiley, Chichester, England, **2003**

[101] Waqif, M.; Pieplu, A.; Saur, O.; Lavalley, J.C.; Blanchard, G., *Solid State Ionics*, **1997**, *95*, 163

[102] Abdulhamid, H.; Fridell, E.; Dawody, J.; Skoglundh, M., *J. Catal.*, **2006,** *241*, 200

[103] Saur, O.; Bensitel, M.; Mohammed Saad, A. B.; Lavalley, J. C.; Tripp, C. P.; Morrow, B. A., *J. Catal,*. **1986**, *99*, 104.

[104] Waqif, M.; Lavelly, J.C.; Perathoner, S.; Centi, G., *J. Phys. Chem.*, **1991**, *95*, 4051.

[105] Kantcheva, M.; Vakkasoglu, A.S., *J.Catal*., **2004**, *223*, 352.

[106] Colthup, N.B.; Daly, L.H.; Wiberley, S.E., *Introduction to Infrared and Raman Spectroscopy, Academic Press*, New York, **1964.**

[107] Nakamoto, K., *Infrared Spectra of Inorganic and Coordination Compounds*, 2nd Ed., Wiley-Interscience, New York, **1960**

[108] Ross, S.D., *Inorganic Infrared and Raman Spectra*, McGraw-Hill, London, **1972**

[109] Ryan, R.R.; Kubas, G.J.; Moody, D.C.; Eller, P.G., *Struct. Bonding*, **1981**, *46*, 47

[110] Xu, W.; He, H.; Yu, Y., *J. Phys. Chem. C*, **2009**, *113*, 4426.

[111] Luo, T.; Gorte, R. J., *Appl. Catal., B,* **2004**, *53*, 77.

[112] Takeuchi, M.; Matsumoto, S., *Top. Catal.,* **2004**, *28*, 151.

[113] Fisher, J. G.; Lee, B.-K.; Choi, S.-Y.; Wang, S.-M.; Kang, S.-J. L., *J. Eur. Ceram. Soc.,* **2006**, *26*, 1619.

[114] Mestl, G.; Rosynek, M. P.; Lunsford, J. H., *J. Phys. Chem. B,* **1997**, *101*, 9321.

[115] Hess, Ch.; Lunsford, J. H. *J. Phys. Chem. B,* **2003**, *107*, 1982.

[116] Hess, Ch.; Lunsford, J. H. *J. Phys. Chem. B,* **2002**, *106*, 6358.

[117] Mestl, G.; Rosynek, M. P.; Lunsford, J. H. *J. Phys. Chem. B,* **1998**, *102*, 154.

[118] Kwak, J. H.; Kim, D. H.; Szailer, T.; Peden, C. H. F.; Szanyi, J. *Catal. Lett.* **2006**, *111*, 119.

[119] Szanyi, J.; Kwak, J. H.; Hanson, J.; Wang, C.; Szailer, T.; Peden, C. H. F. *J. Phys. Chem. B* **2005**, *109*, 7339.

[120] Kwak, J. H.; Hu, J. Z.; Kim, D. H.; Szanyi, J.; Peden, C. H. F., *J.Catal.,* **2007**, *251*, 189.

[121] Kwak, J.H.; Mei, D.; Yi, C.-W.; Kim, D.H.; Peden, C.H.F.; Allard, F.; Szanyi J. *J. Catal.* **2009**, *261,* 17.

[122] Szanyi, J.; Kwak, J.H.; Kim, D.H.; Burton, S.D.; Peden, C.H.F. *J. Phys. Chem. B* **2005**, *109,* 27.

[123] Szanyi, J.; Kwak, J.H.; Kim, D.H.; Wang, X.Q.; Chimentao, R.; Hanson, J.; Epling, W.S.; Peden, C.H.F. *J. Phys. Chem. C,* **2007**, *111*, 4678.

[124] Schoonheydt, R.A. .; Lunsford, J.H., *J. Catal*., **1972**, *26*, 261.

[125] M.A. Babaeva, A.A. Tsyganenko, V.N. Filimonov, Kinet. Katal. **1985**, 787.

[126] Sedlmair, C.; Seshan, K.; Jentys, A.; Lercher, J.A., *Catal. Today,* **2002**, *75*, 413.

APPENDIX

The table shows the SO_x assignments on the studied samples.

Al_2O_3	SO_2(g): 1350 cm^{-1} ν_{as} (S-O) 1150 cm^{-1} ν_s (S-O)	SO_3^{2-}: 1073 cm^{-1} 1049 cm^{-1}	Surface SO_4^{2-}: 1368 cm^{-1} ν (S=O) 1102 cm^{-1} ν_{as} (SO2) 994cm^{-1} ν_s (SO2)	Bulk $Al_2(SO_4)_3$: 1170 cm^{-1}
TiO_2	SO_2(g): 1350 cm^{-1} ν_{as} (S-O) 1150 cm^{-1} ν_s (S-O)	SO_3^{2-}: 1083 cm^{-1}	Surface SO_4^{2-}: 1366, 1356 cm^{-1} ν (S=O) 1046 cm^{-1} ν_{as} (SO_2) 1002 cm^{-1} ν_s (SO_2)	Bidentate SO_4^{2-}: 1287 cm^{-1} ν_{as} (SO_2) 1160 cm^{-1} ν_s (SO_2)
$BaO/Al_2O_3/TiO_2$	SO_3^{2-}: 980 cm^{-1} ν_s (SO_2)	Surface $BaSO_4$: 1118 cm^{-1} 1045 cm^{-1}	Bidentate SO_4^{2-} on Ba and Al: 1221 cm^{-1} ν_{as} (SO_2) 1063 cm^{-1} ν_s (SO_2)	Bulk $BaSO_{4(s)}$: 1242 cm^{-1} ν_{as} (SO_2) 1162 cm^{-1} ν_s (SO_2)

Some of the figures in this manuscript are reproduced from previous publications and their copyright permissions are presented below.

SPRINGER LICENSE
TERMS AND CONDITIONS

Jul 15, 2010

This is a License Agreement between Goksu Seda Senturk ("You") and Springer ("Springer") provided by Copyright Clearance Center ("CCC"). The license consists of your order details, the terms and conditions provided by Springer, and the payment terms and conditions.

All payments must be made in full to CCC. For payment instructions, please see information listed at the bottom of this form.

License Number	2467120688720
License date	Jul 13, 2010
Licensed content publisher	Springer
Licensed content publication	CATTECH
Licensed content title	Catalytic Reduction of Nitrogen Oxides in Automotive Exhaust Containing Excess Oxygen by NOx Storage-Reduction Catalyst
Licensed content author	Shin'ichi Matsumoto
Licensed content date	Mar 1, 2000
Volume number	4
Issue number	2
Type of Use	Thesis/Dissertation
Portion	Figures
Author of this Springer article	No
Order reference number	
Title of your thesis / dissertation	FINDING AN OPTIMUM SURFACE CHEMISTRY FOR BaO/TiO2/Al2O3 SYSTEMS AS NOx STORAGE MATERIALS
Expected completion date	Jul 2010
Estimated size(pages)	160
Total	0.00 USD
Terms and Conditions	

Introduction
The publisher for this copyrighted material is Springer Science + Business Media. By clicking "accept" in connection with completing this licensing transaction, you agree that the following terms and conditions apply to this transaction (along with the Billing and Payment terms and conditions established by Copyright Clearance Center, Inc. ("CCC"), at the time that you opened your Rightslink account and that are available at any time

at http://myaccount.copyright.com).

Limited License
With reference to your request to reprint in your thesis material on which Springer Science and Business Media control the copyright, permission is granted, free of charge, for the use indicated in your enquiry. Licenses are for one-time use only with a maximum distribution equal to the number that you identified in the licensing process.

This License includes use in an electronic form, provided it is password protected or on the university's intranet, destined to microfilming by UMI and University repository. For any other electronic use, please contact Springer at (permissions.dordrecht@springer.com or permissions.heidelberg@springer.com)

The material can only be used for the purpose of defending your thesis, and with a maximum of 100 extra copies in paper.

Although Springer holds copyright to the material and is entitled to negotiate on rights, this license is only valid, provided permission is also obtained from the (co) author (address is given with the article/chapter) and provided it concerns original material which does not carry references to other sources (if material in question appears with credit to another source, authorization from that source is required as well). Permission free of charge on this occasion does not prejudice any rights we might have to charge for reproduction of our copyrighted material in the future.

Altering/Modifying Material: Not Permitted
However figures and illustrations may be altered minimally to serve your work. Any other abbreviations, additions, deletions and/or any other alterations shall be made only with prior written authorization of the author(s) and/or Springer Science + Business Media. (Please contact Springer at permissions.dordrecht@springer.com or permissions.heidelberg@springer.com)

Reservation of Rights
Springer Science + Business Media reserves all rights not specifically granted in the combination of (i) the license details provided by you and accepted in the course of this licensing transaction, (ii) these terms and conditions and (iii) CCC's Billing and Payment terms and conditions.

Copyright Notice:
Please include the following copyright citation referencing the publication in which the material was originally published. Where wording is within brackets, please include verbatim.
"With kind permission from Springer Science+Business Media: <book/journal title, chapter/article title, volume, year of publication, page, name(s) of author(s), figure number(s), and any original (first) copyright notice displayed with material>."

Warranties: Springer Science + Business Media makes no representations or warranties with respect to the licensed material.

Indemnity

You hereby indemnify and agree to hold harmless Springer Science + Business Media and CCC, and their respective officers, directors, employees and agents, from and against any and all claims arising out of your use of the licensed material other than as specifically authorized pursuant to this license.

No Transfer of License
This license is personal to you and may not be sublicensed, assigned, or transferred by you to any other person without Springer Science + Business Media's written permission.

No Amendment Except in Writing
This license may not be amended except in a writing signed by both parties (or, in the case of Springer Science + Business Media, by CCC on Springer Science + Business Media's behalf).

Objection to Contrary Terms
Springer Science + Business Media hereby objects to any terms contained in any purchase order, acknowledgment, check endorsement or other writing prepared by you, which terms are inconsistent with these terms and conditions or CCC's Billing and Payment terms and conditions. These terms and conditions, together with CCC's Billing and Payment terms and conditions (which are incorporated herein), comprise the entire agreement between you and Springer Science + Business Media (and CCC) concerning this licensing transaction. In the event of any conflict between your obligations established by these terms and conditions and those established by CCC's Billing and Payment terms and conditions, these terms and conditions shall control.

Jurisdiction
All disputes that may arise in connection with this present License, or the breach thereof, shall be settled exclusively by the country's law in which the work was originally published.

Other terms and conditions:

v1.2

Gratis licenses (referencing $0 in the Total field) are free. Please retain this printable license for your reference. No payment is required.

If you would like to pay for this license now, please remit this license along with your payment made payable to "COPYRIGHT CLEARANCE CENTER" otherwise you will be invoiced within 48 hours of the license date. Payment should be in the form of a check or money order referencing your account number and this invoice number RLNK10814580.
Once you receive your invoice for this order, you may pay your invoice by credit card. Please follow instructions provided at that time.

Make Payment To:
Copyright Clearance Center
Dept 001
P.O. Box 843006
Boston, MA 02284-3006

If you find copyrighted material related to this license will not be used and wish to cancel, please contact us referencing this license number 2467120688720 and noting the reason for cancellation.

Questions? customercare@copyright.com or +1-877-622-5543 (toll free in the US) or +1-978-646-2777.

AMERICAN CHEMICAL SOCIETY LICENSE
TERMS AND CONDITIONS

Jul 15, 2010

This is a License Agreement between Goksu Seda Senturk ("You") and American Chemical Society ("American Chemical Society") provided by Copyright Clearance Center ("CCC"). The license consists of your order details, the terms and conditions provided by American Chemical Society, and the payment terms and conditions.

All payments must be made in full to CCC. For payment instructions, please see information listed at the bottom of this form.

License Number	2467110797649
License Date	Jul 13, 2010
Licensed content publisher	American Chemical Society
Licensed content publication	The Journal of Physical Chemistry C
Licensed content title	Nature of the Ti−Ba Interactions on the BaO/TiO2/Al2O3 NOx Storage System
Licensed content author	Stanislava M. Andonova et al.
Licensed content date	Jun 1, 2009
Volume number	113
Issue number	25
Type of Use	Thesis/Dissertation
Requestor type11	Not specified
Format	Print and Electronic
Portion	Table/Figure/Micrograph
Number of Table/Figure/Micrographs	8
Author of this ACS article	Yes
Order reference number	
Title of the thesis / dissertation	FINDING AN OPTIMUM SURFACE CHEMISTRY FOR BaO/TiO2/Al2O3 SYSTEMS AS NOx STORAGE MATERIALS
Expected completion date	Jul 2010
Estimated size(pages)	160
Billing Type	Invoice
Billing Address	Bilkent University Chemistry Department ANKARA, other 06800 Turkey
Customer reference info	
Total	0.00 USD
Terms and Conditions	

Thesis/Dissertation

ACS / RIGHTSLINK TERMS & CONDITIONS
THESIS/DISSERTATION

INTRODUCTION
The publisher for this copyrighted material is the American Chemical Society. By clicking "accept" in connection with completing this licensing transaction, you agree that the following terms and conditions apply to this transaction (along with the Billing and Payment terms and conditions established by Copyright Clearance Center, Inc. ("CCC"), at the time that you opened your Rightslink account and that are available at any time at <http://myaccount.copyright.com>).

LIMITED LICENSE
Publisher hereby grants to you a non-exclusive license to use this material. Licenses are for one-time use only with a maximum distribution equal to the number that you identified in the licensing process; any form of republication must be completed within 60 days from the date hereof (although copies prepared before then may be distributed thereafter).

GEOGRAPHIC RIGHTS: SCOPE
Licenses may be exercised anywhere in the world.

RESERVATION OF RIGHTS
Publisher reserves all rights not specifically granted in the combination of (i) the license details provided by you and accepted in the course of this licensing transaction, (ii) these terms and conditions and (iii) CCC's Billing and Payment terms and conditions.

PORTION RIGHTS STATEMENT: DISCLAIMER
If you seek to reuse a portion from an ACS publication, it is your responsibility to examine each portion as published to determine whether a credit to, or copyright notice of, a third party owner was published adjacent to the item. You may only obtain permission via Rightslink to use material owned by ACS. Permission to use any material published in an ACS publication, journal, or article which is reprinted with permission of a third party must be obtained from the third party owner. ACS disclaims any responsibility for any use you make of items owned by third parties without their permission.

REVOCATION
The American Chemical Society reserves the right to revoke a license for any reason, including but not limited to advertising and promotional uses of ACS content, third party usage, and incorrect figure source attribution.

LICENSE CONTINGENT ON PAYMENT
While you may exercise the rights licensed immediately upon issuance of the license at the end of the licensing process for the transaction, provided that you have disclosed complete and accurate details of your proposed use, no license is finally effective unless and until full payment is received from you (by CCC) as provided in CCC's Billing and Payment terms and conditions. If full payment is not received on a timely basis, then any license preliminarily granted shall be deemed automatically revoked and shall be void as if never granted. Further, in the event that you breach any of these terms and conditions or any of

CCC's Billing and Payment terms and conditions, the license is automatically revoked and shall be void as if never granted. Use of materials as described in a revoked license, as well as any use of the materials beyond the scope of an unrevoked license, may constitute copyright infringement and publisher reserves the right to take any and all action to protect its copyright in the materials.

COPYRIGHT NOTICE: DISCLAIMER
You must include the following copyright and permission notice in connection with any reproduction of the licensed material: "Reprinted (“Adapted” or “in part”) with permission from REFERENCE CITATION. Copyright YEAR American Chemical Society."

WARRANTIES: NONE
Publisher makes no representations or warranties with respect to the licensed material.

INDEMNITY
You hereby indemnify and agree to hold harmless publisher and CCC, and their respective officers, directors, employees and agents, from and against any and all claims arising out of your use of the licensed material other than as specifically authorized pursuant to this license.

NO TRANSFER OF LICENSE
This license is personal to you or your publisher and may not be sublicensed, assigned, or transferred by you to any other person without publisher's written permission.

NO AMENDMENT EXCEPT IN WRITING
This license may not be amended except in a writing signed by both parties (or, in the case of publisher, by CCC on publisher's behalf).

OBJECTION TO CONTRARY TERMS
Publisher hereby objects to any terms contained in any purchase order, acknowledgment, check endorsement or other writing prepared by you, which terms are inconsistent with these terms and conditions or CCC's Billing and Payment terms and conditions. These terms and conditions, together with CCC's Billing and Payment terms and conditions (which are incorporated herein), comprise the entire agreement between you and publisher (and CCC) concerning this licensing transaction. In the event of any conflict between your obligations established by these terms and conditions and those established by CCC's Billing and Payment terms and conditions, these terms and conditions shall control.

JURISDICTION
This license transaction shall be governed by and construed in accordance with the laws of the District of Columbia. You hereby agree to submit to the jurisdiction of the courts located in the District of Columbia for purposes of resolving any disputes that may arise in connection with this licensing transaction.

THESES/DISSERTATION TERMS
Publishing implications of electronic publication of theses and dissertation material
Students and their mentors should be aware that posting of theses and dissertation material on the Web prior to submission of material from that thesis or dissertation to an ACS journal may affect publication in that journal. Whether Web posting is considered prior

publication may be evaluated on a case-by-case basis by the journal's editor. If an ACS journal editor considers Web posting to be "prior publication", the paper will not be accepted for publication in that journal. If you intend to submit your unpublished paper to ACS for publication, check with the appropriate editor prior to posting your manuscript electronically.

If your paper has already been published by ACS and you want to include the text or portions of the text in your thesis/dissertation in **print or microfilm formats**, please print the ACS copyright credit line on the first page of your article: "Reproduced (or 'Reproduced in part') with permission from [FULL REFERENCE CITATION.] Copyright [YEAR] American Chemical Society." Include appropriate information.

Submission to a Dissertation Distributor: If you plan to submit your thesis to UMI or to another dissertation distributor, you should not include the unpublished ACS paper in your thesis if the thesis will be disseminated electronically, until ACS has published your paper. After publication of the paper by ACS, you may release the entire thesis (**not the individual ACS article by itself**) for electronic dissemination through the distributor; ACS's copyright credit line should be printed on the first page of the ACS paper.

Use on an Intranet: The inclusion of your ACS unpublished or published manuscript is permitted in your thesis in print and microfilm formats. If ACS has published your paper you may include the manuscript in your thesis on an intranet that is not publicly available. Your ACS article cannot be posted electronically on a publicly available medium (i.e. one that is not password protected), such as but not limited to, electronic archives, Internet, library server, etc. The only material from your paper that can be posted on a public electronic medium is the article abstract, figures, and tables, and you may link to the article's DOI or post the article's author-directed URL link provided by ACS. This paragraph does not pertain to the dissertation distributor paragraph above.

Other conditions:

v1.1

Gratis licenses (referencing $0 in the Total field) are free. Please retain this printable license for your reference. No payment is required.

If you would like to pay for this license now, please remit this license along with your payment made payable to "COPYRIGHT CLEARANCE CENTER" otherwise you will be invoiced within 48 hours of the license date. Payment should be in the form of a check or money order referencing your account number and this invoice number RLNK10814542.
Once you receive your invoice for this order, you may pay your invoice by credit card. Please follow instructions provided at that time.

Make Payment To:
Copyright Clearance Center
Dept 001
P.O. Box 843006
Boston, MA 02284-3006

If you find copyrighted material related to this license will not be used and wish to cancel, please contact us referencing this license number 2467110797649 and noting the reason for cancellation.

Questions? customercare@copyright.com or +1-877-622-5543 (toll free in the US) or +1-978-646-2777.
